

Analysis and Design of a Conductively Cooled Superconducting Magnet System for a Rotary Active Magnetic Regenerative Liquefier

by

**Dale William Goudie
B.A.Sc., Queen's University, 1990**

A Thesis Submitted in Partial Fulfillment of the
Requirements for the Degree of

Master of Applied Science

in the Department of Mechanical Engineering

We accept this thesis as conforming to the required standard

[Redacted Signature]

Dr. John A. Barclay, Supervisor (Department of Mechanical Engineering)

[Redacted Signature]

Dr. David S. Scott, Departmental Member (Department of Mechanical Engineering)

[Redacted Signature]

Dr. Stanislaw S. Stuchly, Outside Member (Department of Electrical & Computer Engineering)

[Redacted Signature]

Mr. Paul Reeve, Additional Member

[Redacted Signature]

Dr. Sydney R. Kreitzman, External Examiner (TRIUMF)

© Dale W. Goudie, 1996
University of Victoria

All rights reserved. This thesis may not be reproduced in whole or in part, by photocopy or other means, without the permission of the author.

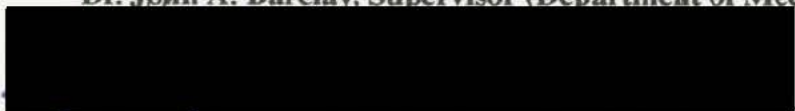
Supervisor: Dr. John A. Barclay

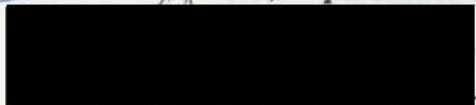
Abstract

Liquid natural gas (LNG) has been identified as having a strong growth potential in the alternative transportation fuels market. One of the barriers to the adoption of LNG, however, is a lack of economical refuelling stations. The Cryofuel Systems Group, at the University of Victoria, is developing cost effective and efficient liquefaction technologies for distributed fleet-sized LNG refuelling stations. One of the technologies under development is a rotary active magnetic regenerative liquefier (AMRL). A sub-system of the AMRL is a conductively cooled superconducting (SC) magnet system. This thesis presents a substantial part of the analysis and design of such a SC magnet system for an AMRL. Potential SC coil configurations for the magnet system of a rotary AMRL were examined and a partial tokamak and an elliptical split pair were selected as suitable configurations. The magnetostatic analysis and winding design of both configurations are presented along with a force analysis which was used for the structural design. An analysis of the thermal loads and design of the thermal pathways for the conduction cooling system are also presented.


Examiners:


 Dr. John A. Barclay, Supervisor (Department of Mechanical Engineering)


 Dr. David S. Scott, Departmental Member (Department of Mechanical Engineering)


 Dr. Stanislaw S. Stuchly, Outside Member (Department of Electrical & Computer Engineering)


 Mr. Paul Reeve, Additional Member


 Dr. Sydney R. Kretzman, External Examiner (TRIUMF)

2.2.1	Magnet Configurations for Rotary MR Devices	19
2.2.2	Summary of Rotary MR Devices	21
2.3	Superconducting (SC) Coil Design	23
2.4	Structural Design of SC Magnet Systems	27
2.5	Conductively Cooled SC Magnet Systems	30
2.6	Auxiliary Components of SC Magnet Systems	35
2.6.1	Power Supply	35
2.6.2	Current Leads	35
2.6.3	Persistent Current Switch	37
2.6.4	Quench Protection	39
3.0	AMRL Magnet Sub-System	42
3.1	Design Process	42
3.2	Specifications and Constraints	43
3.2.1	Large AMRL Geometric Specifications	44
3.2.2	Small AMRL Geometric Specifications	45
3.3	Evaluation of Coil Configurations	46
3.3.1	Racetrack Configuration	46
3.3.2	Split Pair Configuration	47
3.3.3	Solenoid Configuration	48
3.3.4	Partial Tokamak Configuration	50
3.4	First AMRL Coil Configuration	51
3.5	Second AMRL Coil Configuration	51
3.6	Design Methodology	52
4.0	Magnetic Field Modelling and Coil Design	53
4.1	Magnetic Field Modeler	53
4.2	Design Information	55
4.2.1	SC Wire Critical Current	55
4.2.2	Material Magnetization Properties	57
4.3	Partial Tokamak Configuration for Large AMRL	60
4.3.1	Early Designs	60

7.0	Conclusions	4.3.2 Compensating End Coils	63
7.1		4.3.3 Winding Optimization	66
7.2		4.3.4 Final Partial Tokamak Coil Design	69
4.4	Split Pair Configuration for Small AMRL		71
8.0	References	4.4.1 Design Variables	71
Appendix - A		4.4.2 Design Evolution of Split Pair Coils for the AMRL	74
A.1		4.4.3 Winding Optimization	77
		A.1.1 Coil Forces	120
		A.1.2 Magnetic Material Forces	121
		A.2 Elliptical Split Pair Configuration	124
		A.2.1 Coil Forces	125
		A.2.2 Forces on Magnetic Materials	127
Appendix - A		A.2.3 Gravitational Body Forces	129
B.1		A.2.4 Summary of Forces	129
5.0	Structural Force Analysis		85
5.1	Force Analysis		85
5.2	Partial Tokamak Configuration Forces		86
	5.2.1 Coil Forces		86
	5.2.2 Forces on Magnetic Materials		87
Appendix - A		5.2.3 Gravitational Body Forces	89
B.1		5.2.4 Summary of Forces	89
5.3	Elliptical Split Pair Configuration Forces		90
	5.3.1 Coil Forces		90
B.2		5.3.2 Forces on Magnetic Materials	91
	5.3.3 Gravitational Body Forces		91
	5.3.4 Summary of Forces		92
		B.2.3 Cooldown from 30 K to 4.2 K	128
6.0	Thermal Analysis of Magnet System		93
6.1	Thermal Analysis		93
Appendix - A		6.2 Steady State Operation	93
C.1		6.2.1 First Stage Heat Loads	94
		6.2.2 Second Stage Heat Loads	97
6.3	Charging		97
6.4	Cooldown		99
6.5	Quenching		100
6.6	Cryocooler and Conduction Pathways		101
6.7	Summary of Thermal Analysis		105

7.0	Conclusions and Future Work	106
7.1	Conclusions	106
7.2	Suggestions for Future Work	108
8.0	References	110
Appendix - A	Body Forces on Magnet Assembly	120
A.1	Large AMRL - Partial Tokamak Configuration	120
A.1.1	Coil Forces	120
A.1.2	Magnetic Material Forces	121
A.1.3	Gravitational Forces	122
A.2	Small AMRL - Elliptical Split Pair Configuration	123
A.2.1	Gravitational Forces	123
Appendix - A	Heat Loads on Magnet Assembly	124
B.1	Heat Loads During Steady State Operation	124
B.1.1	First Stage Loads	124
B.1.2	Second Stage Loads	126
B.2	Estimation of Cooldown Time	127
B.2.1	Cooldown from 300 K to 100 K	127
B.2.2	Cooldown from 100 K to 50 K	127
B.2.3	Cooldown from 50 K to 4.2 K	128
B.3	Thermal Conduction Pathway	128
Appendix - A	Cryocooler Evaluations	129
C.1	Description of Suitable Cryocoolers	129
	directions	130
	Magnetic forces on AMR bins of large AMRL in x-y directions.	131
	Estimates of weight of partial tokamak magnet assembly.	132
	Estimates of weight of elliptical split pair magnet assembly.	133
	Heat loads to first stage.	135

Table B.1.2a: Heat loads to second stage	126
Table B.3.0a: Temperatures within second stage conduction pathway during steady state operation	128
Table C.1.0a: Summary of cryocooler specifications.	129

List of Tables

Table 1.1.1a: Summary of estimated vehicle fuel consumption in the USA. [2]	2
Table 2.2.2a: Summary of literature regarding rotary MR devices.	21
Table 4.2.1a: Typical operating currents for NbTi filamentary wire.	56
Table 4.2.1b: Typical operating currents for Nb ₃ Sn filamentary wire.	57
Table 4.3.4a: Manufacturer's initial cost estimate and comments of partial tokamak coils.	70
Table 4.4.1a: Centerline magnetic field estimations of circular split pair coils with varying w:h ratios as described in Figure 4.4.1b.	73
Table 6.7.0.a: Summary of estimated heat loads and temperatures of the elliptical split pair magnet assembly for the AMRL.	105
Table A.1.1a: Lorentz forces on partial tokamak coils of large AMRL in x-y directions.	120
Table A.1.2a: Magnetic forces on AMR bins of large AMRL in x-y directions.	121
Table A.1.3a: Estimates of weight of partial tokamak magnet assembly.	122
Table A.2.1a: Estimates of weight of elliptical split pair magnet assembly.	123
Table B.1.1a: Heat loads to first stage.	125

Table B.1.2a: Heat loads to second stage.	126
Table B.3.0a: Temperatures within second stage conduction pathway during steady state operation.	128
Table C.1.0a: Summary of cryocooler specifications.	129

List of Figures

Figure 1.1.1a	Total energy supply and consumption for North America in 1993 [1].	4
Figure 1.1.1b	Volumetric energy density of vehicular fuels [11].	5
Figure 1.1.2a	Supply price of LNG delivered at 100 psig (670 kPa) as a function of refuelling station capital cost and liquefier efficiency for a heavy duty vehicle fleet.	6
Figure 1.1.3a	Adiabatic temperature change of gadolinium as a function of temperature and applied magnetic field [15].	8
Figure 1.1.3b	Schematic diagram of rotary AMRL for natural gas liquefaction.	10
Figure 1.1.3c	Magnetization of gadolinium as a function of applied magnetic field and temperature.	11
Figure 1.2.0a	An example of the critical surface for a superconducting alloy of NbTi [17].	13
Figure 1.2.0b	Schematic diagram of a conduction cooled superconducting magnet system.	14
Figure 2.2.0a	Temperature entropy diagrams of the magnetic refrigerant material during different magnetic refrigeration cycles.	17
Figure 2.2.0b	Temperature entropy diagrams of the magnetic refrigerant material during different magnetic refrigeration cycles.	17
Figure 2.2.0c	Temperature entropy diagrams of the magnetic refrigerant material during different magnetic refrigeration cycles.	17

Figure 2.2.1a	Basic coil configurations for rotary magnetic refrigeration devices.....	20
Figure 2.3.0a	Schematic profile of magnetic field through a solenoid at section a-a.....	25
Figure 2.4.0a	Schematic of the Lorentz forces and radial and hoop stresses on a solenoid.....	28
List of Figures		
Figure 2.6.3a	Persistent current switch circuit diagram.....	38
Figure 1.1.1.a	Total energy supply and consumption for North America in 1993 [1].	4
Figure 2.6.4b	Passive quench protection circuit using a coupled secondary coil.....	40
Figure 1.1.1b	Volumetric energy density of vehicular fuels [11].	5
Figure 2.6.4c	Passive quench protection circuit using high power diodes.....	41
Figure 1.1.2a	Supply price of LNG delivered at 100 psig (670 kPa) as a function of refuelling station capital cost and liquefier efficiency for a heavy duty vehicle fleet.	6
Figure 3.2.2a	6
Figure 1.1.3a	Adiabatic temperature change of gadolinium as a function of temperature and applied magnetic field [15].	8
Figure 3.3.2a	8
Figure 1.1.3b	Schematic diagram of rotary AMRL for natural gas liquefaction.	10
Figure 3.3.3a	10
Figure 1.1.3c	Magnetization of gadolinium as a function of applied magnetic field and temperature.	11
Figure 3.3.3b	11
Figure 1.2.0a	An example of the critical surface for a superconducting alloy of NbTi [17].	13
Figure 3.3.4a	13
Figure 1.2.0b	Schematic diagram of a conduction cooled superconducting magnet system.	14
Figure 3.3.4b	14
Figure 2.2.0a	Temperature entropy diagrams of the magnetic refrigerant material during different magnetic refrigeration cycles.	17
Figure 4.2.2a	Graph of B vs. $\mu_0 H$ for Gadolinium near its Curie temperature.....	58
Figure 4.2.2b	Graph of B vs. $\mu_0 H$ for Dysprosium near its Curie temperature.....	58
Figure 4.2.2c	Graph of B vs. $\mu_0 H$ for C1010 low carbon steel.....	59
Figure 4.3.1a	Early partial tokamak designs with six coils.....	60

Figure 2.2.1a	Basic coil configurations for rotary magnetic refrigeration devices.	20
Figure 2.3.0a	Schematic profile of magnetic field through a solenoid at section a-a.	25
Figure 2.4.0a	Schematic of the Lorentz forces and radial and hoop stresses on a solenoid.	28
Figure 2.6.2a	Thermal anchoring techniques for HTSC current leads.	37
Figure 2.6.3a	Persistent current switch circuit diagram.	38
Figure 2.6.4a	The basic detect-and-dump active quench protection circuit.	39
Figure 2.6.4b	Passive quench protection circuit using a coupled secondary coil.	40
Figure 2.6.4c	Passive quench protection circuit using high power diodes.	41
Figure 3.2.1a	Schematic of the large AMRL geometry.	45
Figure 3.2.2a	Schematic of small AMRL geometry.	46
Figure 3.3.1a	Schematic of stacked racetrack coil configuration.	47
Figure 3.3.2a	Schematic of split pair coil configuration.	48
Figure 3.3.3a	Comparison of magnetization zones for solenoid coil configuration.	49
Figure 3.3.3b	Schematic of "chainsaw" AMR and solenoid coil configuration.	49
Figure 3.3.4a	Coil spacing of partial tokamak configuration.	50
Figure 4.2.2a	Graph of B vs. $\mu_0 H$ for Gadolinium near its Curie temperature of 293 K.	58
Figure 4.2.2b	Graph of B vs. $\mu_0 H$ for Dysprosium near its Curie temperature of 179 K.	58
Figure 4.2.2c	Graph of B vs. $\mu_0 H$ for C1010 low carbon steel.	59
Figure 4.3.1a	Early partial tokamak designs with six coils.	60

Figure 4.3.1b	Sketch of the x-y plane applied field profile on the AMR ring of the six coil partial tokamak model.	61
Figure 4.3.1c	Schematic of end coil placement and dewar wall construction space.	62
Figure 4.3.1d	Applied magnetic field profile of basic ten coil partial tokamak.	63
Figure 4.3.1e	Graph of applied field along radial segments at various angular positions for basic ten coil partial tokamak.	64
Figure 4.3.2a	Diagram of single current density, ten coil partial tokamak with compensating end coils.	65
Figure 4.3.2b	Applied magnetic field profile of single current density, ten coil partial tokamak with compensating end coils.	66
Figure 4.3.3a	Applied field profiles along centerline of single current density, main and compensating coils from partial tokamak shown in Figure 4.3.2a.	67
Figure 4.3.3b	Calculation of centerline field profile by dividing a solenoid into two unequal sections [17].	68
Figure 4.3.4a	Schematic of final partial tokamak coil design.	70
Figure 4.4.1a	Variable dimensions of elliptical, split pair coils.	71
Figure 4.4.1b	Sketch of circular split pair coils with varying w:h ratios.	72
Figure 4.4.1c	Sketch of varying AMR placement with respect to the coils.	74
Figure 4.4.2a	Sketch of NbTi split pair coil design for large AMR ring.	75
Figure 4.4.2b	Sketch of Nb ₃ Sn split pair coil model with 5 cm wide yoke.	76
Figure 4.4.2c	Plots of applied field magnitude along lines described in Figure 4.4.2b in midplane of Nb ₃ Sn split pair coil.	77
Figure 4.4.3a	Spreadsheet results of winding area minimization for three-winding Nb ₃ Sn elliptical coils.	79

Figure 4.4.3b	Applied magnetic field profile of three-winding, elliptical, Nb ₃ Sn, split pair coils around an AMR ring with a placement distance of 15 cm.	80
Figure 4.4.3c	Applied magnetic field profile of three-winding, elliptical, Nb ₃ Sn, split pair coils around an AMR ring with a placement distance of 13 cm.	81
Figure 4.4.3d	Applied magnetic field profile of three-winding, elliptical, Nb ₃ Sn, split pair coils around an AMR ring with a placement distance of 11 cm.	81
Figure 4.4.3e	Sketch of final Nb ₃ Sn, elliptical, split pair coil design.	84
Figure 4.4.3f	Applied magnetic field profile of final split pair coil design around AMR ring with a placement distance of 15 cm.	84
Figure 5.2.1a	Lorentz forces in the x-y plane on individual coils of the partial tokamak assembly.	87
Figure 5.2.2a	Magnetic forces on AMR bins in x-y plane.	88
Figure 5.2.4a	Schematic summary of forces on partial tokamak magnet assembly.	90
Figure 5.3.4a	Schematic summary of forces on elliptical split magnet assembly.	92
Figure 6.2.1a	Schematic diagram of the heat loads to the first stage of the cryocooler.	94
Figure 6.6.0a	Sketch of thermal conduction path between superconducting windings and second stage of cryocooler.	102

Nomenclature

- k thermal conductivity (W/m·K)
 k_a apparent thermal conductivity (W/m·K)
 k_c thermal conductance (W/m²·K)
 L inductance (H)
 a inner minor diameter of ellipse (m)
 a_s inner radius of solenoid (m)
 A surface area of radiating body (m²)
 A_x cross sectional area (m²)
 AT_{total} total number of ampere turns (A)
 b inner major diameter of ellipse (m)
 b_s outer radius of solenoid (m)
 B magnetic flux density (T)
 \vec{B} magnetic flux density vector (T)
 c body displacement for force calculation using virtual work method (m)
 C heat capacity (kJ/kg·K)
 d_w wire diameter (mm)
 E energy (J)
 \vec{F} force vector (N)
 F_c force in direction of displacement, c (N)
 F_e emissivity factor
 h elliptical coil winding height (m)
 H applied magnetic field (A/m)
 \vec{H} applied magnetic field vector (A/m)
 H_c critical applied magnetic field at T_c and J_c (A/m)
 H_{c0} critical applied magnetic field at $T = 0$ and $J = 0$ (A/m)
 H_z applied magnetic field along solenoid centerline (A/m)
 I_{op} operating current (A)
 I_p primary circuit operating current (A)
 I_s secondary circuit operating current (A)
 J current density (A/m²)
 J_c critical current density at T_c and H_c (A/m²)
 J_{test} tested critical current density at T_{test} (A/m²)

k	thermal conductivity (W/m·K)
k_a	apparent thermal conductivity (W/m·K)
k_c	thermal contact resistance (W/m ² ·K)
l	1/2 length of solenoid
L	inductance (H)
m	mass (kg)
M	magnetization (A/m)
\vec{M}	magnetization vector (A/m)
M_{ind}	mutual inductance (H)
p	placement distance between center of AMR ring and major axis of elliptical winding (m)
P.F.	wire packing factor (%)
Q	heat energy (J)
\dot{Q}	heat transfer rate (W)
\dot{Q}_{Ω}	joule heating rate (W)
\dot{Q}_{cond}	conductive heat transfer rate (W)
\dot{Q}_{rad}	radiative heat transfer rate (W)
r	radius (m)
R	mean radius of AMR ring (m)
R_D	resistance of dump resistor (Ω)
R_Q	quench resistance (Ω)
s	separation distance
S	entropy (J/K)
t	time (s)
T	temperature (K)
T_c	critical temperature at H_c and J_c (K)
T_{co}	critical temperature at $H = 0$ and $J = 0$ (T)
T_{test}	tested critical temperature at J_{test} (K)
T_q	equilibrium temperature after quenching (K)
Vol	Volume (m ³)
w	elliptical coil winding width (m)
W_n	elliptical coil winding width of section n (m)

Greek

α	solenoid shape factor
β	solenoid shape factor
μ_0	permeability of free space ($4\pi \times 10^{-7} \text{ N/A}^2$)
σ	Stefan-Boltzmann constant ($5.671 \times 10^{-8} \text{ W/m}^2 \cdot \text{K}^4$)
σ_r	radial stress (Pa)
σ_θ	hoop stress (Pa)
θ	integral of thermal conductivity (W/m)
$\bar{\rho}_e$	average electrical resistivity ($\Omega \cdot \text{m}$)

- Dr. John Barclay, my supervisor, for his infectious enthusiasm, strong words of encouragement, and high expectations;
- Dr. Jeff Hall, for his technical advice and engineering philosophy of getting a working solution rather than solving all the work;
- Sue Walker and Dolores Bogatz, for their knowledge of the university bureaucracy and ability to fix a jammed photocopier faster than a speeding bullet;
- my fellow graduate students for their practical advice and practical jokes; and
- all of the other members of IESVic who have helped me along the way.

I would also like to acknowledge the Natural Sciences and Engineering Research Council of Canada (NSERC) and Contra Gas for their funding of this work and the projects associated with it.

I also wish to thank my family and friends for their support and encouragement even though many of them stared blankly when I tried to explain my work. Finally, I would especially like to thank Dr. Patrick Goetlaizen who gave me my first "kick at the can" and whose support I shall always be grateful for.

Acknowledgments

The time I have spent at IESVic and Cryofuel Systems has been both intellectually challenging and rewarding. I feel very privileged to have been involved with such an exceptional group of people and I regard them as my colleagues and my friends. This work could not have been completed without their help. In particular I would like to thank:

- Dr. John Barclay, my supervisor, for his infectious enthusiasm, strong words of encouragement, and high expectations;
- Dr. Jeff Hall, for his technical advice and engineering philosophy of getting a working solution rather than solving all the work;
- Sue Walton and Dolores Bogusz, for their knowledge of the university bureaucracy and ability to fix a jammed photocopier faster than a speeding bullet;
- my fellow graduate students for their practical advice and practical jokes; and
- all of the other members of IESVic who have helped me along the way.

I would also like to acknowledge the Natural Sciences and Engineering Research Council of Canada (NSERC) and Centra Gas for their funding of this work and the projects associated with it.

I also wish to thank my family and friends for their support and encouragement even though many of them stared blankly when I tried to explain my work. Finally, I would especially like to thank Dr. Patrick Oosthuizen who gave me my first “kick at the can” and whose support I shall always be grateful for.

Chapter 1

Introduction

1.1 Introduction

The energy supplied to the global transportation sector is presently dominated by petroleum based fuels such as gasoline, diesel, and jet-A. In 1993, these petroleum products accounted for 99.8% of the energy consumed within the transport sector in North America [1]. Although oil-based fuels overwhelm the market, there is growing motivation for the adoption of alternative fuels. Public awareness of the real and perceived environmental damage is encouraging a shift away from traditional fuels. There is also the added political concern of the growing dependence upon foreign oil supplies. International conflicts and embargoes can cause fluctuations in oil supply and price which can directly affect the economies of consumer nations. Together, these environmental, economic, and political forces are providing an opportunity for growth in the market share of alternative fuels within the transportation sector.

The Institute for Integrated Energy Systems (IESVic) at the University of Victoria is committed to the development of flexible energy systems that provide economic opportunities and minimize environmental intrusion. The Cryofuel Systems Group (CFS), a research group within IESVic, has recognized the growth potential of alternative fuels within the transportation sector and is pursuing the development of technologies that target this opportunity. In particular, CFS has identified a lack of economical natural gas refuelling stations as a barrier to the widespread adoption of natural gas as a transportation fuel. The work in this thesis is part of the research carried out by CFS towards the development of a natural gas refuelling station.

1.1.1 Alternative Fuels

Alternative fuels includes methanol (M-100 and M-85), ethanol (E-95 and E-85), liquefied petroleum gas (LPG), natural gas (NG) in a compressed (CNG) and liquefied (LNG) form, hydrogen, and electricity. In the United States, alternative fuels account for about 0.2% of the transportation fuels market [2] and this value is slowly growing due to government legislation [3], advances in technology, and increasingly favorable economics. Because this growing market is in its infancy, the market share of each fuel is changing considerably. LPG presently holds the largest share of the alternative fuels market but at current growth rates, natural gas will eventually dominate the market. Table 1.1.1a shows the breakdown and growth of the alternative fuels market in the United States with estimates of vehicle fuel consumption.

Table 1.1.1a: Summary of estimated vehicle fuel consumption in the USA. [2]

Fuel ¹	Estimated Consumption (Thousand gasoline-equivalent gallons)		
	1992	1993	1995
M-100	2,547	3,166	3,160
M-85	1,069	1,593	3,411
E-95	85	80	104
E-85	21	48	89
LPG	208,142	264,655	293,773
CNG	16,823	21,603	66,783
LNG	585	1,900	2,734
Electricity	374	309	525
Ethanol in Gasohol (E-10)	701,000	760,000	871,030
Gasoline	110,135,000	111,323,000	113,914,000
Diesel	23,866,000	24,296,630	25,965,830

¹ Fuel terms are defined in nomenclature. **M-100** = neat methanol; **M-85** = mixture of 85% methanol, 15% gasoline; **E-95** = mixture of 95% ethanol, 5% gasoline; **E-85** = mixture of 85% ethanol, 15% gasoline; **LPG** = liquefied petroleum gas; **CNG** = compressed natural gas; **LNG** = liquefied natural gas.

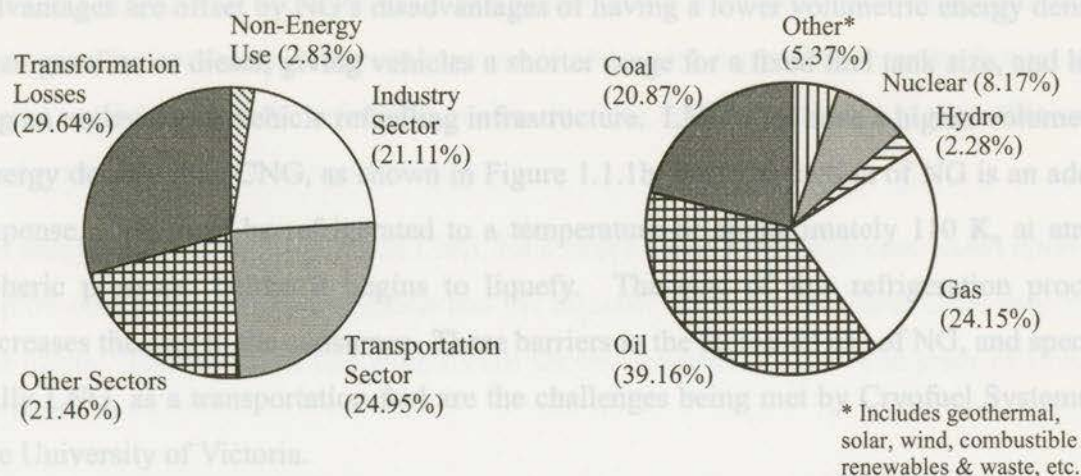
Methanol and ethanol based fuels are presently in limited use as transportation fuels. They will probably not be used significantly in the future because of problems involving their toxicity, dangerous emissions of organic compounds, corrosivity, and water solubility. Low cost production of methanol from natural gas is possible but the largest barrier to its adoption is the lack of an economical distribution infrastructure [4][5]. Ethanol production is limited by the availability of grain crops, corn in particular, as a feedstock and it also lacks a distribution infrastructure. The largest demand for ethanol is as an additive to gasoline, making gasohol or E-10 (10% ethanol and 90% gasoline), to meet oxygenated gasoline requirements.

As the alternative fuels market has emerged over the last decade or more, LPG has been widely adopted due to its competitive pricing, ease of engine conversion, and ability to be stored easily in low pressure (2 MPa) tanks. It is a by-product of natural gas processing and petroleum refining consisting mainly of propane plus some propylene, butane, and butylene. LPG currently dominates the alternative fuels but its market share is declining. It will, however, always hold some share of this market because of competitive pricing, government incentives, environmental benefits, support from the petroleum industry, and availability [2][6].

As the alternative fuels market grows, the market share of LPG will decline for two reasons. First, the total supply of LPG is limited and not significant enough to justify a large share of the transportation fuels market. Figure 1.1.1.a shows that the transportation sector annually consumes 25% of North America's energy supply yet LPG accounts for only 3.5% of the total annual supply [7]. The overall supply of oil and natural gas is much higher than LPG so it would seem logical that these fuels should account for a more significant share of each consumption sector. Second, much of the LPG consumed is dedicated as feedstock for many industrial chemical processes. This can sometimes make LPG more valuable as a feedstock than as a fuel.

Although both hydrogen and electricity are classified as alternative fuels, their current use in the transportation sector is negligible. Globally, there are only a few demonstration vehicles operating on hydrogen and the majority of electric vehicles are owned and operated by hobbyists [6]. Hydrogen vehicle technologies, such as fuel cells and high volumet-

Total Primary Energy Supply (TPES) = 99.8 EJ



Energy Consumption by Sector

Primary Energy Supply by Source

Figure 1.1.1.a Total energy supply and consumption for North America in 1993 [1].

ric energy density H_2 storage vessels, require much more research and development before they become competitive with conventional technologies. Additionally, most hydrogen today is derived from natural gas by steam methane reforming. One of the by-products during the reformation process is CO_2 so it is not a perfectly "clean" fuel as thought by many enthusiasts. Electric vehicles are also subject to this same misunderstanding of being environmentally benign. The source of the electricity is typically a coal-fired, nuclear, or hydro-electric power plant which does make an environmental impact. The technology of today's electric vehicles also limits their market acceptance. Battery systems require charging times of 6 to 10 hours and are heavy and bulky with low energy densities [6]. This results in vehicles that are often underpowered with a limited range. Despite their disadvantages, electric vehicles still cater to a small niche of electric vehicle enthusiasts. It is unlikely, however, that they will see widespread use anytime soon. Natural gas usage in the transportation sector is growing faster than all other alternative fuels and has been identified as the most promising substitute to diesel and gasoline [8][9][10]. NG is a low carbon fuel, consisting primarily of methane (CH_4), making it relatively clean burning with low CO , NO_x , and particulate emissions. It also has the

added benefits of having a somewhat uniform global distribution and being economically competitive with conventional fuels. These environmental, political, and economic advantages are offset by NG's disadvantages of having a lower volumetric energy density than gasoline or diesel, giving vehicles a shorter range for a fixed fuel tank size, and having an undeveloped vehicle refuelling infrastructure. LNG does have a higher volumetric energy density than CNG, as shown in Figure 1.1.1b, but liquefaction of NG is an added expense. NG must be refrigerated to a temperature of approximately 110 K, at atmospheric pressure, before it begins to liquefy. The cost of this refrigeration process increases the cost to the consumer. These barriers to the increased use of NG, and specifically LNG, as a transportation fuel are the challenges being met by Cryofuel Systems at the University of Victoria.

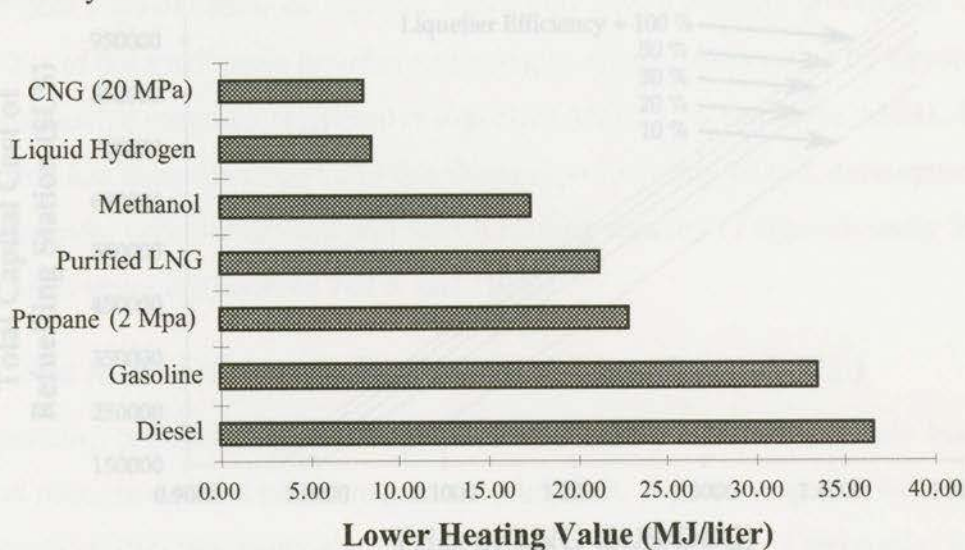


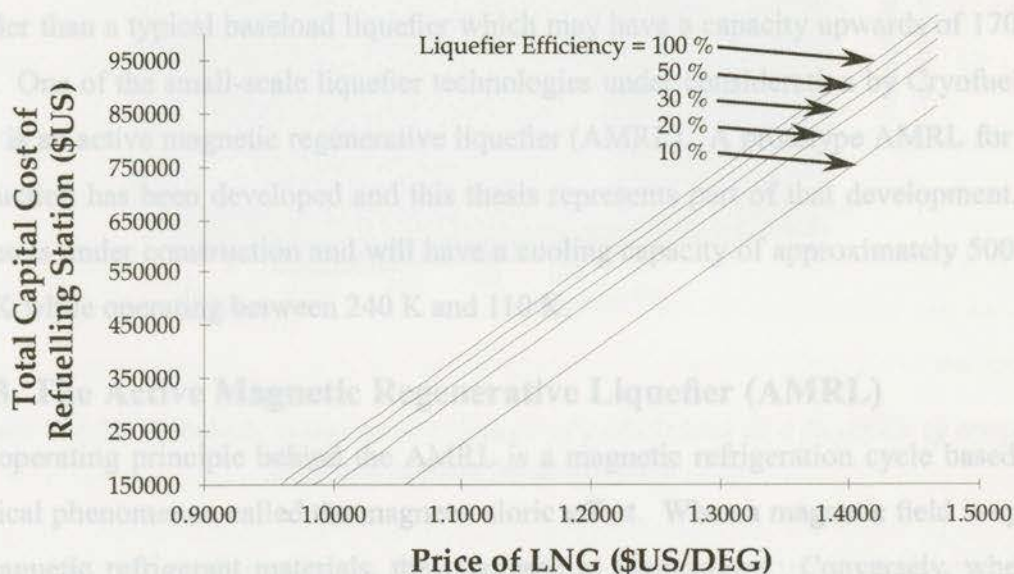
Figure 1.1.1b Volumetric energy density of vehicular fuels [11].

1.1.2 Cryofuel Systems' Natural Gas Liquefier Project

The greatest barrier to the widespread adoption of LNG is a lack of economical refuelling stations [10]. North America has an extensive gas pipeline infrastructure and large centralized liquefaction plants but no localized, small-scale liquefiers for refuelling stations. The development of economical, small-scale refuelling stations, integrated with an NG liquefier, will increase the incentive for the conversion to LNG as a transport fuel.

A better definition of this barrier, as identified by Cryofuel Systems [12], is a need to supply LNG for a lower price, as delivered to the consumer, than conventional fuels. LNG becomes the obvious choice when it can be purchased at a lower price than diesel, on an energy equivalent basis. The supply price of LNG varies depending on many factors such as the capital cost of the refuelling station, the NG feedstock price, liquefier efficiency, road taxes, and vehicle conversion costs.

An analysis of the supply price of LNG, for a fleet of heavy duty vehicles, based upon the capital cost of the refuelling station and the liquefier efficiency has been done as part of the thesis. The results of this analysis are shown in Figure 1.1.2a. The price of LNG is



Notes: (1) Liquefier capacity is 1000 diesel equivalent gallons (DEG) per day; (2) Feedstock price is \$2.50 (US) per Mcf; (3) Fleet is 10 heavy duty vehicles converted to LNG at a cost of \$18,000 (US) per vehicle; (4) Vehicle operation of 500 miles per day at 5 m.p.g.; (5) Annual operation of 260 days; (6) Annual operating expense of \$15,000 (US); (7) Interest rate is 8%; (8) Refuelling station capital cost amortized over 10 years; (9) Vehicle conversion cost amortized over 5 years; (10) Road taxes of \$0.27 (US) per DEG.

Figure 1.1.2a Supply price of LNG delivered at 100 psig (670 kPa) as a function of refuelling station capital cost and liquefier efficiency for a heavy duty vehicle fleet.

shown per diesel equivalent gallon (DEG), which is an amount of LNG with the equivalent energy content of one gallon of diesel fuel. This graph shows that increasing the efficiency of the liquefier provides a significant reduction in the price of the LNG up to a liquefaction efficiency of about 20%. Beyond 20% there is only a marginal reduction in

the price of LNG. Reducing the capital cost of the refuelling system also reduces the price of the LNG, which is to be expected. Reducing the liquefier cost is the a good way to reduce the total refuelling system capital cost because the liquefaction unit, of conventional integrated liquefier/refuelling stations, can account for as much as 50% of the total refuelling station cost [13].

The focus of Cryofuel Systems' research is the development of high efficiency and low cost NG liquefaction technologies. Cryofuel Systems has identified a market for a distributed, fleet-sized LNG refuelling station. This type of station would require a liquefier capable of producing about 1000 diesel equivalent gallons (DEG) of LNG per day which is equivalent to a refrigeration capacity of approximately 30 kW at 110 K. This is much smaller than a typical baseload liquefier which may have a capacity upwards of 170 MW [14]. One of the small-scale liquefier technologies under consideration by Cryofuel Systems is an active magnetic regenerative liquefier (AMRL). A prototype AMRL for LNG production has been developed and this thesis represents part of that development. This device is under construction and will have a cooling capacity of approximately 500 W at 110 K while operating between 240 K and 110 K.

1.1.3 The Active Magnetic Regenerative Liquefier (AMRL)

The operating principle behind the AMRL is a magnetic refrigeration cycle based on a physical phenomenon called the magnetocaloric effect. When a magnetic field is applied to magnetic refrigerant materials, they increase in temperature. Conversely, when the magnetic field is removed they decrease in temperature. It is analogous to the temperature change experienced by a gas during compression and expansion. Magnetic refrigeration is the application of the magnetocaloric effect in a thermodynamic cycle.

During a simple recuperative cycle, the magnetic refrigerant is adiabatically magnetized, causing an increase in temperature, and then the refrigerant is cooled by an external source. After this, the refrigerant is adiabatically demagnetized causing a reduction in temperature below the initial value so the refrigerant can absorb a cooling load. The difficulty with this basic cycle is that the adiabatic temperature change experienced by most magnetic refrigerants is on the order of a few degrees Kelvin depending on the absolute

temperature of the material and the magnitude of the applied magnetic field. An example of the adiabatic temperature change experienced by a common magnetic refrigerant, gadolinium, is shown in Figure 1.1.3a.

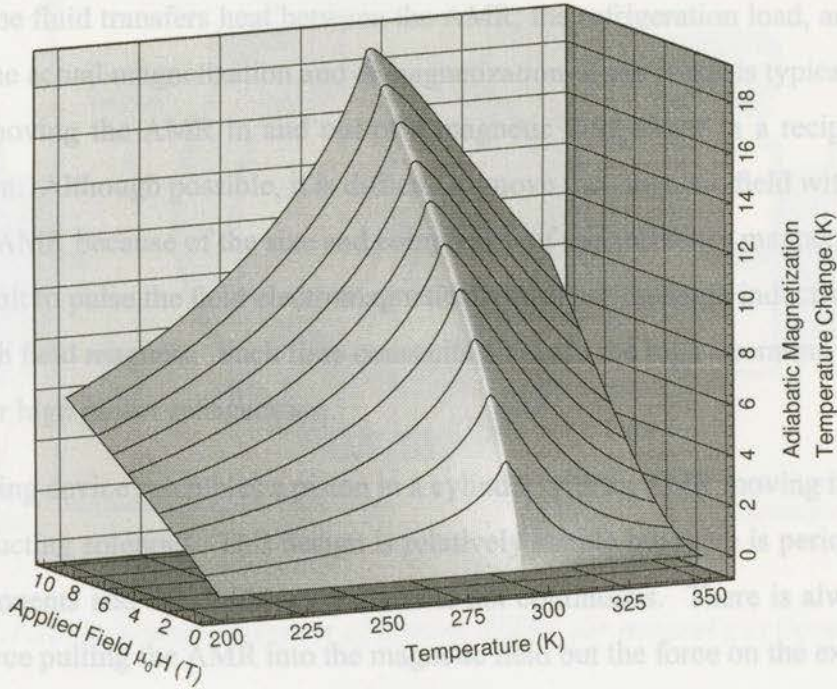


Figure 1.1.3a Adiabatic temperature change of gadolinium as a function of temperature and applied magnetic field [15].

This modest refrigeration effect is not enough for a practical refrigeration device. However, by using a regenerative heat exchanger, it is possible to achieve refrigeration over large temperature spans. One type of regenerative heat exchanger, which uses the magnetic refrigerant material as the regenerator matrix is called an active magnetic regenerator (AMR).

A regenerator is simply a porous solid bed through which a heat transport fluid passes and receives or rejects heat from the solid material. The regenerator also has a temperature gradient between the ends of the bed so the fluid experiences a large temperature change. In a conventional regenerative refrigeration cycle, such as the Stirling cycle or the Gifford-McMahon cycle, the regenerator is a passive device and the thermodynamic work of

the cycle is accomplished by compressing and expanding the working fluid. The thermodynamic work of an active magnetic regenerative refrigeration cycle is accomplished by magnetizing and demagnetizing the AMR. The working fluid acts as the connecting medium between elements of magnetic refrigerant within the regenerator [16]. This means that the fluid transfers heat between the AMR, the refrigeration load, and the environment. The actual magnetization and demagnetization of the AMR is typically done by physically moving the AMR in and out of a magnetic field either in a reciprocating or rotary fashion. Although possible, it is difficult to move the magnetic field with respect to a stationary AMR because of the size and complexity of the necessary magnet systems. It is also difficult to pulse the field electromagnetically because the large inductive time constants of high field magnets. Such time constants preclude the high operating frequencies necessary for high power refrigeration.

A reciprocating device resembles a piston in a cylinder with an AMR moving in and out of a superconducting solenoid. This design is relatively simple but there is periodic loading of the components and the fluid heat transfer is not continuous. There is always a large attractive force pulling the AMR into the magnetic field but the force on the exiting stroke is slightly larger than the force in the entering stroke. The greatest concern of the reciprocating devices is the recovery of the energy as the AMR enters and exits the magnetic field. A rotary AMR is a ring shaped wheel with the magnetic field applied on a section of the wheel. As the wheel rotates the magnetic material continuously enters and exits the magnetic field region. The rotary design is complex but it offers continuous heat transfer and energy recovery is not a concern because the large forces on the entering and exiting sections of the wheel are naturally reacted by the wheel geometry. The difference between the forces primarily represents the net force required for the cycle work input.

The prototype AMRL being developed by Cryofuel Systems is a rotary design. A schematic diagram of this design is given in Figure 1.1.3b. During operation a radial segment of the AMR enters the magnetic field region and increases in temperature due to the magnetocaloric effect. As the segment rotates through the magnetic field the heat transport fluid flows radially through the wheel and absorbs heat convectively from the AMR. The fluid then rejects this heat to the environment through a heat exchanger and the cooled

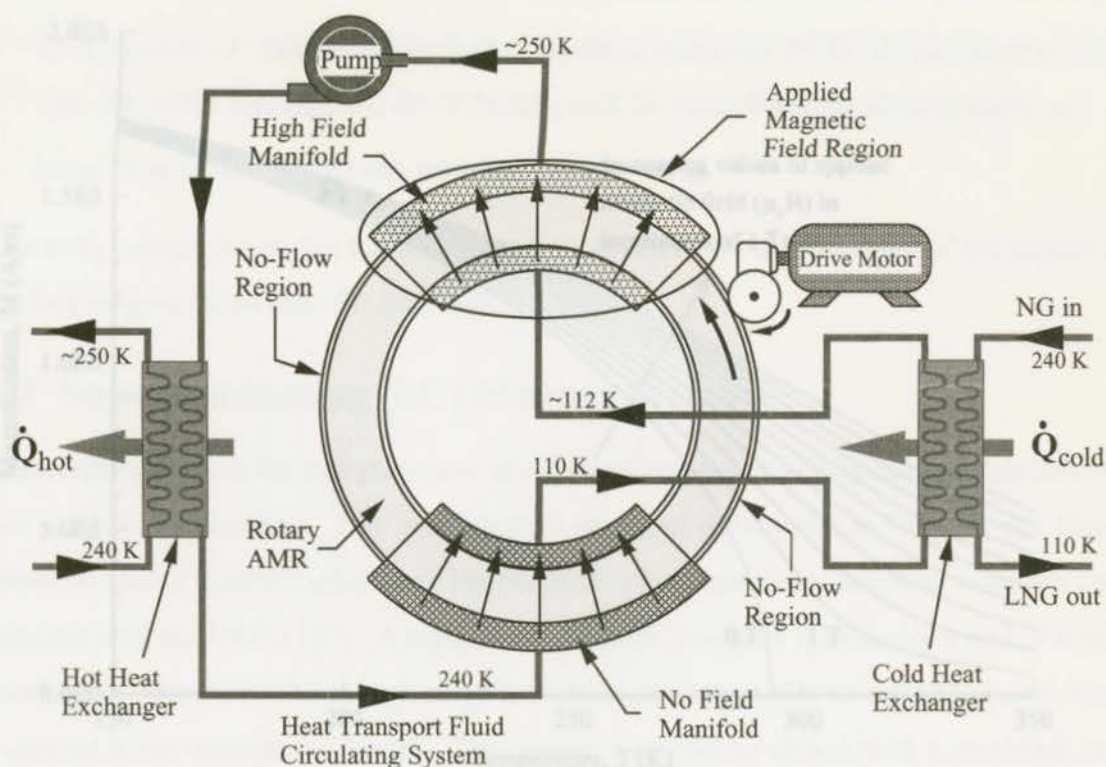


Figure 1.1.3b Schematic diagram of Rotary AMRL for natural gas liquefaction.

AMR segment rotates out of the field experiencing a further decrease in temperature. Following this, the segment enters the region of the no-field manifold and cools the heat transport fluid flowing through the ring. The cooled fluid can now absorb heat from the natural gas within the cold heat exchanger resulting in production of LNG. Finally, the AMR segment exits the no-field manifold region and begins the cycle again.

The portion of the AMR that exits the applied magnetic field has a lower average temperature profile than the portion that enters this region so the exiting portion is more magnetized than the entering portion. This occurs because the magnetization of the refrigerant material is a function of temperature as well as applied field, as shown in Figure 1.1.3c for gadolinium. Additionally, the force on any magnetic material is function of the gradient of the applied field and the magnetization of the material as given by Equation (1.1.3.a):

$$\vec{F} = (\vec{M} \cdot \nabla) \vec{B} \quad (1.1.3.a)$$

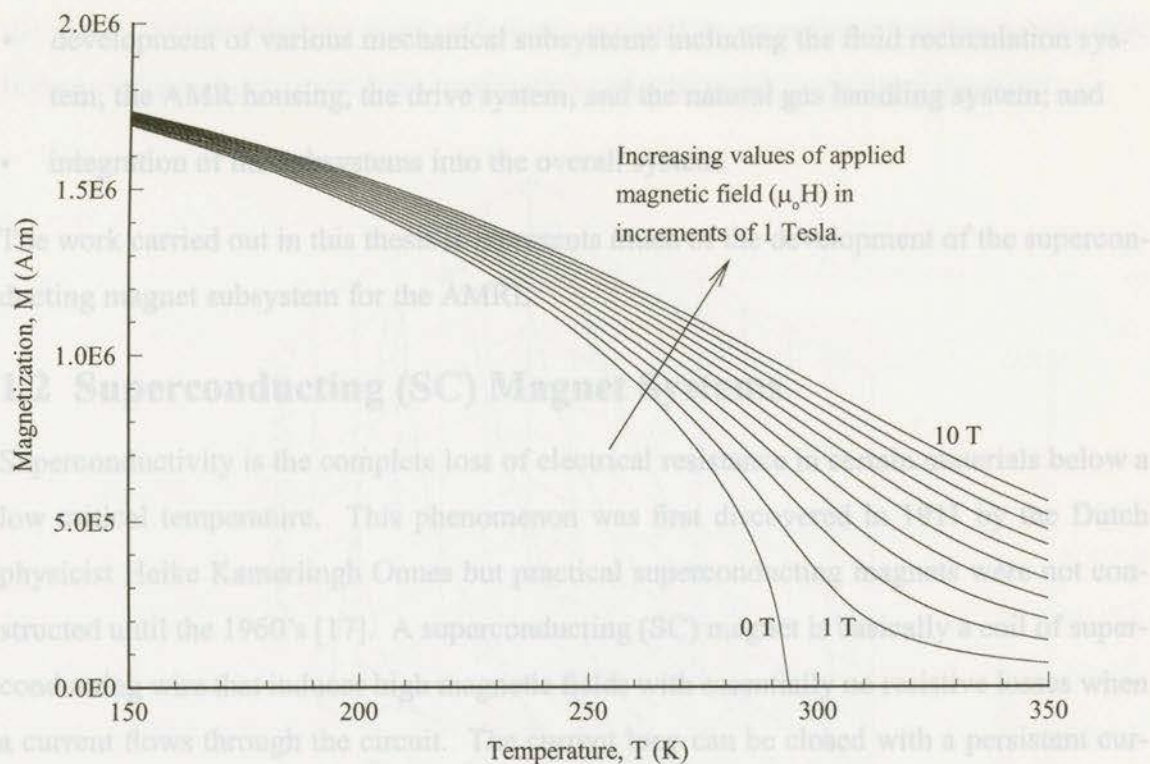


Figure 1.1.3c Magnetization of gadolinium as a function of applied magnetic field and temperature.

The applied field gradient on the entering and exiting sections is essentially the same, neglecting any field redistribution due to the difference in magnetization. Therefore, the imbalance in the magnetization of the entering and exiting sections of the AMR wheel results in an imbalance between the forces on these sections. The force imbalance manifests itself as a torque on the rotating AMR which represents the input work necessary to achieve refrigeration.

The development of the entire AMRL system is an ambitious task due to its complexity. To simplify the project, the AMRL research and development has been subdivided into several sections. These sections include:

- selection of suitable magnetic refrigerant materials and regenerator fabrication;
- development of a regenerator test apparatus and subsequent regenerator testing;
- numerical modelling and computer simulation of the AMRL;

- development of the superconducting magnet subsystem;
- development of various mechanical subsystems including the fluid recirculation system, the AMR housing, the drive system, and the natural gas handling system; and
- integration of the subsystems into the overall system.

The work carried out in this thesis represents much of the development of the superconducting magnet subsystem for the AMRL.

1.2 Superconducting (SC) Magnet Systems

Superconductivity is the complete loss of electrical resistance in certain materials below a low critical temperature. This phenomenon was first discovered in 1911 by the Dutch physicist Heike Kamerlingh Onnes but practical superconducting magnets were not constructed until the 1960's [17]. A superconducting (SC) magnet is basically a coil of superconducting wire that induces high magnetic fields with essentially no resistive losses when a current flows through the circuit. The current loop can be closed with a persistent current switch allowing the power supply to be disconnected without affecting the operation of the magnet. At present, most conventional SC magnets are made with wires of niobium tin (Nb_3Sn) or niobium titanium (NbTi) filaments in a copper stabilizer operating in a bath of liquid helium at temperatures of 4.2 K or lower. They can produce applied fields ($\mu_0 H$) of up to 10 T or more and are used in wide variety of applications such as particle accelerators, low purity ore separators, and magnetic resonance imaging (MRI) scanners for hospitals.

The phenomenon of superconductivity is not just limited by a critical temperature (T_c). Superconducting materials are also limited by a critical current density (J_c) and a critical applied magnetic field (H_c). These three properties are related to each other in T-J-H space by a critical surface that is material dependent. At any operating point above this surface the material will be in a non-superconducting, or normal, state. An example of the critical surface for an alloy of NbTi is given in Figure 1.2.0a. The transition from the superconducting to normal state of an operating magnet is called a quench. During a

quench the stored magnetic energy is resistively dissipated resulting in ohmic heating of the wires. Magnet designs must sufficiently account for quenching because catastrophic failure of the coil can occur from overheating and, ultimately, melting of the wires.

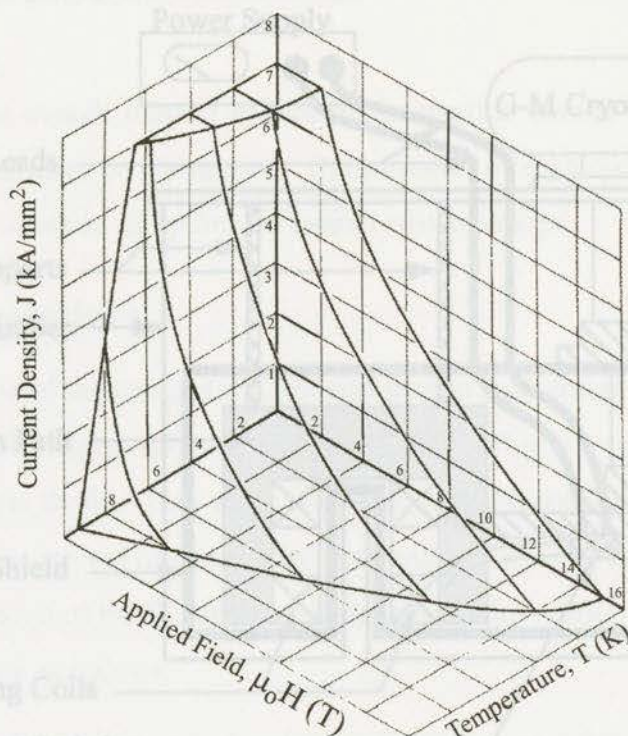


Figure 1.2.0a An example of the critical surface for a superconducting alloy of NbTi [17].

To maintain SC magnets in a liquid helium environment, highly effective dewars with liquid nitrogen thermal shields are typically used and the cryogenic liquids must be replaced or recondensed as they boil off. Removing the liquid helium requirement simplifies the design of any SC magnet system. The discovery of high temperature superconductors has led to the development of magnets that can operate at liquid nitrogen temperatures (77 K) but presently these magnets are quite expensive, difficult to fabricate, and unable to produce the high magnetic fields possible with low temperature superconductors [18][19][20]. Liquid cryogenics can be avoided completely by conductively cooling the magnet coil with a cryogenic refrigerator or cryocooler. Modern Gifford-McMahon (GM) cycle cryocoolers with cooling capacities on the order of 1 W at 4.2 K have been used suc-

cessfully in recent conductively cooled SC magnet systems [21]. Conduction cooling is a novel aspect of the SC magnet subsystem for the AMRL. A schematic of a split pair, conduction cooled superconducting magnet system is shown in Figure 1.2.0b.

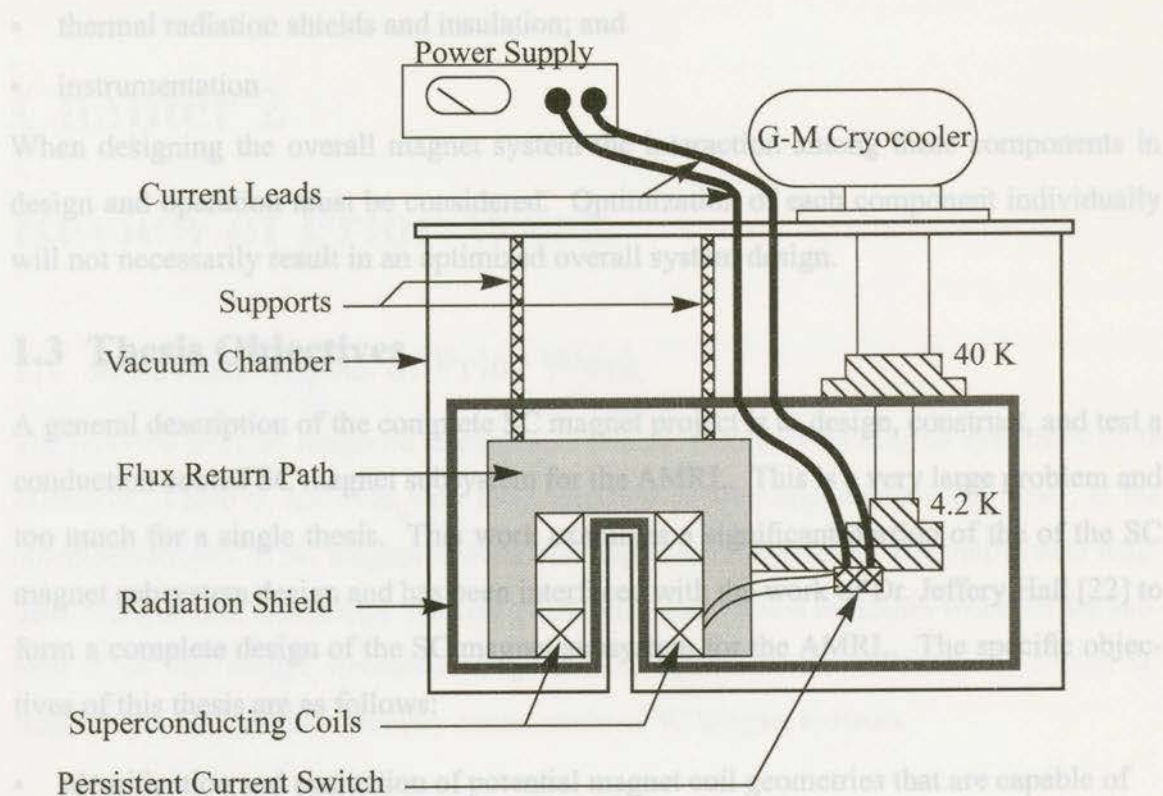


Figure 1.2.0b Schematic diagram of a conduction cooled superconducting magnet system.

There are many other components within a SC magnet system other than just the superconducting coil, power supply, and cooling system. The major components of the SC magnet subsystem for the AMRL are:

- superconducting coils;
- a power supply;
- current leads;
- a persistent current switch;
- quench detection and protection circuitry;
- a vacuum chamber and pump;

- structural supports;
- a flux return path;
- a refrigeration system;
- thermal radiation shields and insulation; and
- instrumentation

When designing the overall magnet system the interaction among these components in design and operation must be considered. Optimization of each component individually will not necessarily result in an optimized overall system design.

1.3 Thesis Objectives

A general description of the complete SC magnet project is to design, construct, and test a conduction cooled SC magnet subsystem for the AMRL. This is a very large problem and too much for a single thesis. This work examines a significant portion of the of the SC magnet subsystem design and has been interfaced with the work of Dr. Jeffery Hall [22] to form a complete design of the SC magnet subsystem for the AMRL. The specific objectives of this thesis are as follows:

- identification and evaluation of potential magnet coil geometries that are capable of meeting the magnetic field requirements of the AMRL;
- design and optimization of selected coil geometries and flux return path by magneto-static simulation in the presence of magnetic material;
- estimation of magnetic forces for structural design and analysis;
- thermal analysis of heat loads for design of the conduction cooling system; and
- identification of auxiliary components for the magnet subsystem.

Although the individual topics examined in this work have been examined by other researchers, this work represents a unique synthesis of these topics and their application to rotary AMR systems. It also presents the magnetic field simulation and winding design of a partial tokamak coil configuration. There is no published work, to date, that has examined the details of applying this magnet configuration to a rotary AMR.

Unfortunately, this classification method does not provide any information about the hardware design of the refrigeration devices. An alternate method of grouping, for design purposes, is to group these devices by the following factors:

- cycle type (Carnot, Ericsson, Brayton, or AMR);
- configuration (static, reciprocating, or rotating).

Chapter 2

Review of Prior Work

2.1 Relevant Topics of Prior Work

The reported work on magnetic refrigeration and superconducting magnet systems is quite extensive. There is, however, very little literature directly applicable to this work, in the combined subject of SC magnet systems for magnetic refrigerators. Beginning with magnetic refrigeration technology and coil geometries, this review examines works in the subjects of SC coil design, structural design of SC magnet systems, conductively cooled SC magnet systems, and the auxiliary components of SC magnet systems.

2.2 Magnetic Refrigeration (MR) Technology

Literature in the subject of magnetic refrigeration (MR) has been reviewed by Lacaze [23], Barclay [24][25], and Zhang et al. [26]. The focus of most work, as identified by Zhang et al. [26], has been in the areas of magnetic refrigerant materials development, theoretical studies of magnetic refrigeration and liquefaction, and experimental studies of magnetic refrigeration and liquefaction. It is the experimental works that are of interest because they provide insight into the hardware development of MR devices.

The common method of classifying these experimental works is by the temperature range spanned by the devices [23][24][25][26]. The reported temperature ranges are 0.1-1.5 K, 1.5-4.2 K, 4.2-20 K, 20-77 K, and near 300 K. Classification by this method is particularly good for defining the application of the device and selecting suitable magnetic refrigerants because the magnetocaloric effect of different refrigerants varies with temperature.

Unfortunately, this classification method does not provide any information about the hardware design of the refrigeration devices. An alternate method of taxonomy, for design purposes, is to group these devices by the following factors:

- cycle type (Carnot, Ericsson, Brayton, or AMR);
- temperature range; and,
- configuration (static, reciprocating, or rotating).

The magnet design of an MR device depends upon the cycle type because the magnetization process is different for each cycle. The magnetization of the refrigerant, during each process of an MR cycle, is best described using a temperature-entropy diagram. Segments of the idealized T-S diagrams of various MR cycles are shown in Figure 2.2.0a. Carnot

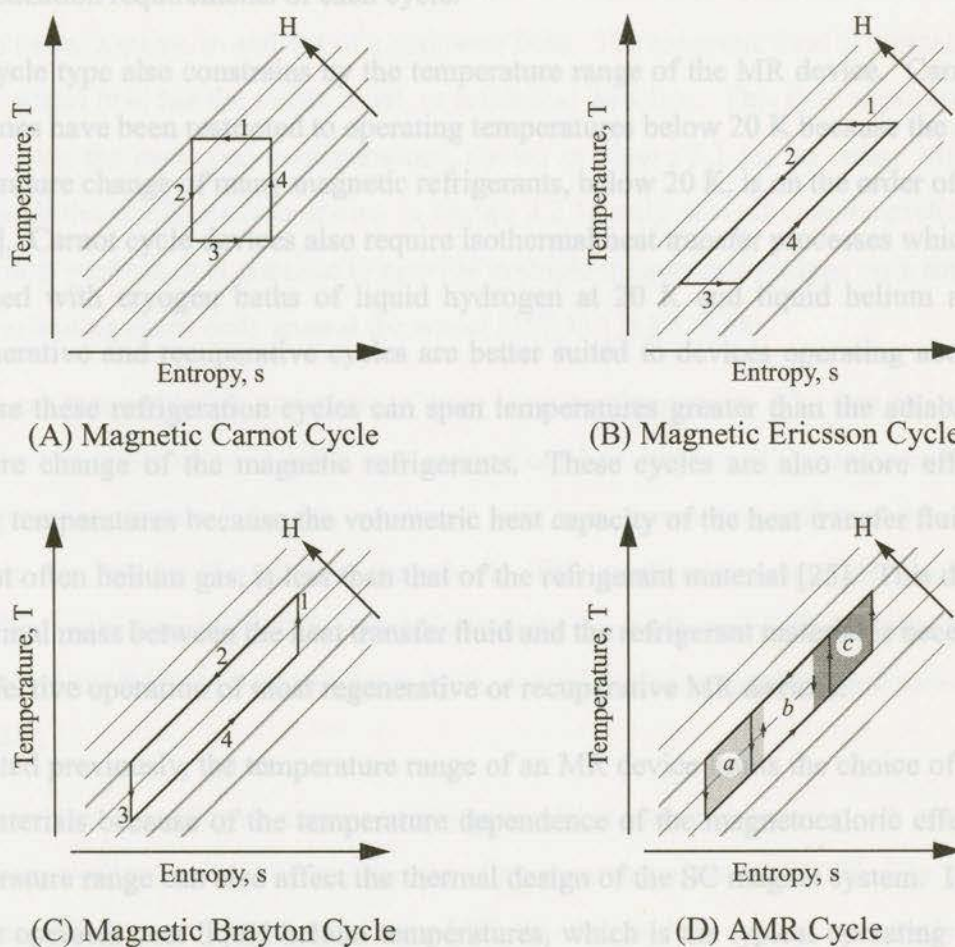


Figure 2.2.0a Temperature entropy diagrams of the magnetic refrigerant material during different magnetic refrigeration cycles.

cycle devices require varying applied magnetic fields during both the isothermal and isentropic processes of the cycle. Ericsson cycles only require varying fields during the isothermal processes. Lastly, both the Brayton and AMR cycles require isentropic magnetization/demagnetization followed by isofield heat transfer processes. These last two cycles are similar in their magnetization requirements but differ in their thermodynamics. A regenerative Brayton cycle uses an external regenerator while the magnetic working material of an AMR cycle also functions as the regenerator material. The exact thermodynamic theory behind the AMR cycle is still being developed. The newest advance by Hall et al. [16] states that the solid elements in the regenerator perform overlapping Brayton cycles, as shown by cycles *a*, *b*, and *c* in Figure 2.2.0a-D, while transferring heat to and from the fluid. The magnet design of an MR device must reflect these magnetization requirements of each cycle.

The cycle type also constrains by the temperature range of the MR device. Carnot cycle machines have been restricted to operating temperatures below 20 K because the adiabatic temperature change of many magnetic refrigerants, below 20 K, is on the order of 10 to 20 K [25]. Carnot cycle devices also require isothermal heat transfer processes which can be obtained with cryogen baths of liquid hydrogen at 20 K and liquid helium at 4.2 K. Regenerative and recuperative cycles are better suited to devices operating above 15 K because these refrigeration cycles can span temperatures greater than the adiabatic temperature change of the magnetic refrigerants. These cycles are also more effective at higher temperatures because the volumetric heat capacity of the heat transfer fluid, which is most often helium gas, is less than that of the refrigerant material [25]. This difference in thermal mass between the heat transfer fluid and the refrigerant material is necessary for the effective operation of most regenerative or recuperative MR devices.

As stated previously, the temperature range of an MR device limits the choice of refrigerant materials because of the temperature dependence of the magnetocaloric effect. This temperature range can also affect the thermal design of the SC magnet system. If the MR device operates near liquid helium temperatures, which is the typical operating temperature of most SC magnets, the MR device may be used to refrigerate the magnet system. There are many reported cases of MR devices that self-refrigerate their SC magnet sys-

tems [27][28][29][30][31][32][33][38]. If this is not possible, the SC magnet system must have a separate refrigeration system. However, Barclay and Stewart [34] have proposed that a separate parasitic MR device could be used to effectively refrigerate the SC magnet system regardless of the temperature range of the main MR device.

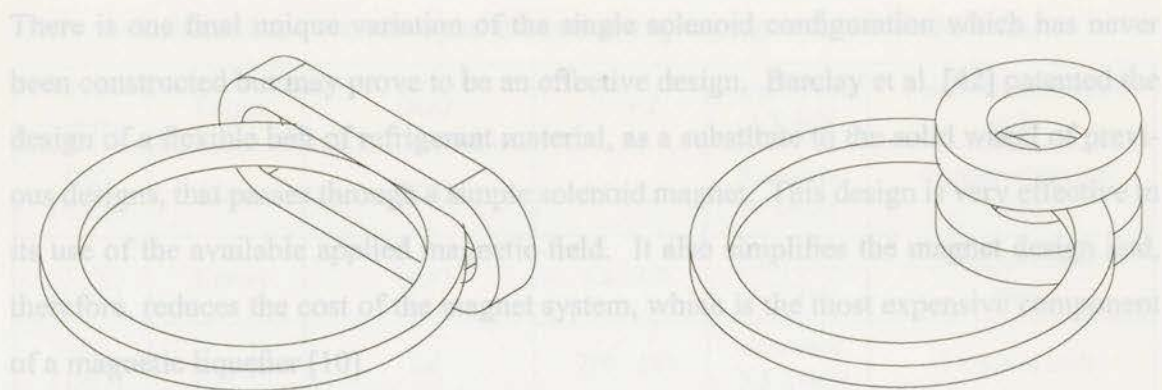
It is the configuration that is the most important factor when considering the design of the SC magnet subsystem. Static and reciprocating devices typically employ a simple solenoid coil design but there are many possible coil designs available to rotating MR devices. As the AMRL is a rotating device, prior work involving rotating MR devices provides the most relevant magnet design information.

2.2.1 Magnet Configurations for Rotary MR Devices

The refrigerant material of a rotary MR device is fashioned in a circular form and rotated, as the name implies, in and out of a magnetic field. The magnetic field is typically applied to the wheel in either the radial, axial, or azimuthal direction. This field application can be done using the basic coil configurations, shown in Figure 2.2.1a, for rotary MR devices. Although the configurations shown in Figure 2.2.1a only provide one magnetized region per wheel rotation, it is possible to provide multiple magnetized regions on a single wheel by distributing more coils around the wheel [30][35][36][37][38].

There are many possible variations to these basic configurations. The first reported rotary MR device, constructed in 1977 by a group from Los Alamos [27], used a racetrack coil configuration, Figure 2.2.1a-A, combined with a compensating coil to reduce the stray field in the "no field" region of the wheel. This configuration was also used later by Toshiba researchers [32]. Other variations of the racetrack coil include a tilted coil [33], which applies the field between the radial and axial directions, and stacked racetrack coils [35][44].

Variations on the split pair magnet configuration have included systems with rotating coils [30][36], ovalized coils [38], and the use of permanent magnets [37][39]. The permanent magnet MR device by Kirol and Dacus [37] also oriented the split pair to apply the mag-



(A) Racetrack Configuration

(B) Split Pair Configuration

A compilation of the literature regarding rotary MR devices provides a good overview of the design trends in this field since the development of the first device in 1977. Table 2.2.2a lists the general design factors of real and ideal rotary MR devices. The design trends have been adopted and adapted from a more detailed survey of rotary MR devices by Kulkarni and Barclay [43].



(C) Single Solenoid Configuration

(D) Partial Tokamak Configuration

Figure 2.2.1a Basic coil configurations for rotary magnetic refrigeration devices.

netic field in the radial direction of the wheel. Although a unique design, this device unfortunately suffered a catastrophic failure because the wheel construction was not robust enough to withstand the magnetic forces.

The partial tokamak design is a variation on the single solenoid configuration as both produce an azimuthally applied magnetic field. The concept of the solenoid design was first presented by Barclay and Steyert [40] and the partial tokamak configuration by Astronautics Corporation of America [41]. At present, however, neither magnet configuration has ever been constructed for an MR device. The partial tokamak configuration could also be modified to become a bent solenoid or a partial torus but there is no evidence of this design concept in any of the reviewed literature.

[40]	Carroll	He-3	4.2 K	Solenoid	racetrack, compressor coil
[41]	Carroll	He-3	4.2 K	Solenoid	solenoid covering entire wheel, refrigeration based on azimuthally applied field
[43]	Carroll	He-3	4.2 K	Split Pair	racetrack, compressor coil
[44]	Carroll	He-3	4.2 K	Split Pair	racetrack, compressor coil
[45]	Carroll	He-3	4.2 K	Split Pair	racetrack, compressor coil
[46]	Carroll	He-3	4.2 K	Split Pair	racetrack, compressor coil
[47]	Carroll	He-3	4.2 K	Split Pair	racetrack, compressor coil
[48]	Carroll	He-3	4.2 K	Split Pair	racetrack, compressor coil
[49]	Carroll	He-3	4.2 K	Split Pair	racetrack, compressor coil
[50]	Carroll	He-3	4.2 K	Split Pair	racetrack, compressor coil
[51]	Carroll	He-3	4.2 K	Split Pair	racetrack, compressor coil
[52]	Carroll	He-3	4.2 K	Split Pair	racetrack, compressor coil
[53]	Carroll	He-3	4.2 K	Split Pair	racetrack, compressor coil
[54]	Carroll	He-3	4.2 K	Split Pair	racetrack, compressor coil
[55]	Carroll	He-3	4.2 K	Split Pair	racetrack, compressor coil
[56]	Carroll	He-3	4.2 K	Split Pair	racetrack, compressor coil
[57]	Carroll	He-3	4.2 K	Split Pair	racetrack, compressor coil
[58]	Carroll	He-3	4.2 K	Split Pair	racetrack, compressor coil
[59]	Carroll	He-3	4.2 K	Split Pair	racetrack, compressor coil
[60]	Carroll	He-3	4.2 K	Split Pair	racetrack, compressor coil
[61]	Carroll	He-3	4.2 K	Split Pair	racetrack, compressor coil
[62]	Carroll	He-3	4.2 K	Split Pair	racetrack, compressor coil
[63]	Carroll	He-3	4.2 K	Split Pair	racetrack, compressor coil
[64]	Carroll	He-3	4.2 K	Split Pair	racetrack, compressor coil
[65]	Carroll	He-3	4.2 K	Split Pair	racetrack, compressor coil
[66]	Carroll	He-3	4.2 K	Split Pair	racetrack, compressor coil
[67]	Carroll	He-3	4.2 K	Split Pair	racetrack, compressor coil
[68]	Carroll	He-3	4.2 K	Split Pair	racetrack, compressor coil
[69]	Carroll	He-3	4.2 K	Split Pair	racetrack, compressor coil
[70]	Carroll	He-3	4.2 K	Split Pair	racetrack, compressor coil
[71]	Carroll	He-3	4.2 K	Split Pair	racetrack, compressor coil
[72]	Carroll	He-3	4.2 K	Split Pair	racetrack, compressor coil
[73]	Carroll	He-3	4.2 K	Split Pair	racetrack, compressor coil
[74]	Carroll	He-3	4.2 K	Split Pair	racetrack, compressor coil
[75]	Carroll	He-3	4.2 K	Split Pair	racetrack, compressor coil
[76]	Carroll	He-3	4.2 K	Split Pair	racetrack, compressor coil
[77]	Carroll	He-3	4.2 K	Split Pair	racetrack, compressor coil
[78]	Carroll	He-3	4.2 K	Split Pair	racetrack, compressor coil
[79]	Carroll	He-3	4.2 K	Split Pair	racetrack, compressor coil
[80]	Carroll	He-3	4.2 K	Split Pair	racetrack, compressor coil
[81]	Carroll	He-3	4.2 K	Split Pair	racetrack, compressor coil
[82]	Carroll	He-3	4.2 K	Split Pair	racetrack, compressor coil
[83]	Carroll	He-3	4.2 K	Split Pair	racetrack, compressor coil
[84]	Carroll	He-3	4.2 K	Split Pair	racetrack, compressor coil
[85]	Carroll	He-3	4.2 K	Split Pair	racetrack, compressor coil
[86]	Carroll	He-3	4.2 K	Split Pair	racetrack, compressor coil
[87]	Carroll	He-3	4.2 K	Split Pair	racetrack, compressor coil
[88]	Carroll	He-3	4.2 K	Split Pair	racetrack, compressor coil
[89]	Carroll	He-3	4.2 K	Split Pair	racetrack, compressor coil
[90]	Carroll	He-3	4.2 K	Split Pair	racetrack, compressor coil
[91]	Carroll	He-3	4.2 K	Split Pair	racetrack, compressor coil
[92]	Carroll	He-3	4.2 K	Split Pair	racetrack, compressor coil
[93]	Carroll	He-3	4.2 K	Split Pair	racetrack, compressor coil
[94]	Carroll	He-3	4.2 K	Split Pair	racetrack, compressor coil
[95]	Carroll	He-3	4.2 K	Split Pair	racetrack, compressor coil
[96]	Carroll	He-3	4.2 K	Split Pair	racetrack, compressor coil
[97]	Carroll	He-3	4.2 K	Split Pair	racetrack, compressor coil
[98]	Carroll	He-3	4.2 K	Split Pair	racetrack, compressor coil
[99]	Carroll	He-3	4.2 K	Split Pair	racetrack, compressor coil
[100]	Carroll	He-3	4.2 K	Split Pair	racetrack, compressor coil

There is one final unique variation of the single solenoid configuration which has never been constructed but may prove to be an effective design. Barclay et al. [42] patented the design of a flexible belt of refrigerant material, as a substitute to the solid wheel of previous designs, that passes through a simple solenoid magnet. This design is very effective in its use of the available applied magnetic field. It also simplifies the magnet design and, therefore, reduces the cost of the magnet system, which is the most expensive component of a magnetic liquefier [10].

2.2.2 Summary of Rotary MR Devices

A compilation of the literature regarding rotary MR devices provides a good overview of the design trends in this field since the development of the first device in 1977. Table 2.2.2a lists the reported general design factors of real and conceptual rotary MR devices. This table has been adapted and updated from a more general survey of all MR devices by Kral and Barclay [43].

Table 2.2.2a: Summary of literature regarding rotary MR devices.

Ref.	Cycle Type	Refrigerant Material	Temp. Span (K)	Magnet Config.	Comments
[27] (1977)	Carnot	$Gd_2(SO_4)_3 \cdot 8H_2O$	2.1 - 4.2	Racetrack, 3.1 T field	compensating coil used
[39] (1977)	Brayton	Gd	290 - 294	Split Pair, 1.2 T field	permanent magnets, cycle erroneously reported as Stirling
[28] (1980)	Carnot	$DyPO_4$ (crystal)	4 - 20	Solenoid, 7 T field	solenoid covering entire wheel, refrigeration based on anisotropic nature of $DyPO_4$ crystal
[45] (1985)	Carnot	Gadolinium Gallium Garnet (GGG)	4.2 - 15	Split Pair, 4 T field	net cooling load of 0.9 W with 4 T field, some gas sealing problems
[29] (1985)	Carnot	GGG	4.5 - 15	Racetrack, 5+ T field	conceptual design only, compensating coil used
[36] (1985)	Carnot	N/A	1.8 +	Split Pair	patent, axial & radial applied field, rotating SC coils

Table 2.2.2a: Summary of literature regarding rotary MR devices.

[30] (1986)	Carnot	GGG	2 - 4.2	Split Pair, 3 T field	3 pairs of rotating SC coils
[32] (1986)	Carnot	GGG	4.2 - 8.2	Racetrack, 4 T field	compensating coil used
[31] (1986)	Carnot	GGG	1.8 - 4.2	Racetrack, 3 T field	2 compensating coils used
[44] (1987)	Brayton	Gd	290 - 297	Racetrack, 3.5 T field	3 stacked coils
[42] (1987)	AMR	ferro or paramag- netic material	12 - 77	Solenoid	patent, flexible belt of refrigerant material
[33] (1988)	Carnot	GGG	4.2 - 11.5	Racetrack, 4.5 T field	racetrack coil tilted between axial and radial directions
[37] (1988)	Ericsson	Gd	~ 300	Split Pair, 0.9 T field	recuperative cycle, 4 pairs of permanent magnets, radial applied field, device failed during opera- tion
[41] (1988)	Carnot	GGG	13.8 - 20.2	Partial Tokamak	conceptual design only, 50 kW refrigera- tion power
[38][46] (1990)	Carnot	GGG	4.2 - 15	Split Pair, 3 T field	2 pairs of oval shaped SC coils, conduc- tively cooled coils
[35] (1993)	AMR	N/A	N/A	Racetrack	patent, 2 sets of stacked SC coils

All of the constructed rotary MR devices, except one, used racetrack or split pair magnet configurations. The exception, designed by a Los Alamos group [28], was not based on the concept of a wheel with magnetized and non-magnetized sections. Instead, the entire wheel was placed in a uniform magnetic field and refrigeration was based upon the anisotropic nature of the crystalline refrigerant material.

The solenoid and partial tokamak configurations are coupled with the mechanical design of the AMR. This means that the AMR ring, and its associated components, must be constructed in at least two pieces for assembly. The racetrack and split pair offer the advantage of physically decoupling the wheel from the magnet design. For this reason these

configurations are preferred over the solenoid and partial tokamak configuration in previously reported MR devices. The racetrack and split pair, however, do suffer from some disadvantages.

It is well recognized [45] that, for a split pair magnet configuration, the applied field in the gap, where the wheel rotates, is less than the field in the center of the individual coils. All of the stationary split pair designs, [37][39][45], reduced this problem by using a soft iron flux return path to concentrate the magnetic field. Another problem is that the maximum applied field of constructed devices may be lower than the designed maximum field. Barclay and Steyert [44] designed a racetrack coil to produce 6 T but the actual magnet only produced 3.5 T. They found that the peak fields in the corners of the racetrack were higher than planned and caused premature quenching of the magnet at low operating currents. This problem is best minimized by using presently available computational magnetic modelling, which is more advanced than was available to Barclay and Steyert.

A final concern, in the design of any magnet system for a rotary MR device, is the applied field profile. Although applying the highest possible magnetic field to the magnetized section of the wheel provides the largest possible magnetocaloric effect, minimizing the applied field on the non-magnetized section of the wheel also increase the effectiveness of the MR device. This is the reason that many designs, [27][29][31][32], employ compensating coils. The uniformity of the field is also important, particularly for AMR cycle systems, because fluctuations in the applied field can reduce the effectiveness of an MR device [15].

2.3 Superconducting (SC) Coil Design

The key design issues of any SC magnet system are identified by Iwasa [47] as the following:

- *Magnetic field.* The SC coil must provide a magnetic field that satisfies the spatial distribution and temporal variation requirements of the design.
- *Conductor specification.* The overall cost of a SC magnet system can be influenced to a large extent by the cost of the superconductor. It is impor-

tant to optimize the winding so that the field requirements can be met with the minimum amount of conductor.

- *Protection.* In the event the magnet is driven into the normal state, it must remain undamaged and be capable of being energized to its operating point repeatedly.
- *Mechanical integrity.* The magnet must be structurally strong to withstand the large magnetic stresses, both under operating and fault conditions.
- *Operational reliability.* The magnet must be stable to reach and stay at its operating point reliably.
- *Cryogenics.* It requires power to create and maintain the cryogenic environment necessary for SC magnets. It is important to try to minimize this power requirement.

The issues of magnetic field, conductor specification, protection, and mechanical integrity directly affect the coil design. The protection and mechanical integrity issues, however, also influence the electric circuit and the external structure development. The last two issues, operational reliability and cryogenic, are interdependent and relate to the auxiliary components and refrigeration system design. It is the first two issues that are most important to the coil design.

Practical modelling of the magnetic field provided by the coil geometries shown in Figure 2.2.1a can only be accomplished by computer simulation because these coil shapes are complex, there are multiple coils in varying spatial orientation, and magnetic material is present. The split pair coil by Rowe et al. [38] is the result of numerical modelling with successive design modifications. There are, however, analytical and empirical methods, which are presented by Wilson [17], for calculating the magnetic field profiles of solenoids without the presence of magnetic material. Examining the field profiles of simple solenoids can provide a good understanding of the factors which influence the spatial distribution of magnetic fields and the methods for minimizing the conductor volume.

[50] present a detailed optimization algorithm for solenoids which also includes the cost of the wire.

The classic analytical method of coil optimization, presented by Wood [48] and Thomas and Bright [49], involves minimizing the conductor volume of a solenoid with a rectangular cross section and a uniform current density. Although useful for simple coils, this is not the most effective optimization technique for high field magnets. The maximum field within a solenoid is located at the inner radius of the coil and the magnitude of the field decreases in the radial direction through the windings as shown in Figure 2.3.0a. There-

coils for the AMRL magnet system are optimized in this fashion.

Optimization and realistic modelling of a SC coil also requires valid information regarding the T-J-H relationship of the superconductor. The relationship between critical current and applied field at liquid helium temperature, 4.2 K, is available for commercial SC wires from their respective manufacturers. If, however, the critical current information is needed at temperatures other than 4.2 K, the manufacturer's information can be adjusted using the empirical relation presented by Labadie [17], in Equation (2.3.0a) and Equation (2.3.0b), from Iwamoto [17], which assumes the critical current is a linear function of temperature.

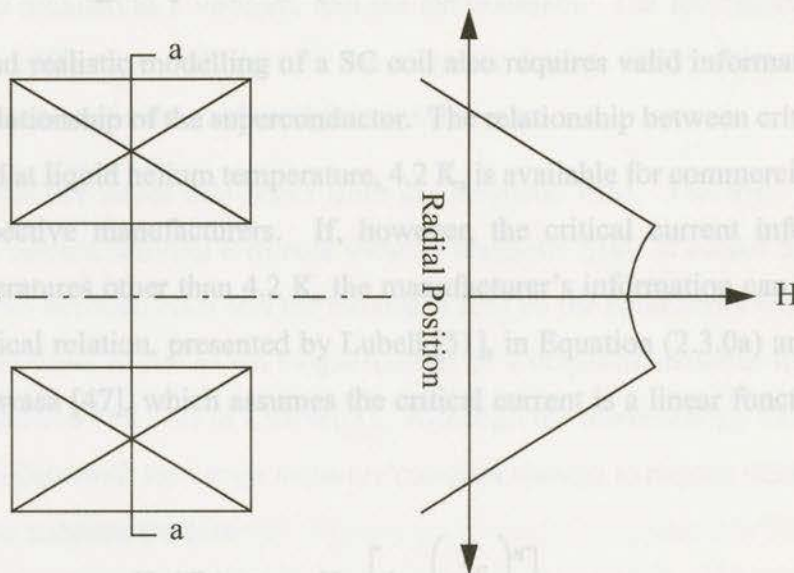


Figure 2.3.0a Schematic profile of magnetic field through a solenoid at section a-a.

fore, the conductor material in the first winding is subjected to a higher field than the other windings and constrains the overall current density of the coil by the T-J-H relationship of the superconducting material. By using multiple sections of winding, each operating near the maximum current density allowed by the maximum local field, more of the conductor operates near its design limit so less material is needed. This winding technique usually involves wrapping a coil bobbin with sections of successively smaller diameter wire and connecting them in series. Then, for a fixed operating current, the inner sections have a low current density and the outer sections have a high current density. Wilson [17] gives a good general description of this coil sectioning technique while Ishiyama and Shimizu [50] present a detailed optimization algorithm for solenoids which also includes the cost of the wire.

Practical optimization by sectioning, of more complex coil shapes such as racetrack coils or ovalized coils, is done iteratively. This process involves numerically modeling a sectioned coil, examining the maximum fields within the winding sections, and confirming that the current density of each winding is within its operational limit for the calculated field. If the current density is beyond its critical limit or below its limit, which means that the winding is under-utilized, the current is adjusted and the coil is modelled again. The coils for the AMRL magnet system are optimized in this fashion.

Optimization and realistic modelling of a SC coil also requires valid information regarding the T-J-H relationship of the superconductor. The relationship between critical current and applied field at liquid helium temperature, 4.2 K, is available for commercial SC wires from their respective manufacturers. If, however, the critical current information is needed at temperatures other than 4.2 K, the manufacturer's information can be adjusted using the empirical relation, presented by Lubell [51], in Equation (2.3.0a) and Equation (2.3.0b), from Iwasa [47], which assumes the critical current is a linear function of temperature.

$$\mu_0 H_c(T_c) = \mu_0 H_{co} \left[1 - \left(\frac{T_c}{T_{co}} \right)^n \right] \quad (2.3.0a)$$

$$J(T) = J_{test} \left(\frac{T_c - T}{T_c - T_{test}} \right) \quad (2.3.0b)$$

According to Lubell [51], when using Equation (2.3.0a) for NbTi conductors, $n = 1.7$ and the critical values of $\mu_0 H_{co} = 14.5$ T and $T_{co} = 9.2$ K provide the best results. The appropriate values for Nb₃Sn conductors are $n = 0.62 \sim 0.72$, $\mu_0 H_{co} = 27.9$ T, and $T_{co} = 18.3$ K according to Iwasa [47]. The T_c from Equation (2.3.0a) can then be used in Equation (2.3.0b) along with the manufacturer's tested critical values of J_{test} and T_{test} for a given applied field to find the critical current density at a chosen temperature.

2.4 Structural Design of SC Magnet Systems

There are three structural elements within a SC magnet system; the internal structure of the coil, the external structure supporting the coil, and the container which isolates the system from the environment. These structures are meant to support the forces produced by the magnetic field, thermal contraction of the components, any pre-loading of components during assembly, the weight of the entire system, and the pressure differential between the system, which is isolated in a vacuum, and the environment. The mechanical loads are generally not as difficult to calculate as the magnetic loads. Good estimates of these forces are necessary to ensure a safe and functional design.

There are two distinct forces that result from the magnetic field. The first, the Lorentz force, acts upon current carrying elements within a magnetic field. It causes the attractive or repulsive forces between coils and the internal forces on the conductors within a single coil. The second force is due to the magnetization of a magnetic material within a field gradient (see Equation (1.1.3.a) in Chapter 1). Although the methodology for calculating these forces is understood, the vector sums are complex enough to require numerical solutions for even the simplest models.

Barclay et al. [52] present a good analysis of the material magnetization force of Gadolinium Gallium Garnet within a 6 T field for both a reciprocating and rotary MR device. The results of this analysis show that the internal force on the refrigerant material is approximately ten times larger than the force required to move the material through the field. This smaller, net force on the material also results in an equal and opposite force on the coils. The external structure must be strong enough to support this force on the coils. Although these results are for a very specific case, they do show that the magnetic forces within the material are much larger than the net external force so precautions must be taken to prevent mechanical failure of the refrigerant material.

The effects of the Lorentz force on the coil design is discussed thoroughly in the textbooks by Wilson [17] and Iwasa [47]. Within a coil, the Lorentz force produces a outward radial force that results in radial and hoop stresses (σ_r , σ_θ) within the coil windings as seen in

Figure 2.4.0a. There is also an axial compressive force within a coil due to the field direction at the ends of a coil. These forces can be calculated analytically for simple solenoids but are calculated numerically for more complex coil shapes.

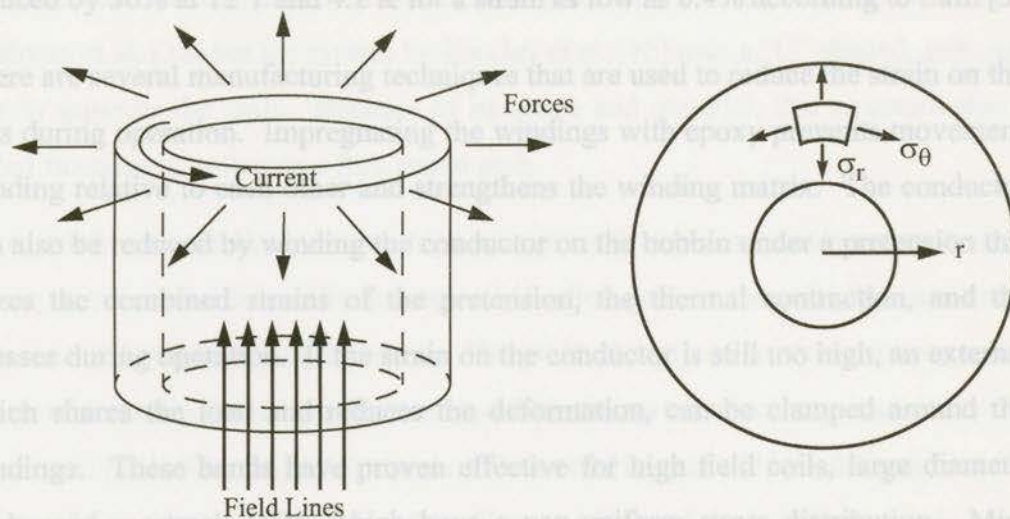


Figure 2.4.0a Schematic of the Lorentz forces and radial and hoop stresses on a solenoid.

In general, the stress distribution within operating solenoids resembles that found in thick walled pressure vessels. Assuming the properties of the conductor matrix are isotropic, the stress distribution in a solenoid can be described by the equilibrium equation, Equation (2.4.0a), from Mitchell and Mszanowski [53]:

$$r \frac{d\sigma_r}{dr} + \sigma_r - \sigma_\theta = -J\mu_0 H r \quad (2.4.0a)$$

Because the magnetic field is proportional to current density [17], the stresses, according to Equation (2.4.0a), scale with $(\mu_0 H)^2$ and the radius of the coil. This means that internal coil structure is most important for high field coils and large diameter coils.

The coil stresses exist within the conductor and the epoxy-glass matrix that binds the conductors together. Overstressing the conductor can destroy the coil but the strain on the conductor is also of concern. The current density of the wire is affected by the wire strain in a similar fashion to the temperature and field effect on the current density. If the strain

is too high, the current density and, therefore, the applied field is degraded from the design value. The magnitude of this effect also depends upon the conductor material, local field, and operating temperature. The critical current of a Nb_3Sn conductor, for example, can be reduced by 30% at 12 T and 4.2 K for a strain as low as 0.4% according to Ekin [54].

There are several manufacturing techniques that are used to reduce the strain on the windings during operation. Impregnating the windings with epoxy prevents movement of the winding relative to each other and strengthens the winding matrix. The conductor strain can also be reduced by winding the conductor on the bobbin under a pretension that minimizes the combined strains of the pretension, the thermal contraction, and the hoop stresses during operation. If the strain on the conductor is still too high, an external band, which shares the load and reduces the deformation, can be clamped around the outer windings. These bands have proven effective for high field coils, large diameter solenoids, and racetrack coils, which have a non-uniform stress distribution. Minas and Laskaris [55] reported using stainless steel and aluminum bands around large diameter coils for MRI applications. Similarly, Jüngst et al. [56] used an iron form to contain racetrack coils for a magnetic ore separator and Vermilyea [57] designed an aluminum structure encasing conduction cooled racetrack coils for a maglev vehicle. Vermilyea's design is particularly interesting because the aluminum banding also acts as a heat conduction path for the conduction cooling of the coils.

In addition to the causing internal forces within a coil, the Lorentz force also acts between coils. This is only a concern for systems with multiple coils such as the split pair and the partial tokamak configurations. The structure that separates these coils must be in direct contact with the coils so it must also be as cold as the coils. The physical properties of many materials change significantly at cryogenic temperatures so the selection of structural materials is an important design factor. In general, the yield strength of most materials increases while the impact strength, ductility, and fatigue strength decrease at cryogenic temperatures. Plain carbon steels are particularly notorious for low temperature embrittlement and, therefore, not used in cryogenic equipment. The most common cryogenic structural materials are steels with at least a 9 percent nickel content, aluminum, and glass reinforced plastics [58][59]. In literature mentioning coil separation structure,

Minas and Laskaris [55] use a stainless steel structure while van der Laan et al. [60] use aluminum cylinders. Both of these systems access the field in the axial direction of the coils, similar to the partial tokamak configuration, so their structure is only applicable to a partial tokamak configuration. There is little mention of the structure of the split pair coils by Rowe et al. [38] but the system by Barclay et al. [45] uses a "C" shaped, soft iron structure to separate the coils. Because of its shape and material, this structure also has the added function of acting as a flux return path.

Glass reinforced plastic and other high strength polymeric materials are very well suited for the structure that thermally isolates cold bodies, such as the coils, because these materials have low thermal conductivities. The yield strength of many composite materials is comparable to their metal counterparts but their thermal conductivity is an order of magnitude lower [61]. The magnet systems of Minas and Laskaris [55] and Vermilyea [57] both use tensile supports of epoxied carbon fibre and Duband et al. [62] suspended cryogenic systems with braided Kevlar cords. Reducing the heat leak through this external support structure is especially important for conduction cooled magnet systems because of the limited cooling capacity of the cryocooler.

2.5 Conductively Cooled SC Magnet Systems

Conductively cooled magnet systems avoid the need for refrigeration with liquid cryogens by thermally connecting a SC coil to a low temperature heat sink, such as the cold head of a two stage Gifford McMahon (GM) cryocooler. Such systems are desirable because the lack of liquid cryogens allows the magnet system to be operated literally with the push of a button.

Hoening [63] presented one of the first conceptual designs of a conduction cooled superconducting magnet in 1986. He proposed refrigerating a Nb_3Sn coil with a standard two stage GM cryocooler to an operating temperature of 13 K and estimated that the coil would develop an applied magnetic field of 3.3 T with a refrigeration load of 2.5 W at the operating temperature. Hoening's conceptual design is very similar to the first operational conduction cooled system, presented by Furuyama et al. [64] in 1989, which developed a maximum field of 2.4 T at 14 K using Nb_3Sn tape coils cooled by two GM refrigerators.

At the same time, van der Laan et al. [60][65] constructed a working 1:3 scale model MRI magnet system that was also cooled with two conventional GM cryocoolers. The coils of van der Laan's system were also made of Nb₃Sn producing a 1 T field at 12 K. These early systems proved that conduction cooling was possible but they were unfortunately restricted to low fields and Nb₃Sn conductors by their relatively high operating temperatures.

The lowest operating temperature of conventional GM refrigerators is slightly below 10 K because, at these temperatures, the volumetric heat capacity of the helium working gas becomes much greater than that of the most common second stage regenerator material, lead. The development of practical, low temperature, high heat capacity regenerator materials using rare earth materials by Hashimoto et al. [66] led to Kuriyama et al.'s [67] construction of the first 4.2 K GM refrigerator. Kuriyama's 4.2 K cryocooler, which used Er₃Ni particles in the second stage regenerator, was soon followed by the development of the next conduction cooled SC magnet by Masuyama et al. [68]. This magnet system was novel because it used the less expensive NbTi superconductor and operated at 6 K producing a 5.4 T field. Like the previous systems however, Masuyama's system employed two cryocoolers. The first cooled the SC coils and the second cooled the heat shields and the copper current leads. The heat load from the current leads was too great to be absorbed by a single refrigerator as the 4.2 K cryocooler only had a 500 mW capacity at 5.4 K [68].

The discovery of even better low temperature passive regenerator materials, such as ErNi_{0.9}Co_{0.1} by Onishi et al. [69] and Er₃Co and Er_{0.9}Yb_{0.1}Ni by Yabuki et al. [70], has led to the development of refrigerators with ever increasing cooling powers. At 4.2 K, the cryocoolers of Kuriyama et al. [71] and Tsukagoshi et al. [72] have a cooling power of just over 1 W while the device by Satoh et al. [73] is capable of 1.5 W of refrigeration. The erbium based alloys used in all of these cryorefrigerators have the unfortunate property of being extremely brittle so the reliability of these machines is diminished. Using the more ductile material neodymium instead of erbium alloys, Chafe et al. [74] modified the GM cryocooler described by Riedy [75] to produce a 4.2 K refrigerator with a cooling power roughly has a thermal conductivity of 300 W/m·K at 4.2 K [85]. As for the mechanical connections, they can be either soldered or pressed, such as bolted flanges.

of 500 mW. Although this device does not have the cooling capacity of machines using erbium based alloys, it is more reliable and recently became commercially available from the Balzers corporation [76].

The next step in the progress of conduction cooled magnet systems was the use of high Tc superconducting current leads between the first (~ 50 K) and second (4.2 K) stages of the cryocooler. Replacing the copper current leads reduces the thermal conduction and removes the ohmic heating loads so that only one cryocooler is necessary for most SC magnet systems. Takahashi et al. [77] constructed the first conduction cooled SC magnet system using a single 4.2 K cryocooler. Their NbTi coil produced a 7.7 T field at 4.1 K and they estimated the heat load to be 166 mW at this temperature.

Other conduction cooled magnet systems, using high Tc current leads, have been developed [78][79][80][81][82] but all have an operating temperature of approximately 10 K. At present, the only other 4.2 K, conduction cooled SC magnet is a 6 T NbTi system described by Urata et al. [83]. In summary, the only reported liquid helium temperature conduction cooled SC magnets have been the systems by Rowe et al. [38], Masuyama et al. [68], Takahashi et al. [77], and Urata et al. [83]. Rowe's system is self cooling using a magnetic refrigerator, Masuyama's device requires two cryocoolers, and Takahashi's and Urata's systems both use a single 4.2 K GM cryocooler. The SC magnet system for the AMRL is similar to these last two systems as it attempts to use a single 4.2 K cryocooler and high Tc current leads.

Yazawa et al. [84], who discuss the cooling structure of Urata's system, and Takahashi et al. [77] both observe that the temperature difference between the SC coil and the cold flange of the cryocooler must be minimized to maintain the coil at the lowest possible temperature. This is done by making the conduction path out of high thermal conductivity material, minimizing the length of the conduction path, minimizing the number of mechanical connections in the conduction path, and minimizing the thermal contact resistance at all connections. The most common high conductivity material is oxygen free high conductivity (OFHC) copper which, for a residual resistivity ratio (RRR) of 50, roughly has a thermal conductivity of 300 W/m·K at 4.2 K [85]. As for the mechanical connections, they can be either soldered or pressed, such as bolted flanges.

According to Radebaugh [86], soldered connections provide a lower thermal contact resistance than pressed joints; care must be taken, however, in choosing the type of solder. Some solders, such as lead and lead-tin, become superconducting just above 4.2 K so their thermal conductivity decreases significantly. Fortunately, these materials also have a low critical applied field so that the superconducting state is destroyed if a small field is present. Radebaugh claims that connections made with indium solder have a higher thermal conductance than alloy solders and it does not become superconducting until 3.4 K. Indium is also the preferred thermal gasket material for pressed copper connections. Both Deutsch [87] and Salerno et al. [88] agree that the thermal contact resistance of a pressed copper-indium-copper joint is lower than a pressed copper-copper joint. Salerno also observes that Apiezon-NTM grease [89], commonly used in cryogenic work, provides an even lower contact resistance than indium but care must be taken in preparing the connection. Salerno et al. [88] found the thermal conductance of pressed copper contacts to be 95 mW/cm²·K for copper-indium-copper and 195 mW/cm²·K for copper-grease-copper at a pressure of 8.2 MPa (~ 1200 psi) and at 4.2 K while Radebaugh [86] measured a conductance of 30 W/cm²·K for indium soldered joints at this temperature. Salerno's value for pressed copper-indium-copper contacts may be low because the pressure was applied to the joint at 4.2 K and indium is not very flexible at this temperature. At room temperature, indium is very soft and will cold weld to connections under pressure. It is possible that cold welded connections may have conductances approaching those of soldered joints. From these values it is obvious that, for the conduction path of conductively cooled SC magnet systems, solder connections should be used when possible and pressed connections should have as large a surface area as possible.

The greatest general concern of conductively cooled SC magnet systems is the reduction of the heat loads on the system because of the limited cooling power of the cryocooler. As mentioned previously, the use of polymeric structural materials reduces the conductive losses and using high T_c current leads reduces both ohmic heating and conductive losses. The other major loss mechanism is thermal radiation and it is reduced by the use of radiation shields, which are thermally anchored to the first stage of the cryocooler, and good insulation materials.

The purpose of the radiation shield is to prevent thermal radiation between room temperature and the liquid helium temperature bodies by intercepting the radiation at an intermediate temperature, usually around 50 K. In general, the thermal radiation load, \dot{Q}_{rad} , between a body enclosed in a vacuum vessel and the inner surface of the vessel, described in Equation (2.5.0a) from Barron [58], depends heavily on the temperature difference between the bodies as well as the surface areas and emissivities of the bodies.

2.6 Auxillary Components of SC Magnet Systems

$$\dot{Q}_{rad} = F_e \sigma A_1 (T_2^4 - T_1^4) \quad (2.5.0a)$$

Where F_e = emissivity factor between outer vessel (1) and inner body (2).

σ = Stefan-Boltzmann constant = $56.96 \text{ nW/m}^2 \cdot \text{K}^4$

A_1 = surface area of inner body (m^2)

T_1 = absolute temperature of inner body (K)

T_2 = absolute temperature of outer vessel (K)

The general practice of single wall shield design is to use highly conductive materials, like the thermal conduction paths of the coils, so that heat intercepted by the shield is conducted away without significantly raising the temperature of the shield. If the shield temperature increases then more heat will be radiated to the cold body. It is also a good idea to polish the shields so that the emissivity is as low as possible. Leung et al. [90] suggest that good shield materials include polished aluminum, which has an oxide layer that is transparent to radiation below 100 K, and polished copper painted with a thin layer of transparent benzotriazol to prevent oxidation. Gold plating is another option which results in high emissivity surfaces [59].

The other technique of reducing the radiative heat transfer is to place reflective multilayer insulation between the shield and the vacuum vessel inner wall. One of the most common and simplest multilayer insulations is NRC-2 [91], an aluminized mylar sheet. NRC-2 effectively reduces the heat transfer, between 294 K and 77 K, to near 2 W/m^2 , according to Gathright and Reeve [92], when at least 20 layers are used in a high vacuum of less than 10 mPa (7.5×10^{-5} torr) [58]. NRC-2 may also be used between the shield and the 4.2 K

surface but at least 20 layers are necessary. Both Leung et al. [90] and Gathright and Reeve [92] suggest that a simpler and equivalent, or possibly better, technique is to cover all of the radiating surfaces with adhesive 3M aluminized mylar tape [93]. Both authors estimated the heat transfer between 77 K and 4.2 K to be 12.5 mW/m^2 using this technique.

2.6 Auxiliary Components of SC Magnet Systems

Along with the coils, structure, and cooling system, there are four other components of importance; the power supply, current leads, persistent current switch (PCS), and quench protection circuitry.

2.6.1 Power Supply

The power supply must have an output current rating equal to, or greater than, the design current for the coil. Its output voltage, however, may be small (on the order of 5 to 10 volts) because there is little resistance in the charging circuit of the SC magnet and the low ramping rate of the current induces a low voltage drop across the winding. The low ramp rate is needed to prevent quenching from eddy current production within the windings. The power supply voltage must also be very stable to prevent eddy current induced quenching. If the magnet quenches during charging a quench detection and protection system is required to discharge the magnet. The necessary controls include a programmable ramping rate and presettable current and voltage limits. This is an "off the shelf" component and a dialogue with a SC magnet manufacturer will indicate the most suitable power supply for the magnet system [94].

2.6.2 Current Leads

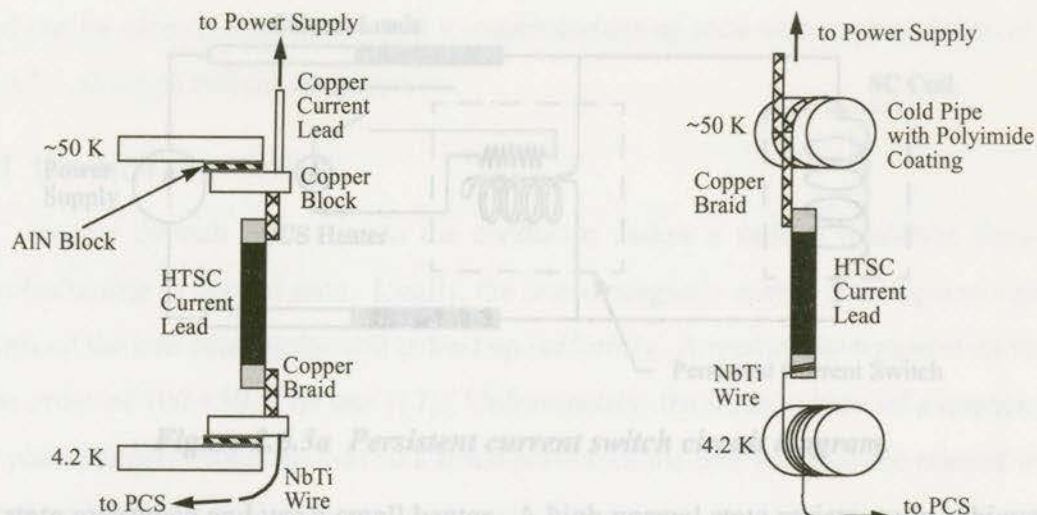
The current leads connect the power supply to the PCS, which is wired in parallel with the coil, but conduct current only during the charging and discharging of the SC coil. The leads introduce heat into the cryostat by conduction and ohmic heating. High conductivity copper leads, which reduce the ohmic heating, connect the power supply to the first stage of the cryocooler. High T_c superconducting (HTSC) leads are used between the first stage and the coil. The copper leads must be designed so that the combination of the ohmic

heating and the thermal conduction loads is minimized. Chafe and Green [95] describe a practical analytic method of finding the optimum length to area ratio of conduction cooled leads that minimizes the heat load to the cryocooler.

The HTSC leads have no ohmic heating losses and the conduction losses are reduced because HTSCs, such as BSCCO and YBCO, are ceramic and have lower thermal conductivities than metals. According to Bock et al. [96], compared to copper, these leads can reduce the heat load to the 4.2 K heat sink by a factor of 10. The copper leads and the wires from the PCS are silver soldered to the ends of the HTSC leads but the ohmic heating at the connections is very small because the contact resistance is on the order of $1 \mu\text{ohm}\cdot\text{cm}^2$ [96][97]. Leads made of HTSC rods and tubes are available commercially and sized according to their current rating.

Because the leads are conductively cooled they must be thermally anchored to the first and second stage of the cryocooler. These connections must be flexible to protect the HTSC leads from mechanical damage as they are very brittle. The thermal anchor must also be thermally conductive as well as electrically insulative to prevent grounding. The HTSC current leads of Takahashi et al.'s [77] conduction cooled magnet system are thermally anchored using blocks of aluminum nitride (AlN), which is electrically insulating but has a thermal conductivity nearly equal to copper. The HTSC rods are soldered to copper braids, the braids are connected to copper blocks, and the copper blocks are screwed into the heat sinks through the AlN blocks. Indium sheets are also placed on the AlN contact surfaces to improve the thermal conduction. Figure 2.6.2a-A shows this assembly arrangement.

Ballarino and Ijspeert [98] also use a relatively simple method for thermally anchoring HTSC current leads. Copper braid is soldered to the warm side of the lead and the braid is wrapped around a cold helium gas tube. 2 layers of 0.025 inch polyimide electrically insulates the braid from the pipe and a stainless steel hose clamp connects the braid to the pipe. The same configuration is used at the cold side of the lead but superconducting NbTi wire is used instead of the copper braid. This arrangement is shown in Figure 2.6.2a-B.



(A) HTSC current lead cooling arrangement of Takahashi et al. [76].

(B) HTSC current lead cooling arrangement of Ballarino and Ijspeert [97].

Figure 2.6.2a Thermal anchoring techniques for HTSC current leads.

2.6.3 Persistent Current Switch

The purpose of the persistent current switch is to place the magnet in a persistent current mode once the charging is complete. In persistent current mode, the power supply may be disconnected while the current continues to flow through the superconducting circuit. The PCS is composed of a low inductance, bifilar winding of superconducting wire and a small heater. The PCS is wired in parallel with the power supply and thermally connected to the 4.2 K heat sink. During charging, the PCS heater is switched on so that the SC wire of the PCS is in the normal state and acts as a resistor. After the coil is fully charged, the PCS heater is switched off so that the SC wire of the PCS becomes superconducting, creating a superconducting circuit with the coil. Once this circuit is complete, the power supply can be turned off. The PCS circuit diagram is shown in Figure 2.6.3a.

The design criteria for a conduction cooled PCS are similar to those of a cryogen cooled PCS but the limited cooling capacity of the cryocooler must also be considered. Dorri and Laskaris [99] claim that a cryogen free PCS should possess two qualities, namely, it should generate as little heat as possible during charging and, after the PCS heater is switched off, it should cool down and revert to the superconducting state in as little time as possible. To reduce the heat generation during charging, the PCS should have a high nor-

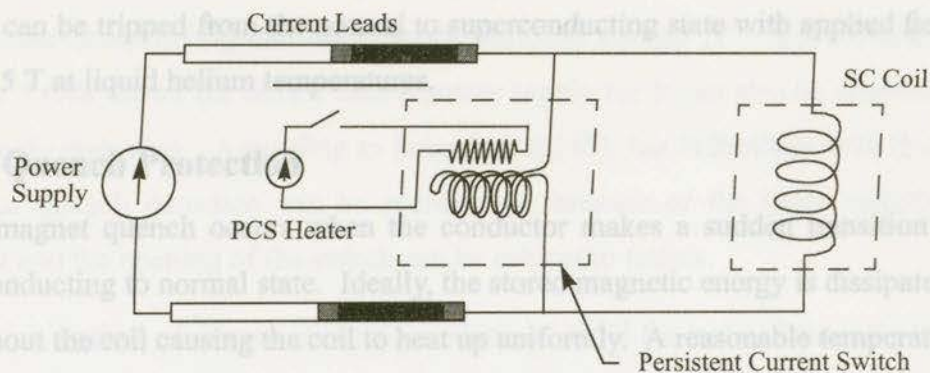


Figure 2.6.3a Persistent current switch circuit diagram.

mal state resistance and use a small heater. A high normal state resistance is achieved by using either long lengths of standard SC wire with a copper stabilizer or shorter lengths of SC wire with a high resistance stabilizer such as CuNi. Using the shorter wire lengths is the more desirable option because the heat capacity of the PCS is reduced and therefore, so is the recovery time. The switch constructed by Dorri and Laskaris met their criteria of producing heat at a rate of less than one watt of heat during charging, allowing the charge to occur in less than two hours, and reverting to the superconducting state, after charging, in less than a half hour.

This switch by Dorri and Laskaris, however, was constructed for a 10 K magnet system using two cryocoolers with a total heat load of 2.1 watts at this temperature [80]. A PCS with a heat load on the order of one watt is unacceptable for a 4.2 K conduction cooled system. Therefore, a heater controlled PCS must be designed to have a very high normal state resistance such that the heat produced is much less than the capacity of the cryocooler. Another method of reducing the heat production is to trip the PCS magnetically rather than thermally. Noto et al. [100] and Sadakata et al. [101] describe a magnetically controlled PCS made of a bifilar winding of NbTi wire with a CuNi stabilizer surrounded by a small SC magnet. When the magnet is turned on, the PCS winding is non-superconducting but it is still cold so the only heat generation is due to ohmic heating from the PCS normal state resistance. When the magnet is turned off, the PCS reverts to the supercon-

ducting state very quickly. The PCS of Sadakata et al. [101] carries currents of 30 to 300 A and can be tripped from the normal to superconducting state with applied fields of less than 0.5 T at liquid helium temperatures.

2.6.4 Quench Protection

A SC magnet quench occurs when the conductor makes a sudden transition from the superconducting to normal state. Ideally, the stored magnetic energy is dissipated equally throughout the coil causing the coil to heat up uniformly. A reasonable temperature rise is on the order of 100-150 K or less [17]. Unfortunately, the initialization of a quench is a local phenomenon within the coil so a small portion of the coil will become normal while the rest of the coil remains superconducting. The rate at which a coil quenches can be gauged by the normal zone propagation (NZP) velocity of the coil conductor. If the NZP velocity is not high enough, failure may occur from local overheating, arcing due to large inductive voltages, or thermally induced overstressing [47]. The limit of the normal zone heating is 300-400 K [17]. Anything more than this may cause insulation damage or local over stressing. Magnets with NZP velocities high enough to prevent failure are aptly labelled "self-protecting". Magnet systems that are not self-protecting require quench protection circuitry.

The most basic method of active quench protection is the detect-and-dump technique. Figure 2.6.4a shows the simplified circuit diagram for this technique. When a quench is

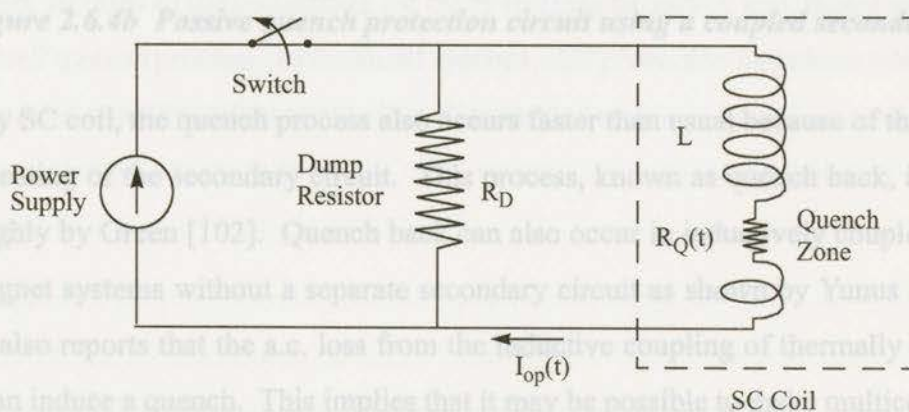


Figure 2.6.4a The basic detect-and-dump active quench protection circuit.

detected within the coil the switch is opened so the energy stored in the coil can be dis-

charged into an external resistor [17][47]. The choice of dump resistors controls the rate of current decay (di/dt) and therefore the induced voltage ($V = Ldi/dt$) across the coil. Figure 2.6.4a shows the circuit with a power supply but it can also be adapted for persistent mode operation. According to Iwasa's text [47], the difficulties with this technique are that quench detection can be problematic because of the large inductive voltage present and the opening of the switch can be subject to failure.

A passive method of quench protection, which is useful for isolated magnets in persistent mode, is the use of a coupled secondary coil. If the primary SC coil should quench, some of the energy from the primary coil will be transferred to the secondary coil, due to the mutual inductance of the two coils, reducing the maximum temperature and voltage in the primary coil [17]. The circuit diagram of a coupled secondary protection system is displayed in Figure 2.6.4b. When the secondary resistive coil is in thermal contact with the

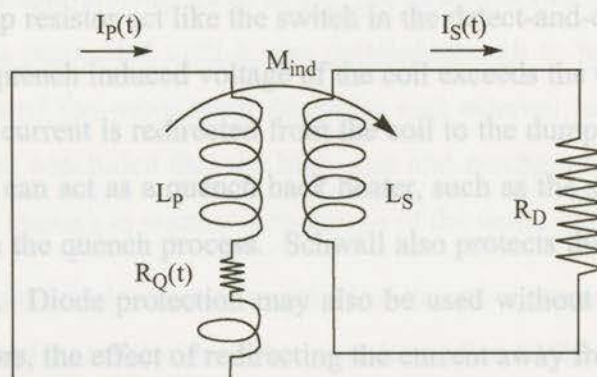


Figure 2.6.4b Passive quench protection circuit using a coupled secondary coil.

primary SC coil, the quench process also occurs faster than usual because of the additional joule heating of the secondary circuit. This process, known as quench back, is examined thoroughly by Green [102]. Quench back can also occur in inductively coupled multicoil SC magnet systems without a separate secondary circuit as shown by Yunus et al. [103]. Yunus also reports that the a.c. loss from the inductive coupling of thermally isolated SC coils can induce a quench. This implies that it may be possible to make multicoil SC magnets self-protecting without the reliance of heaters for encouraging the quench process.

Another method of passive quench protection is the use of high power silicon diodes as shown by the multicoil diode protection circuit of Figure 2.6.4c. Diodes wired parallel to

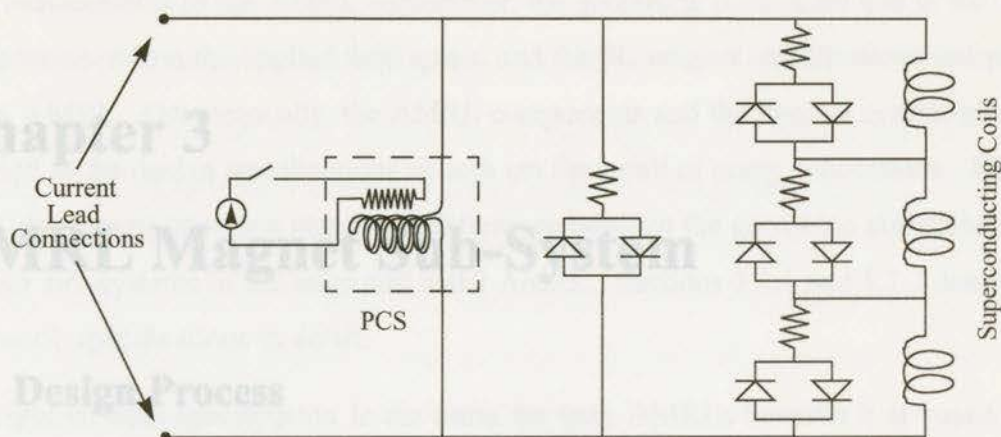


Figure 2.6.4c Passive quench protection circuit using high power diodes.

the SC coil with a dump resistor act like the switch in the detect-and-dump circuit of Figure 2.6.4a. When the quench induced voltage of the coil exceeds the threshold voltage of the diode, some of the current is redirected from the coil to the dump resistor. Additionally, the dump resistor can act as a quench back heater, such as the system examined by Schwall [104], to force the quench process. Schwall also protects the PCS from burnout using diode protection. Diode protection may also be used without dump resistors. In systems without resistors, the effect of redirecting the current away from the quench zone into other sections of the coil causes the other sections to quench and, therefore, speeds up the overall quench process. In multicoil systems, this protection technique combined with the inductive coupling effect results in well protected coils.

The magnet designs in this thesis were carried out sequentially; for the sake of clarity, however, they are presented in parallel. They differ in their configurations, because each has distinct constraints and specifications, but some similarities and general concepts do exist. The differences, similarities, and general concepts of these systems are presented for each stage of the design procedure.

3.2 Specifications and Constraints

The specifications that define the SC magnet sub-system are a combination of the applied field requirements of the AMRL regenerator, the geometric constraints due to the AMRL components within the applied field space, and the SC magnet specifications independent

Chapter 3

AMRL Magnet Sub-System

3.1 Design Process

Initially, the AMRL project called for the construction of a prototype rotary AMRL capable of 1 kW of refrigeration between 240 K and 110 K. This cooling capacity equals an LNG production rate of approximately 200 l/day. The design of this device, including the SC magnet sub-system, proceeded until it was detailed enough to hold a critical design review in the presence of the sub-system designers and external technical consultants. After the review, it was concluded that the high cost and mechanical complexity of the design were significant enough to warrant a re-design of the entire system.

The new design was downsized in capacity and all of the sub-systems were decoupled as much as possible to simplify the design. The second, smaller AMRL is made to provide 500 W of refrigeration power and is considered more robust than its predecessor. Re-designing the AMRL also required a new design for the SC magnet sub-system. Although the first magnet design was never fully completed, the gained knowledge was applied to the second design, which is presently under construction, and can be applied to all subsequent magnet systems for rotary MR devices.

The magnet designs in this thesis were carried out sequentially; for the sake of clarity, however, they are presented in parallel. They differ in their configurations, because each has distinct constraints and specifications, but some similarities and general concepts do exist. The differences, similarities, and general concepts of these systems are presented for each stage of the design procedure.

3.2 Specifications and Constraints

The specifications that define the SC magnet sub-system are a combination of the applied field requirements of the AMRL regenerator, the geometric constraints due to the AMRL components within the applied field space, and the SC magnet specifications independent of the AMRL. Geometrically, the AMRL components and the magnet system are highly coupled so the design specifications of both are the result of many concessions. This coupling also means there is a significant difference between the geometric constraints of the magnet sub-systems of the large and small AMRL. Sections 3.2.1 and 3.2.2 describe the geometric specifications in detail.

The applied field specification is the same for both AMRLs because it is based on the magneto-thermodynamics of the refrigerant material in the regenerator matrix. A uniform, minimum mean applied magnetic field of 7 T is desired in the entire high-field region of the AMR ring while the applied field in the no-field region should be as low as possible. It was not possible to meet this field requirement in the large AMRL design but it was possible for the second, small AMRL.

Initially, it was unknown if a non-uniform applied field would adversely affect the performance of an AMRL so an azimuthal field homogeneity on the order of 5% was specified for the large AMRL. This value was chosen because it was thought to be small enough not to significantly affect the thermodynamic performance of the device but also not so small that it would significantly increase the cost of the magnet. Later, it was determined by Spearing [15] that azimuthal field fluctuations of this magnitude would affect adversely affect the performance of the AMRL. Therefore, the homogeneity requirement of the small AMRL was specified to be as small as possible and less than 5% without significantly increasing the cost of the SC coils.

The other requirements of the magnet sub-system design, which are independent of the AMRL specifications, are the conduction cooling system and, if possible, the use of NbTi conductors rather than Nb₃Sn conductors. Although Nb₃Sn magnets can provide a greater applied field than NbTi magnets, they are also more expensive to produce. The conduction cooling of the coils is to be accomplished with a single 4.2 K G-M cryocooler. The

cryocooler is modified from a standard G-M refrigerator to supply 0.5 W of cooling capacity at 4.2 K. Therefore, the total heat load to the 4.2 K stage of the system must be kept below 0.5 W.

3.2.1 Large AMRL Geometric Specifications

Figure 3.2.1a shows the basic dimensions of the large AMRL regenerator and pressure housing. The regenerator is a particle bed of magnetic refrigerant materials with a porosity of 38%. It has a 5.5 cm by 5 cm cross section, a mean diameter of 60 cm, and is enclosed within a pressure housing that has a diameter of approximately 10 cm. The pressure housing dimension is approximate because at the time the specifications were made the exact value was unknown. The housing contains the helium working gas at 5 MPa so it must have a large enough wall thickness, which affects the diameter, to meet the necessary strength requirements. Conversely, the housing needs to remain as small as possible so the SC coils can be placed as close as possible to the AMR ring. A 120° section of the AMR ring is to be magnetized with a uniform magnetic field and no components of the SC magnet sub-system are to be located more than 15° of either side of the 120° magnetized section. This leaves only a 150° construction zone for the magnet sub-system. This 150° construction zone was later considered too restrictive so it was specified to be as small as possible and varied during the design of the magnet system.

As stated earlier, the AMRL and SC magnet geometric specifications are highly coupled. The pressure housing is given a circular shape because it can have a thinner wall thickness than a non-circular shape for a given internal pressure. The size of the magnetized region is then determined by cooling power, or the liquefaction rate, of the AMRL. For a fixed rotation frequency, a specific volume of magnetized material is necessary to meet the cooling requirements of the liquefier. If the AMR ring were made larger, the magnetization region would enclose a smaller arc for the same material volume. The cost of the magnetic refrigerants is relatively high so it is important to reduce the AMR ring size as much as possible. Early in the AMRL project it was decided that a 120° arc was the maximum magnetization zone that could be covered considering the need for an equivalent sized no-field region on the other side of the ring and an intermediary region where the field changes.

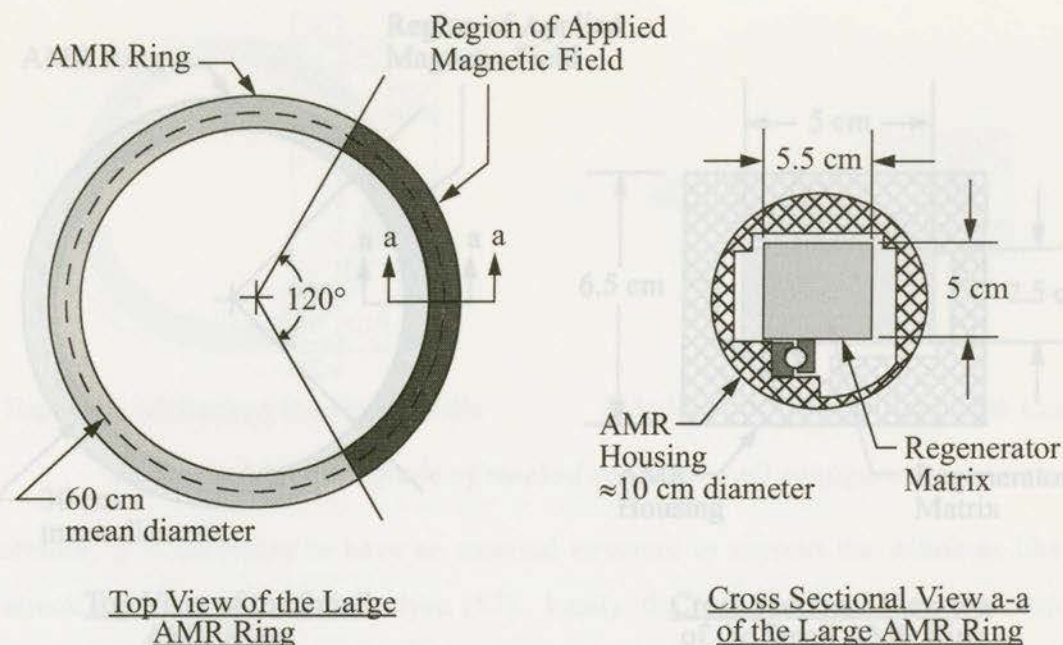


Figure 3.2.1a Schematic of the large AMRL geometry.

3.2.2 Small AMRL Geometric Specifications

Like the large AMR ring, the small ring is a particle bed with a porosity of 38% but has a 5 cm by 2.5 cm cross section and a mean diameter of 30 cm. The general layout of the small AMR is shown in Figure 3.2.2a. The 7 MPa operating pressure of the helium gas is higher than for the large AMRL so the housing is proportionately larger, however, the regenerator height was reduced to 2.5 cm so the pressure housing height is only 6.5 cm.

The magnetization zone was initially specified to span an arc of 120° but this was later considered too large for the selected coil configuration. A circular magnet that could provide a field over a 120° arc is prohibitively large and expensive. The region of constant magnetization was, therefore, set at 90° . Similarly, the no-field region is the equivalent size on the opposite side of the wheel. The greatest difference between the first and second AMRL design is that the smaller second AMRL was specified to have a one piece AMR ring, bearing race, and gear track. This means that the AMR ring, pressure housing, and associated components must be completely decoupled from the SC magnet sub-system in terms of construction. Therefore, the SC coil choices for this system are limited to the split pair and racetrack configurations.

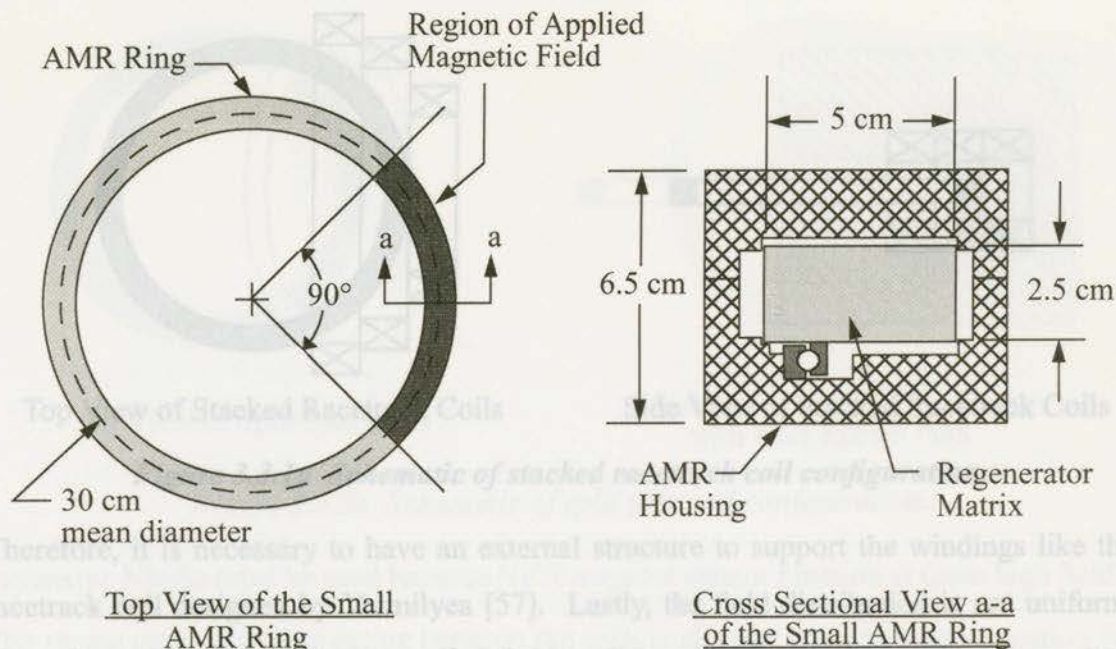


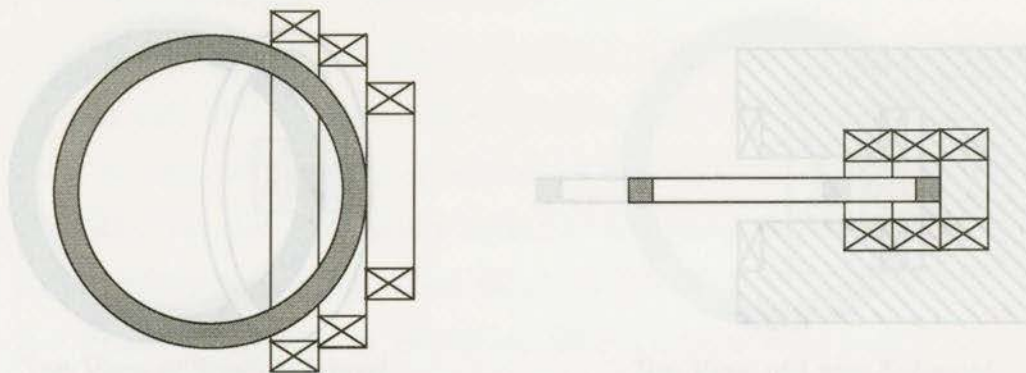
Figure 3.2.2a Schematic of small AMRL geometry.

3.3 Evaluation of Coil Configurations

Each of the possible coil configurations, shown in Figure 2.2.1a, has certain positive and negative attributes. The attributes presented here were evaluated as part of this thesis and the most suitable coil configuration for given AMRL specifications was selected.

3.3.1 Racetrack Configuration

The greatest advantage of the racetrack coil configuration is that it allows the AMR ring and the SC magnet subsystem to have a mechanically decoupled design. The magnetized volume of the coil is also well utilized by the ring so there is little wasted magnetized volume. Unfortunately, a single racetrack coil does not cover a large region of the AMR ring. It is necessary to use two or more coils stacked in the "football stadium" shape, like the system by Barclay and Steyert [44], as shown in Figure 3.3.1a. This winding shape is also difficult to wind because of the long straight sections of conductor. Often, these types of coils are shaped to have a slightly positive curvature, rather than flat sections, so that winding tension may be maintained. The long flat sections of these coils are also subject to large Lorentz forces but do not have the internal strength to withstand these forces.



Top View of Stacked Racetrack Coils

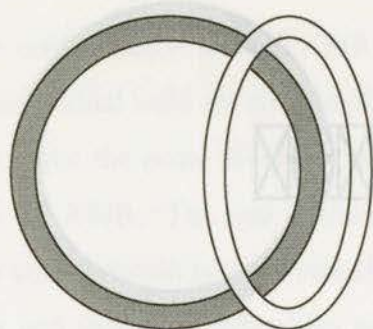
Side View of Stacked Racetrack Coils

Figure 3.3.1a Schematic of stacked racetrack coil configuration.

Therefore, it is necessary to have an external structure to support the windings like the racetrack coil designed by Vermilyea [57]. Lastly, the field distribution is not uniform. Near the ends of the coils the applied field is disproportionately larger than the central field so quenching can occur when the central field is relatively low, such as the racetrack coil by Barclay and Steyert [44].

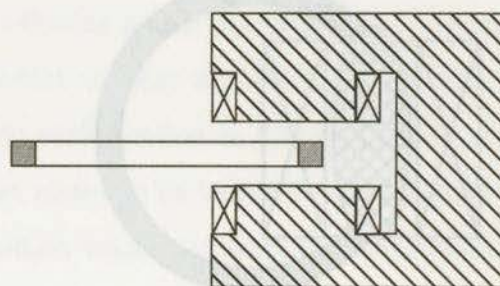
3.3.2 Split Pair Configuration

Like the racetrack configuration, the greatest advantage of the split pair configuration is that it is decoupled from the AMR ring. The direction of the applied field is also perpendicular to the AMR ring so there is less stray field in the no-field region of the AMR than would be found with a racetrack coil. However, circular coils must be very large to magnetize a large portion of the AMR ring. By using elliptical shaped coils, as shown in Figure 3.3.2a, smaller windings can be made to magnetize a large portion of the AMR. Elliptical coils are not as difficult to build as racetrack coils but must still be custom manufactured at a high cost because of their odd shape. The biggest drawback with this configuration is that the AMR ring does not effectively utilize the magnetized space of the coils as suggested by Barclay et al. [45]. This effect can be minimized by reducing the gap between the coils as much as possible and using a flux return path. Even so, the magnitude of the useful field between the coils may be on the order of half of the maximum field in the windings. Therefore, if a useful field on the order of 7 T is required for the AMR ring, the coils must tolerate upwards of 12-14 T within the windings. Therefore,



Top View of Small Solenoid

Top View of Split Pair Coils



Top View of Large Solenoid

Side View of Split Pair Coils
with Flux Return Path

Figure 3.3.2a Schematic of split pair coil configuration.

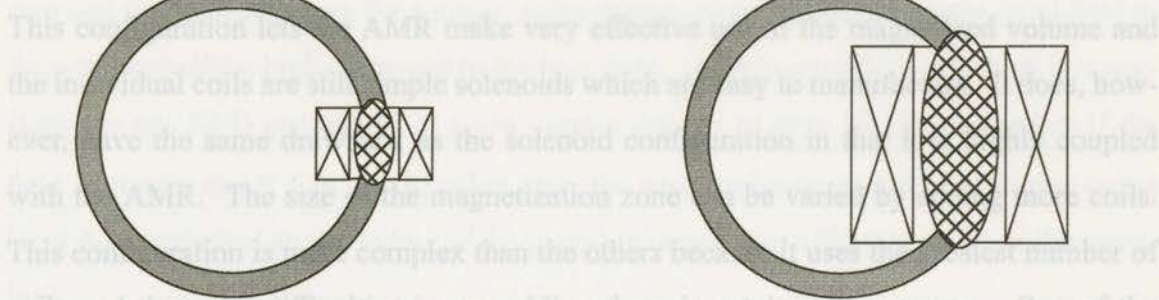
increased but the AMR ring was progressively less of the total magnetized volume. One expensive Nb_3Sn must be used because NbTi magnets cannot function at these high fields. The strong attractive force acting between the coils is also an important consideration for this configuration. The structure separating the coils must be suitably strong and rigid yet not impede the access of the AMR ring to the magnetization zone. With the materials such as 9% nickel steel, which is ferromagnetic and has a high strength at cryogenic temperatures, it is possible to additionally employ the coil separation structure as a flux return path.

3.3.3 Solenoid Configuration

The solenoid configuration, shown in Figure 3.3.3a, is very desirable because the coil is the most simple and inexpensive of all of the possible configurations. The inherent problem with this configuration is that the AMR ring, and its associated components, must be constructed in at least two pieces for assembly. Although not impossible, it is a challenging problem to construct split components of rotating machinery with the associated pressure housing.

The other difficulty with this design is that a single coil cannot provide a large zone of magnetization without having a large inner diameter, as shown in Figure 3.3.3a. Because of the curvature of the AMR ring a small diameter solenoid can only magnetize a small arc of the ring. A larger arc of the ring will be magnetized as the solenoid diameter is

3.3.4 Partial Tokamak Configuration



Top View of Small Solenoid
with Associated Magnetization Zone

Top View of Large Solenoid
with Associated Magnetization Zone

Figure 3.3.3a Comparison of magnetization zones for solenoid coil configuration.

increased but the AMR ring uses progressively less of the total magnetized volume. One way to magnetize a large arc of the AMR wheel without wasting much of the magnetized volume is to assemble many small coils in the partial tokamak configuration.

Perhaps the most effective way to use a solenoid coil for a rotary magnetic refrigeration system is to arrange the AMR in the form of a flexible belt or chain as proposed by Barclay et al. [42]. This “chainsaw” configuration, shown in Figure 3.3.3b also uses a single solenoid but has two thermodynamic cycles per complete rotation of the chain. This design, however, was not chosen by the Cryofuel Systems group. It was considered risky to manufacture, primarily due to the mechanical complexity of the flexible AMR.

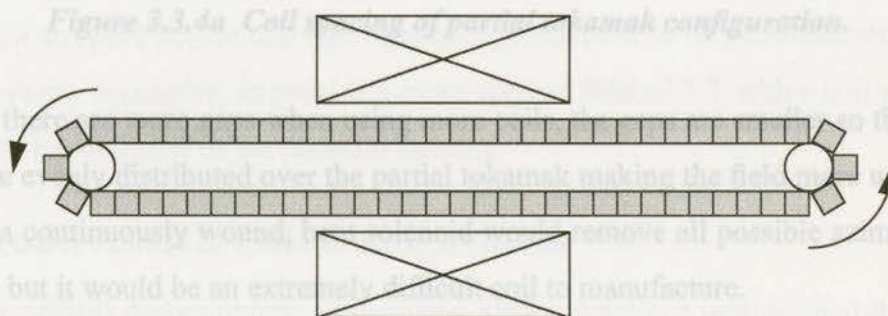


Figure 3.3.3b Schematic of “chainsaw” AMR and solenoid coil configuration.

3.3.4 Partial Tokamak Configuration

This configuration lets the AMR make very effective use of the magnetized volume and the individual coils are still simple solenoids which are easy to manufacture. It does, however, have the same drawback as the solenoid configuration in that it is highly coupled with the AMR. The size of the magnetization zone can be varied by adding more coils. This configuration is more complex than the others because it uses the greatest number of coils and there are difficulties in assembling them in a tokamak geometry. One of the more important concerns is the azimuthal field attenuation between the coils caused by the absence of winding in the gap between the coils. This azimuthal field ripple effect can be reduced by using more coils within the same arc length, as shown in Figure 3.3.4a.

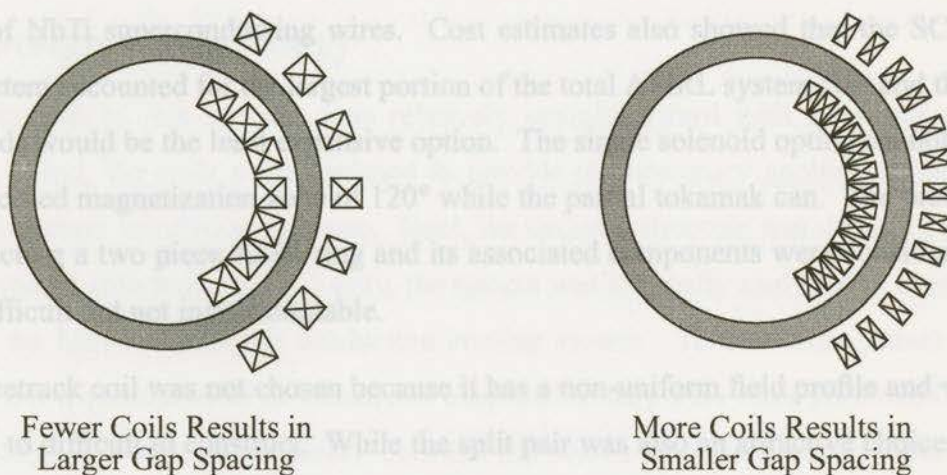


Figure 3.3.4a Coil spacing of partial tokamak configuration.

Although there are more gaps when using more coils, the gaps are smaller so the conductor is more evenly distributed over the partial tokamak making the field more uniform. In the limit, a continuously wound, bent solenoid would remove all possible azimuthal field variations but it would be an extremely difficult coil to manufacture.

The other concern with a toroidal or tokamak type winding is the radial field attenuation. The magnetic field intensity across the width of the AMR ring, within the bore of the partial tokamak, decreases from the inner to outer radius as a function of $1/r$. Because it is a function of $1/r$, this radial field attenuation effect lessens as the overall radius of the AMR ring and the associated coil assembly increases. The radial field attenuation is a problem

because the high field gradient that exists across the ring induces large forces between the ring and the magnet. Also, for a small radius partial tokamak, the maximum local field in the winding will be high compared to the bore field. If the local field is very high it is necessary to use NbTi conductors at a low current density or even Nb₃Sn conductors if the field is greater than 9 T or so. In either case, the winding becomes more expensive as the local field increases so the radius of the partial tokamak also affects the cost of the windings.

3.4 First AMRL Coil Configuration

The partial tokamak coil configuration was selected for the first, large AMRL design because it is able to economically provide a large magnetization zone with solenoid coils made of NbTi superconducting wires. Cost estimates also showed that the SC magnet sub-system accounted for the largest portion of the total AMRL system cost and that NbTi solenoids would be the least expensive option. The single solenoid option cannot provide the specified magnetization zone of 120° while the partial tokamak can. The problems of constructing a two piece AMR ring and its associated components were considered to be very difficult but not insurmountable.

The racetrack coil was not chosen because it has a non-uniform field profile and was considered to difficult to construct. While the split pair was also an attractive choice because of its decoupled design, the magnetic field attenuation between the coils was considered too great for an AMR ring of this size. The coils would have to be unreasonably large, and correspondingly expensive, to provide a mean applied field of 7 T with a coil gap greater than 10 cm, the diameter of the pressure housing.

3.5 Second AMRL Coil Configuration

During the critical design review of the large AMRL system it was decided that the two piece AMR ring and the pressure housing was too expensive and risky to merit construction. Theoretically the design worked but the manufacturing tolerances were very high and considered unattainable for the available manufacturing resources. Therefore, a new

AMRL design that allowed the magnet sub-system and the AMR ring to be physically decoupled was required. This meant that the racetrack and split pair coil configurations were the only possible design options.

Of these two choices, the split pair configuration was selected because it provided a uniform field distribution and produced a low field in the no-field region of the AMR ring. It did, however, have to be designed to use Nb₃Sn conductors in order to provide a mean central field over 7 T. Because Nb₃Sn coils are quite expensive to construct, the AMR ring diameter, AMR height, and the size of the magnetization zone were all reduced so that the overall coil size and, therefore, cost was reduced. So, unlike the first AMRL design, the magnet specifications of the second AMRL drove the AMR ring specifications.

3.6 Design Methodology

The approach to this problem was relatively straightforward with three major design phases. First, the coils were designed to provide the necessary applied magnetic field using computer simulation software. Next, the external structure was designed based on the estimated structural loads. Lastly, the system was thermally analyzed to estimate and reduce the heat loads on the conduction cooling system. These design phases are presented in a sequential order in subsequent chapters but they were often performed in parallel because of the interdependency between the results from each phase. Before each phase, the necessary design information such as the magnetic, mechanical, and thermal material properties were found or estimated if they were unknown.

The coils were modeled as bulk conductors rather than identify each individual wire. Without this simplification the simulation models become too large to solve. The bulk current density of the coils was calculated from the wire operating current, diameter, and packing factor. The coils were modeled with the maximum possible bulk current density, without exceeding the wire specifications, so that the conductor volume was minimized.

Symmetrical designs were cut along the symmetry plane and only one half of the design was modeled which reduced the computation time. If the symmetry plane was tangential to the applied field direction then the plane was defined with a Neumann boundary condition. The Neumann boundary condition forces the field solution to be tangential to the

Chapter 4

Magnetic Field Modelling and Coil Design

4.1 Magnetic Field Modeler

The SC coils for the AMRL project were designed using the Maxwell 3D Field Simulator™ software by Ansoft [105] operating on a Sun [106] Sparc 10 workstation. The simulator is capable of solving three dimensional magnetostatic problems with non-linear material properties. Although the liquefier is dynamic because the AMR ring actually rotates through the magnetic field during operation, it was modelled as a static problem because the rotation of the circular and continuous magnetic ring does not significantly modify the applied field profile.

A three dimensional solid model was constructed within the simulator via a CAD interface. Conductors were then identified and assigned current densities. Non-conductors were assigned magnetization values as a function of applied field. It was necessary to model the coils as bulk conductors rather than identify each individual wire. Without this simplification the simulation models become too large to solve. The bulk current density of the coils was calculated from the wire operating current, diameter, and packing factor. The coils were modelled with the maximum possible bulk current density, without exceeding the wire specifications, so that the conductor volume was minimized.

Symmetrical designs were cut along the symmetry plane and only one half of the design was modelled which reduced the computation time. If the symmetry plane was tangential to the applied field direction then the plane was defined with a Neumann boundary condition. The Neumann boundary condition forces the field solution to be tangential to the

plane. If the symmetry plane is perpendicular to the field a Dirichlet boundary condition is applied. The Dirichlet boundary condition forces the field solution to be perpendicular to the plane. A Neumann boundary condition was applied to all other planes of the solution boundary.

Next, a finite element mesh was created for the solid model by the software and the magnetic field was computed by finite element analysis. The analysis uses Ampere's law, Equation (4.1.0a), and Maxwell's equation describing the continuity of flux, Equation (4.1.0b).

$$\nabla \times \underline{H} = \underline{J} \quad (4.1.0a)$$

$$\nabla \cdot \underline{B} = 0 \quad (4.1.0b)$$

Additionally, the magnetic flux density, \underline{B} , was found with Equation (4.1.0c) where μ_0 is the permeability of free space and \underline{M} is the magnetization of the material.

$$\underline{B} = \mu_0 (\underline{H} + \underline{M}) \quad (4.1.0c)$$

After the magnetic field was calculated, the solution was used to estimate the residual error of the energy in each finite element. The sum of this error is the total 'energy error' and it represents the accuracy of the solution. The simulator uses adaptive meshing to generate more accurate solutions with each successive iteration. Solutions with an energy error less than 5% were considered to have converged for initial design purposes because better convergence required more computation time. More accurate solutions with an energy error less than 2% were used for final designs. These convergence values were based on benchmark solutions of a basic solenoid and are also suggested by the software company. The accuracy of the benchmark field solution was within 5% which was considered acceptable for design purposes.

4.2 Design Information

The two necessary pieces of information for the magnetic field analysis and coil design were the conductor current densities and the material magnetization curves. The operating currents of commercially available superconducting wires provided estimates of typical bulk current densities. The necessary magnetization curves came from the material properties data of the magnetic refrigerants in the AMR ring and the material used for the flux return path.

4.2.1 SC Wire Critical Current

All commercially available SC wires are tested at 4.2 K over a range of applied fields for their critical currents. Although they are only tested at 4.2 K, the critical currents at other temperatures were estimated, using Equation (2.3.0a) and Equation (2.3.0b), and used to evaluate the sensitivity of the designed field with temperature. These short sample tests take place with little or no wire strain so realistic operating currents are usually estimated to be 80-90% of the short sample critical currents. The bulk current density of the coils is around 45-65% of the wire current density. This scaling factor is based on the wire's packing factor due to its circular cross section, insulation, and winding pattern.

The operating currents, and associated bulk current densities, for typical multifilament NbTi wires is shown in Table 4.2.1a. The values presented are for 54S43 wire available from Supercon, Inc [107]. The values at 4.2 K come directly from Supercon while the values at 4.5 K and 5 K were estimated using Equation (2.3.0a) and Equation (2.3.0b). These values were based on packing factors of 65%, 60%, and 55% for the large, medium, and small diameter wires respectively and correspond with the typical realistic working current densities of established magnet systems [108]. The packing factors are lower for smaller diameter wire because the wire insulation, which has a constant thickness for all wires, accounts for a relatively greater portion of the wire's cross sectional area. As is

shown, the bulk current density, which was used for modelling purposes, is not strongly related to the wire diameter. Therefore, during the initial design phase it was unnecessary to exactly specify the wire diameter and current.

Table 4.2.1a: Typical operating currents for NbTi filamentary wire.

Wire Diameter (mm) and Packing Factor	Applied Field = 9 T		Applied Field = 7 T	
	Operating Current (A)	Bulk Current Density (A/cm ²)	Operating Current (A)	Bulk Current Density (A/cm ²)
At 4.2 K				
1.016 (P.F. = 65%)	180	14432	500	40088
0.762 (P.F. = 60%)	105	13815	310	40787
0.508 (P.F. = 55%)	45	12212	140	37991
At 4.5 K				
1.016 (P.F. = 65%)	126	10109	427	34201
0.762 (P.F. = 60%)	74	9677	264	34797
0.508 (P.F. = 55%)	32	8554	119	32412
At 5.0 K				
1.016 (P.F. = 65%)	36	2905	304	24388
0.762 (P.F. = 60%)	21	2781	189	24813
0.508 (P.F. = 55%)	9	2458	85	23113

Table 4.2.1a shows the operating currents for Nb₃Sn multifilament wires supplied by Tele-dyne Wah Chang [109]. The operating currents are 85% of the tested short sample critical currents. Like the previous data for NbTi wires, the bulk current density is nearly independent of the wire diameter so it was unnecessary to specify the exact wire diameter and current during the initial design phase.

As the B-H curves show, the relative permeability of Gd and Dy is around 1.5 below applied fields of 1 T and steadily decreases to unity as the magnitude of the applied field increases. The data for these curves were obtained from a using a molecular field model to simulate ferromagnetic materials properties. This simulation provided the magnetic

Table 4.2.1b: Typical operating currents for Nb₃Sn filamentary wire.

Wire Diameter (mm) and Packing Factor	Applied Field = 14 T		Applied Field = 12 T	
	Operating Current (A)	Bulk Current Density (A/cm ²)	Operating Current (A)	Bulk Current Density (A/cm ²)
At 4.2 K				
1.263 (P.F. = 60%)	503	24090	750	35919
0.600 (P.F. = 55%)	122	23732	187	36377
At 5.0 K				
1.263 (P.F. = 60%)	308	14758	579	30030
0.600 (P.F. = 55%)	75	14539	144	28073
At 6.0 K				
1.263 (P.F. = 60%)	65	3093	365	17471
0.600 (P.F. = 55%)	16	3047	91	17693

4.2.2 Material Magnetization Properties

The magnetic refrigerant material within the AMR ring is a blend of pure and alloyed rare earth metals which include gadolinium, dysprosium, and holmium [110]. The magnetization curve of Gd, shown in Figure 1.1.3c, is indicative of the magnetization curves of these refrigerants. Although all of the refrigerants have differing temperature dependencies upon their magnetization, they all also operate at different temperatures because of the thermal gradient within the AMR ring. The result is that all of the materials operate near their respective Curie temperatures so they all have very similar magnetic properties during operation. This similarity is shown by the B-H curves, in Figure 4.2.2a and Figure 4.2.2b, of Gd and Dy near their respective Curie temperatures of 293 K and 179 K.

As the B-H curves show, the relative permeability of Gd and Dy is around 1.5 below applied fields of 1 T and steadily decreases to unity as the magnitude of the applied field increases. The data for these curves were obtained from a using a molecular field model to simulate ferromagnetic materials properties. This simulation provided the magnetic

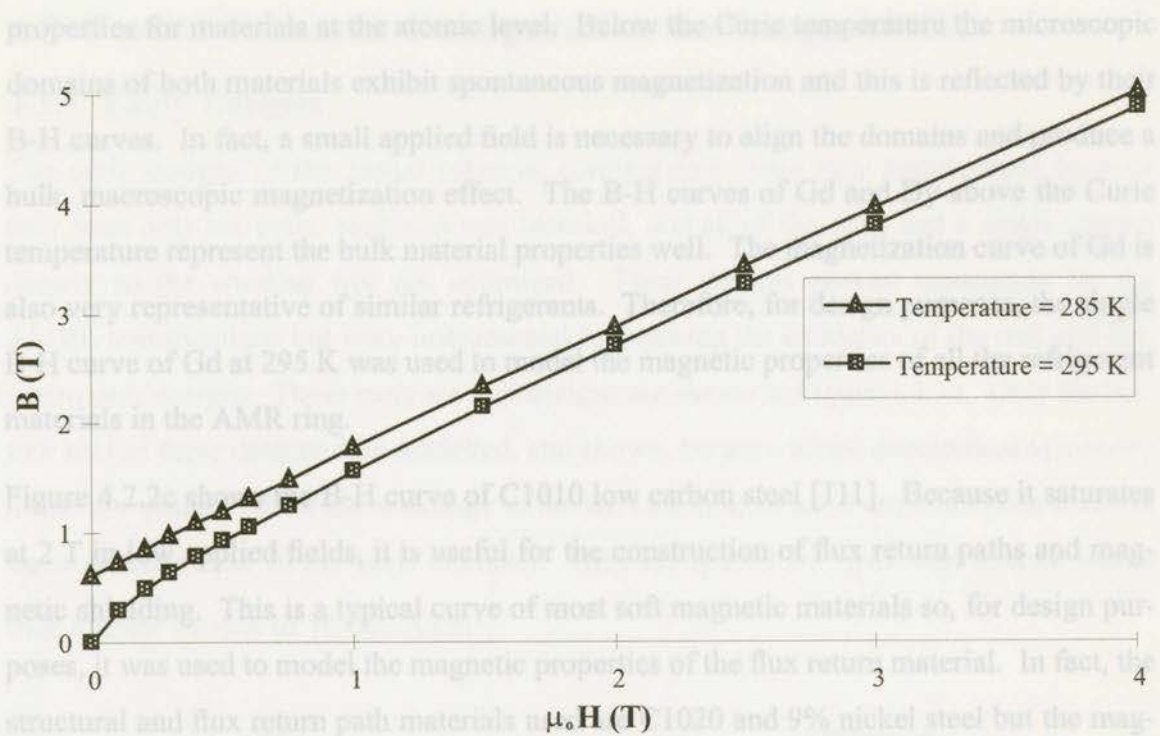


Figure 4.2.2a Graph of B vs. $\mu_0 H$ for Gadolinium near its Curie temperature of 293 K.

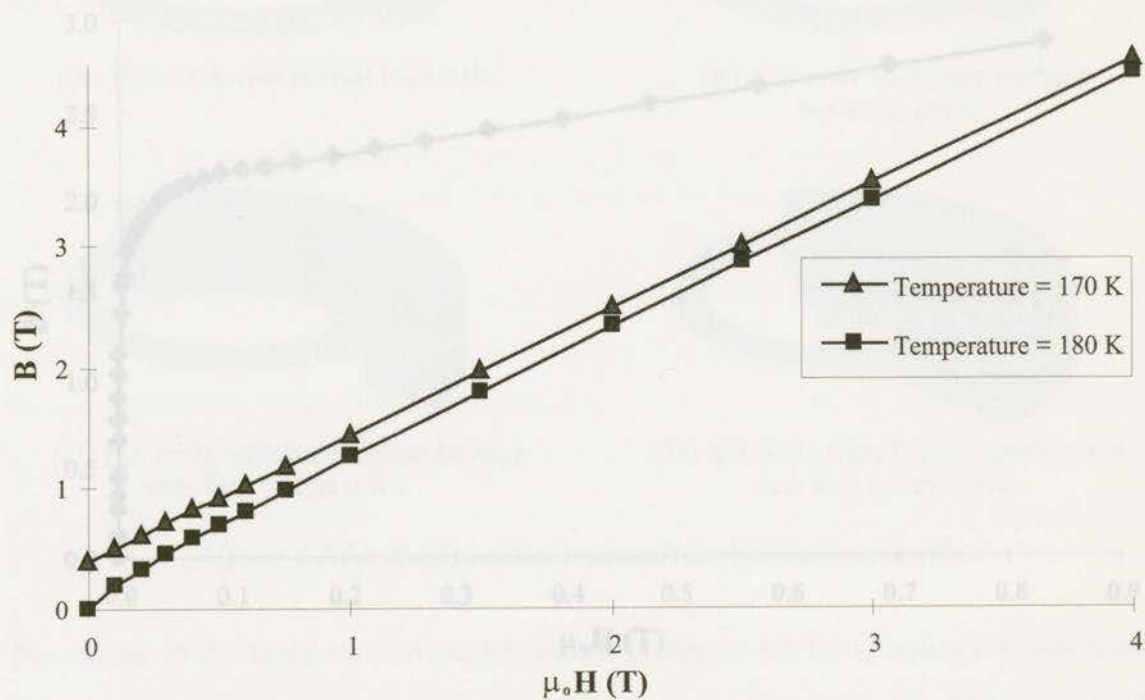


Figure 4.2.2b Graph of B vs. $\mu_0 H$ for Dysprosium near its Curie temperature of 179 K.

properties for materials at the atomic level. Below the Curie temperature the microscopic domains of both materials exhibit spontaneous magnetization and this is reflected by their B-H curves. In fact, a small applied field is necessary to align the domains and produce a bulk, macroscopic magnetization effect. The B-H curves of Gd and Dy above the Curie temperature represent the bulk material properties well. The magnetization curve of Gd is also very representative of similar refrigerants. Therefore, for design purposes, the single B-H curve of Gd at 295 K was used to model the magnetic properties of all the refrigerant materials in the AMR ring.

Figure 4.2.2c shows the B-H curve of C1010 low carbon steel [111]. Because it saturates at 2 T in low applied fields, it is useful for the construction of flux return paths and magnetic shielding. This is a typical curve of most soft magnetic materials so, for design purposes, it was used to model the magnetic properties of the flux return material. In fact, the structural and flux return path materials used are C1020 and 9% nickel steel but the magnetization curves for these materials were unavailable.

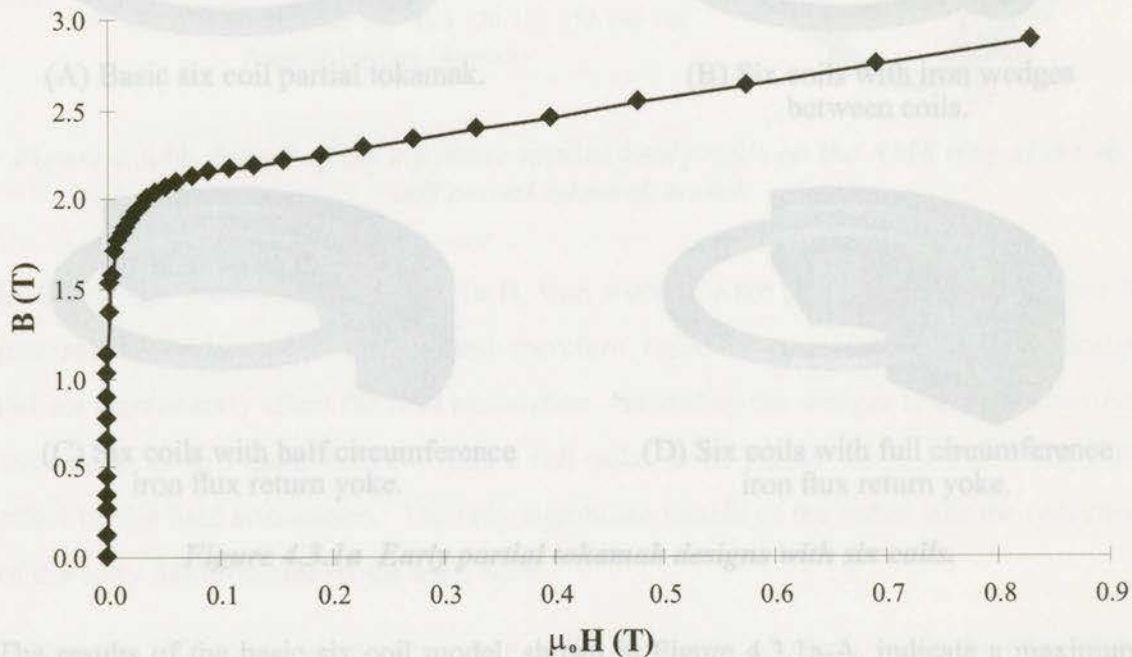
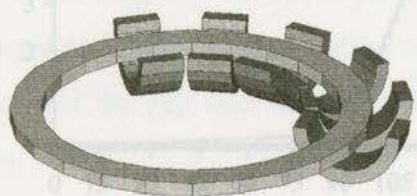


Figure 4.2.2c Graph of B vs. $\mu_0 H$ for C1010 low carbon steel.

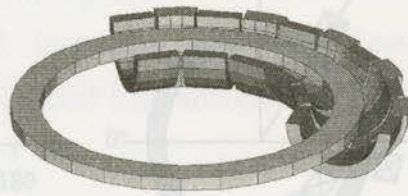
4.3 Partial Tokamak Configuration for Large AMRL

4.3.1 Early Designs

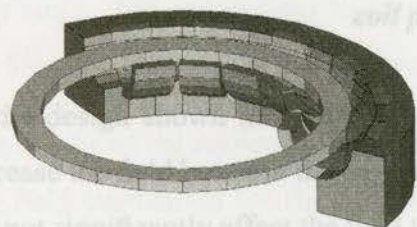
The early designs of the partial tokamak configuration were very approximate because they used only six coils, each coil was identical, and all of the coils had a single current density so the winding was not optimized. These designs proved inadequate for the AMRL specifications but were instrumental in exposing the subtleties of the coil and flux return path designs. These early six coil designs are shown in Figure 4.3.1a. Only the bottom half of these designs was modelled, and shown, because of the geometrical symmetry in the x-y plane. All of the windings in the six coil models are 8 cm wide with a 15 cm inner diameter and 20 cm outer diameter. They are spaced 24° apart and operate with a bulk current density of $30,000 \text{ A/cm}^2$.



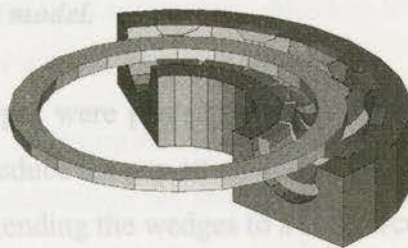
(A) Basic six coil partial tokamak.



(B) Six coils with iron wedges between coils.



(C) Six coils with half circumference iron flux return yoke.



(D) Six coils with full circumference iron flux return yoke.

Figure 4.3.1a Early partial tokamak designs with six coils.

The results of the basic six coil model, shown in Figure 4.3.1a-A, indicate a maximum field of 7.2 T in the windings which is acceptable for a current density of $30,000 \text{ A/cm}^2$. Unfortunately, there is a strong radial field attenuation shown by a maximum field at the inner circumference of the AMR of 6.5 T and 5.5 T at the outer circumference. The azi-

muthal attenuation is also approximately 0.75 T from the central bore of the tokamak to the bore of the end coils. Lastly, the mean field attenuation from the bore of any coil to the gap position between the coils is also approximately 0.75 T. The sketch of the applied field profile in Figure 4.3.1b shows the radial, azimuthal, and gap attenuation. Attempts to reduce these three forms of field attenuation were made in the subsequent models shown in Figure 4.3.1a-B, C, and D. These models used the selective placement of iron yokes to try to reduce the different field attenuations.

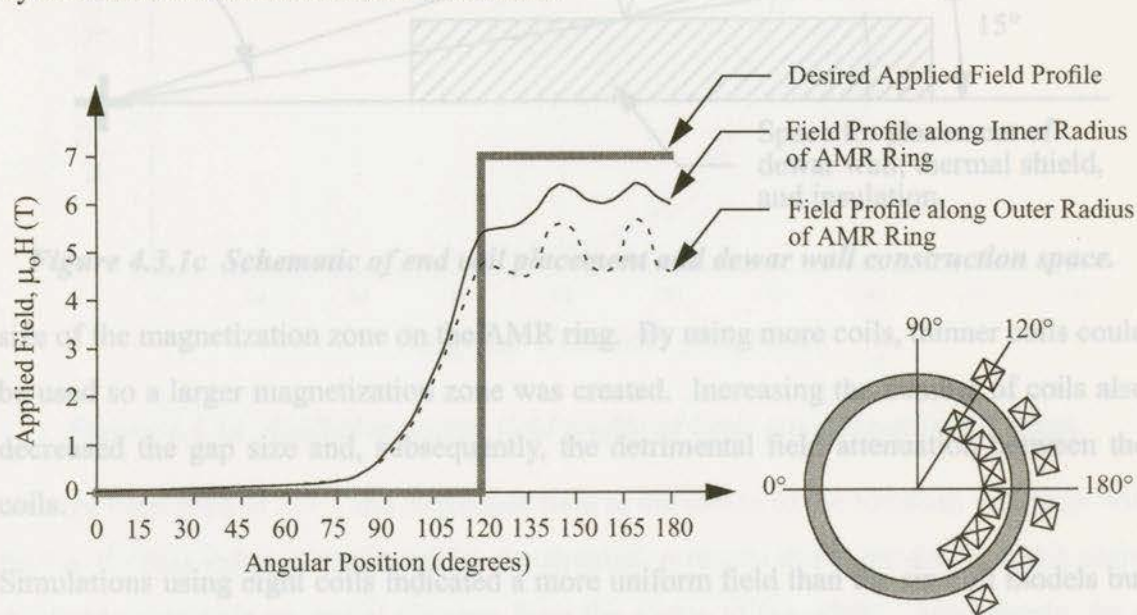


Figure 4.3.1b Sketch of the x-y plane applied field profile on the AMR ring of the six-coil partial tokamak model.

In the design shown in Figure 4.3.1a-B, iron wedges were placed between the coils to increase the field between the coils and, therefore, reduce the gap attenuation. This design did not significantly affect the field attenuation. Extending the wedges to a half circumference yoke, as in Figure 4.3.1a-C, and a full yoke, as in Figure 4.3.1a-D, also had little effect on the field attenuation. The only significant benefit of the yokes was the reduction of the stray fields outside of the main bore.

Within the 150° total construction space, a 15° space was allotted outside the edge of the end coils for the dewar, insulation, and thermal shield. This meant that the end coils had to be placed 120° apart from edge to edge, as shown in Figure 4.3.1c. Their center to center placement varied depending on the coil size and this placement directly affected the

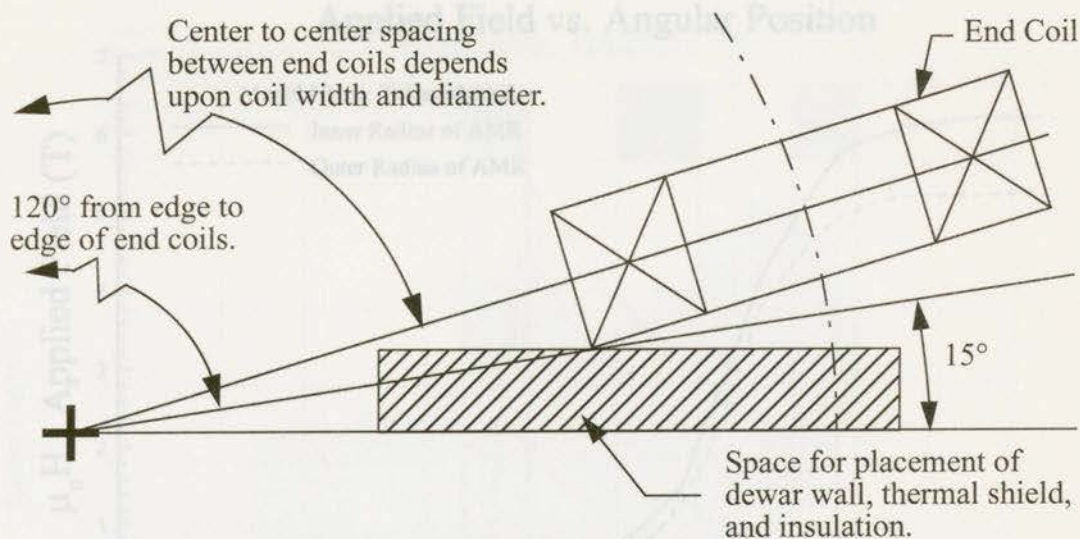


Figure 4.3.1c Schematic of end coil placement and dewar wall construction space.

size of the magnetization zone on the AMR ring. By using more coils, thinner coils could be used so a larger magnetization zone was created. Increasing the number of coils also decreased the gap size and, subsequently, the detrimental field attenuation between the coils.

Simulations using eight coils indicated a more uniform field than the six coil models but the field attenuation between the coils was on the order of 0.5 T, which was still undesirably large. Ten coil designs had less than a 0.2 T gap field attenuation, which is less than the 5% field homogeneity requirement, so all further simulations used ten coils.

The results of the earliest ten coil model are shown in Figure 4.3.1d. This shows the low gap field attenuation but the azimuthal and radial attenuation are still present. The coils for this simulation were modelled with a current density of $25,000 \text{ A/cm}^2$, had a 15 cm inner diameter, 22 cm outer diameter, and were 3.4 cm wide. They were spaced 12° apart so they spanned an arc of 108° from center to center and 120° from end to end.

The applied field within the magnetization zone of this ten coil model was approximately 5.7 T, along the center of the AMR ring, which is much less than the specified field of 7 T. The reason for this low field, as well as the 1 T radial field attenuation across the AMR ring, is the $1/r$ field dependence inherent to toroidal windings. This means that for an

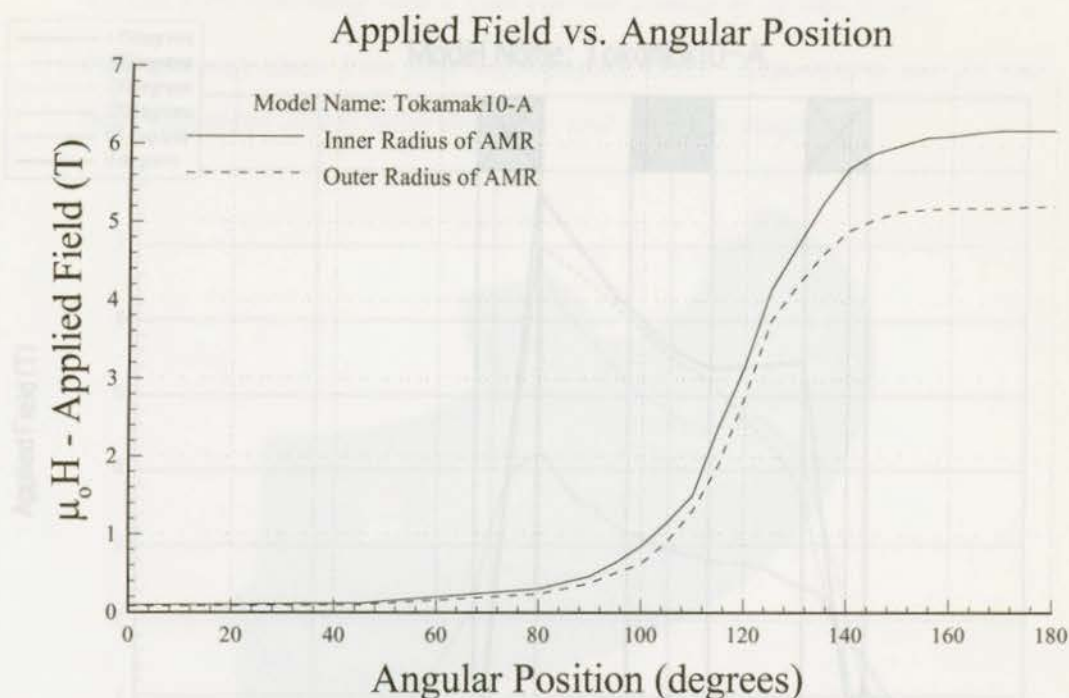


Figure 4.3.1d Applied magnetic field profile of basic ten coil partial tokamak.

average bore field of 5.7 T the maximum field at the inside of the tokamak windings will be 7.6 T. This value is confirmed by the simulation results in Figure 4.3.1e which show the field magnitude vs. radial distance from the center of the AMR. Accordingly, for a maximum field of 8 T in the windings, which is the chosen limit for the NbTi conductors, the maximum possible mean bore field is 6 T for this AMR ring diameter. The field magnitude specification of 7 T, therefore, cannot be met unless the AMR diameter is increased to 120 cm while keeping the coil bore size constant. The AMR size is fixed, however, so the 6 T mean applied field must be accepted as the maximum.

4.3.2 Compensating End Coils

Although the field attenuation in the radial direction can only be reduced by minimizing the ratio of the AMR ring outer to inner diameter, the gap field attenuation can be reduced by increasing the number of coils. It is also possible to reduce the azimuthal field attenuation by altering the size of some of the coils. The field magnitude decreases significantly near the ends of the partial tokamak so by using larger end coils, which produce a greater field than the other coils, the field can be increased in this end region.

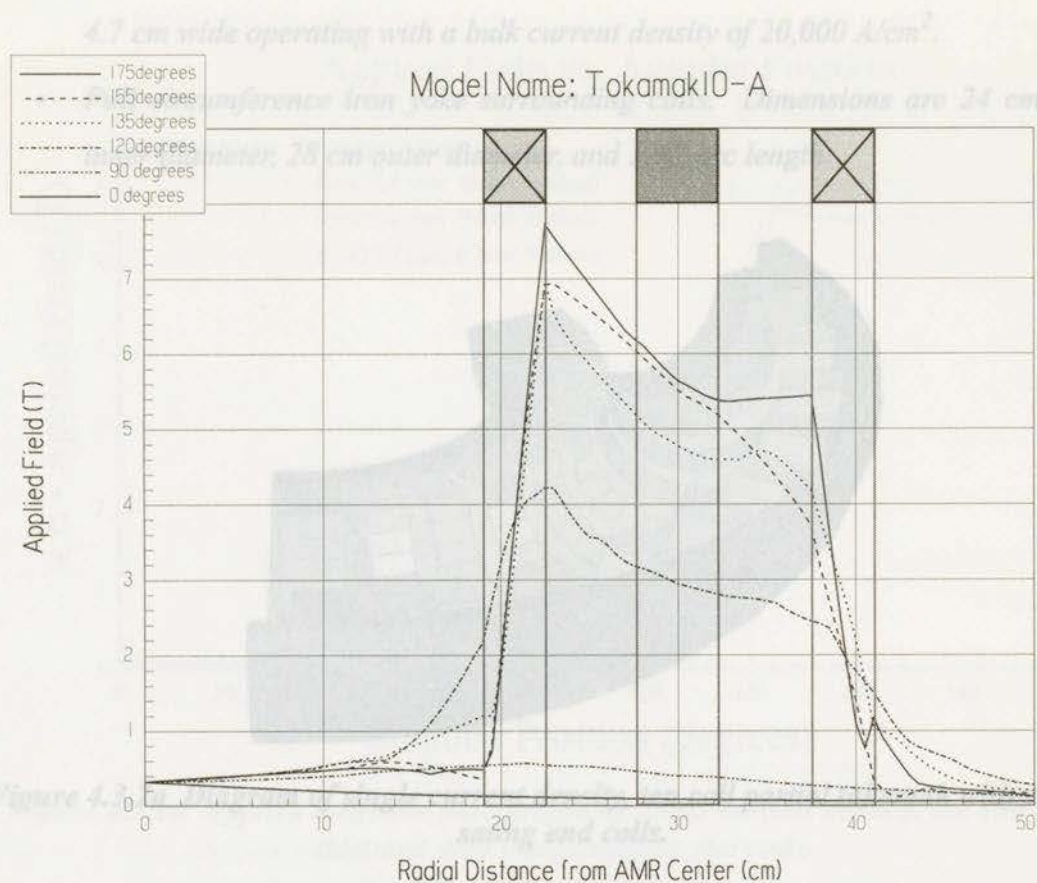


Figure 4.3.1e Graph of applied field along radial segments at various angular positions for basic ten coil partial tokamak.

Later simulations of the ten coil partial tokamak use these large compensating end coils. The later simulations also use coils with a 13 cm inner diameter, rather 15 cm as the earlier models, because the mechanical design of the AMR housing, which occurred in parallel with the magnetic design, indicated that 13 cm would suffice. These simulations still only use single current density windings but these windings are optimized later. After multiple simulations, the best results were found using the model shown in Figure 4.3.2a which has the following description:

- Eight main central coils spaced 12° apart. Winding dimensions of 13 cm inner diameter, 22 cm outer diameter, and 3.4 cm wide operating with a bulk current density of $20,000 \text{ A/cm}^2$.
- Two end compensating coils spaced 14° from neighboring main coil. Winding dimensions of 13 cm inner diameter, 25.2 cm outer diameter, and .

4.7 cm wide operating with a bulk current density of $20,000 \text{ A/cm}^2$.

- Full circumference iron yoke surrounding coils. Dimensions are 24 cm inner diameter, 28 cm outer diameter, and 128° arc length.

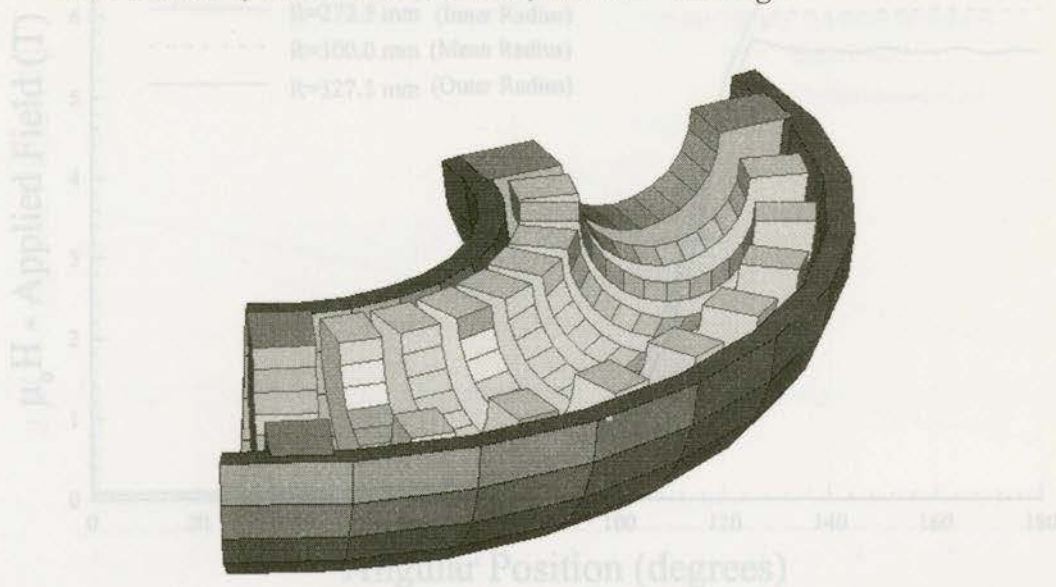


Figure 4.3.2a Diagram of single current density, ten coil partial tokamak with compensating end coils.

This simulation estimated a maximum field of 8 T within the windings which is the target maximum field for the NbTi conductor. The applied field profile of this simulation along the inner circumference, centerline, and outer circumference of the AMR ring is shown in Figure 4.3.2b. The reduction of the azimuthal field attenuation and the increased arc of magnetization is visible by comparing this profile with the one in Figure 4.3.1d of the basic partial tokamak. This reduction is due to both the compensating coils and the increased arc length of the partial tokamak. The earlier construction zone arc length of 15° for the dewar wall and shielding has been decreased to 10° allowing the coils to be placed farther apart.

This field profile has the greatest possible magnitude and size possible given geometric constraints of the AMR and the conductor limitations of a single current density winding. Now the coils may be optimized to use less superconducting wire making them, therefore, less expensive.

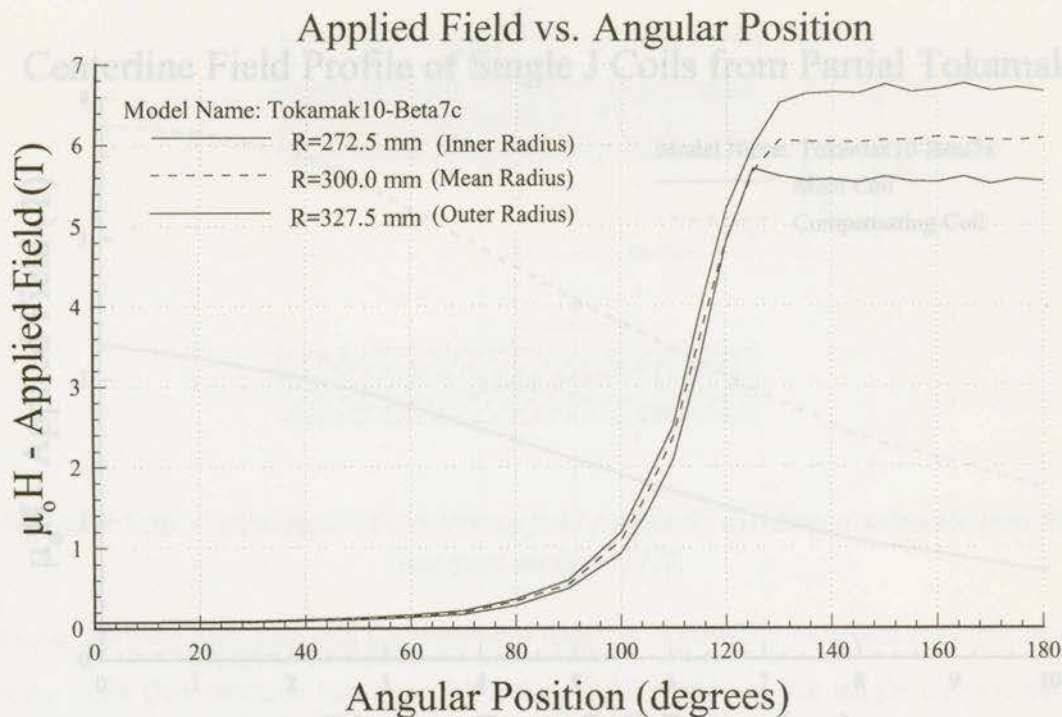


Figure 4.3.2b Applied magnetic field profile of single current density, ten coil partial tokamak with compensating end coils.

4.3.3 Winding Optimization

The method used to optimize the coils involves examining the field produced by one of the single current density coils of the partial tokamak and then creating multiple current density coils that produce the same field without exceeding the T-J-H limitations of the conductor. The outer windings of the coil operate at higher current densities than the inner windings because the local field is lower in the location of these outer windings. Because the partial tokamak uses two types of coils, main coils and compensating coils, each coil must be examined separately. A maximum bore field of 2.25 T and 3.8 T is produced by isolated main and compensating coils respectively as can be seen from the simulated centerline field profile of both of these coils in Figure 4.3.3a.

Using these equations, the field profile of a multiple current density coil is found by superimposing the analytically calculated field profiles of two separate windings of different diameters and current densities. Further, by adjusting the outer diameter of these coils,

Centerline Field Profile of Single J Coils from Partial Tokamak

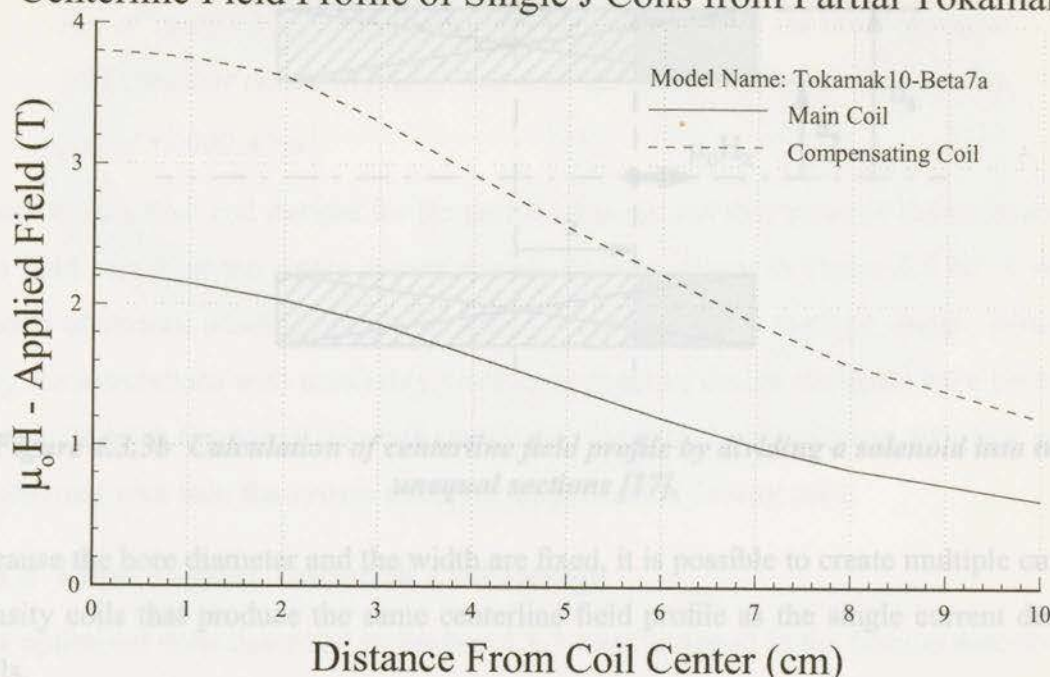


Figure 4.3.3a Applied field profiles along centerline of single current density, main and compensating coils from partial tokamak shown in Figure 4.3.2a.

The centerline field of a simple coil at any point z along the axis, as sketched in Figure 4.3.3b, may be calculated analytically using Equation (4.3.3a) and Equation (4.3.3b) along with the shape factors $\alpha = b_s/a_s$, $\beta_1 = (l-z)/a_s$, and $\beta_2 = (l+z)/a_s$ [17].

$$\mu_0 H_z = \frac{1}{2} J a_s \{ F(\alpha, \beta_1) + F(\alpha, \beta_2) \} \quad (4.3.3a)$$

$$F(\alpha, \beta) = \mu_0 \beta \log_e \left\{ \frac{\alpha + \sqrt{\alpha^2 + \beta^2}}{1 + \sqrt{1 + \beta^2}} \right\} \quad (4.3.3b)$$

Using these equations, the field profile of a multiple current density coil is found by superimposing the analytically calculated field profiles of two separate windings of different diameters and current densities. Further, by adjusting the outer diameter of these coils,

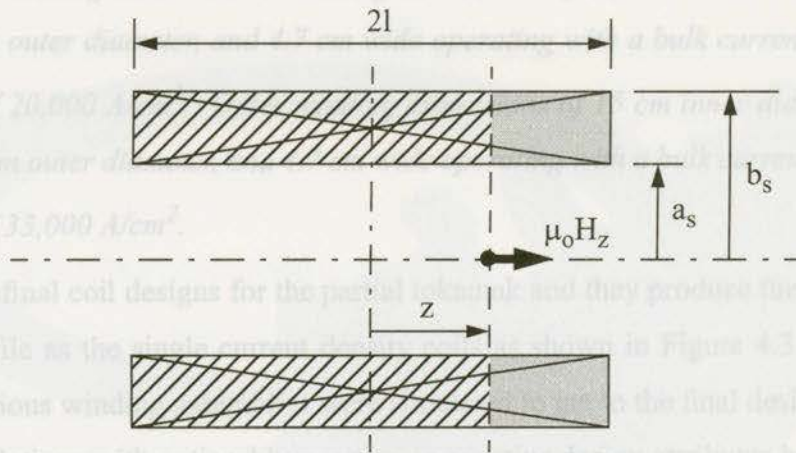


Figure 4.3.3b Calculation of centerline field profile by dividing a solenoid into two unequal sections [17].

because the bore diameter and the width are fixed, it is possible to create multiple current density coils that produce the same centerline field profile as the single current density coils.

The magnetostatic simulation shows that the field in the winding decreases from a maximum value at the inner bore of the winding to value of nearly zero at the outside of the winding. A conservative estimate is to assume that the magnetic field varies linearly through the winding from 8.5 T at the inner radius to 0 T at the outer radius. This assumption allows the radius where the current density must change to be estimated by knowing the field limit of the outer conductor. The manufacturer suggests changing the wire at the point in the coil where the field is 7 T for coils of this size [108]. At 7 T a suitable current density is 33,000 A/cm². Allowing for a 10% factor of safety, so that the changeover point occurs in a field of 6.3 T, it is possible to estimate the winding dimensions that produce the necessary centerline field profiles. The resulting coils are as follows:

- *Central coils: Inner winding dimensions of 13 cm inner diameter, 14.5 cm outer diameter, and 3.4 cm wide operating with a bulk current density of 20,000 A/cm². Outer winding dimensions of 14.5 cm inner diameter, 18.8 cm outer diameter, and 3.4 cm wide operating with a bulk current density of 33,000 A/cm².*

- *Compensating coils: Inner winding dimensions of 13 cm inner diameter, 15 cm outer diameter, and 4.7 cm wide operating with a bulk current density of 20,000 A/cm². Outer winding dimensions of 15 cm inner diameter, 20.6 cm outer diameter, and 4.7 cm wide operating with a bulk current density of 33,000 A/cm².*

These are the final coil designs for the partial tokamak and they produce the same center-line field profile as the single current density coils as shown in Figure 4.3.3a. Over 60 models of various winding assemblies were simulated to get to the final design. However, only the simulations with noticeably positive or negative design attributes have been presented. In total, the partial tokamak using these optimized coils requires 40% less superconducting wire than the system using the single current density coils.

4.3.4 Final Partial Tokamak Coil Design

The optimized coils described in Section 4.3.3 were arranged in the fashion described in Section 4.3.2 to form the final design of the partial tokamak coil configuration. The main coils were spaced 12° apart and the compensating coils were spaced 14° from the neighboring main coil. The iron yoke was increased in size from the previous designs to form a toroidal shaped shield, as seen in Figure 4.3.4a, with an inner diameter of 30 cm, and outer diameter of 34 cm, and an arc length of 132°. This large yoke is split into top and bottom shells so the coils may be assembled together. The yoke also functions as a thermal radiation shield as its operating temperature is around 50 K. The field profile of this final design is the same as the profile described in Figure 4.3.2b with a mean bore field of 6 T extending over an arc length of just over 100°. The coils were designed to operate at 4.5 K with a maximum local field on the windings of 8.5 T.

Three superconducting magnet manufacturers were contacted about these coils and asked to provide a rough cost estimate and any comments regarding the manufacturing of these coils. The feedback from these manufacturers is presented in Table 4.3.4a. The manufacturer's comments were not extremely encouraging and, therefore, were carefully considered during the critical design review of this system.

Table 4.3.4a: Manufacturer's initial cost estimate and comments of partial tokamak coils.

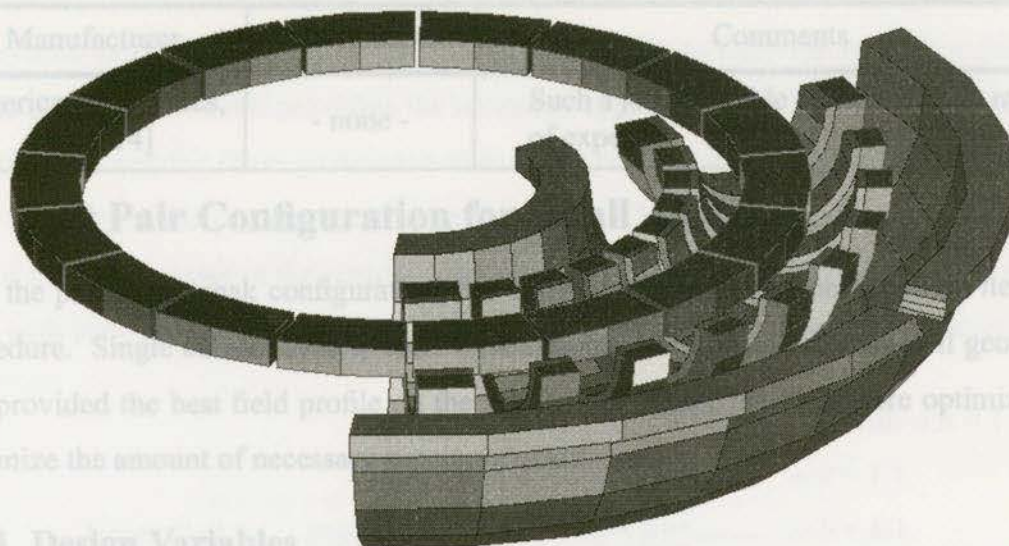


Figure 4.3.4a Schematic of final partial tokamak coil design.

Table 4.3.4a: Manufacturer's initial cost estimate and comments of partial tokamak coils.

Manufacturer	Cost Estimate	Comments
Cryomagnetics, Inc. [112]	\$4,250 (US) per main coil. \$7,500 (US) per compensating coil.	<ol style="list-style-type: none"> 1) Magnetic forces are uncertain and will affect bobbin design. 2) Their magnetics software cannot handle the partial tokamak arrangement so they will trust the design as is but not guarantee the performance. 3) Pricing includes testing in LHe, quench protection, but not the persistent switches. 4) Manufacturing seems straightforward.
Oxford Instruments, Inc. [113]	\$10,000 (US) per coil	<ol style="list-style-type: none"> 1) Current densities are too high according to their experience. 2) $\alpha > 1.4$ for both types of coils which suggests delamination problems due to thermal contraction. 3) Many uncertainties so cost estimating is difficult.

Figure 4.4.1a Variable dimensions of elliptical, split pair coils.

Table 4.3.4a: Manufacturer's initial cost estimate and comments of partial tokamak coils.

Manufacturer	Cost Estimate	Comments
American Magnetics, Inc. [114]	- none -	Such a job is outside of their current range of expertise.

4.4 Split Pair Configuration for Small AMRL

Like the partial tokamak configuration, the design of the split pair coils was an iterative procedure. Single current density coils were simulated to find an effective coil geometry that provided the best field profile on the AMR ring. Then, the coils were optimized to minimize the amount of necessary superconductor.

4.4.1 Design Variables

There are many dimensions of elliptical, split pair coils, as shown in Figure 4.4.1a, that may be varied to create the desired magnetic field profile and magnitude. The inner width and length dimensions, a and b , affect the size of the magnetization zone as well as the peak field in the coil, which limits the current density of the conductor. The peak field occurs at the inner side of the coil at the ends of the long axis because at this point the winding has the greatest curvature. Therefore, as the ratio $b:a$ increases, the ratio of the peak field to the bore field also increases. The separation distance, s , between the coils is one of the more influential dimensions as it significantly affects the magnitude of the field between the coils as described by Barclay et al [45]. Like the partial tokamak, this gap attenuation can only be reduced by placing the coils as close together as possible.

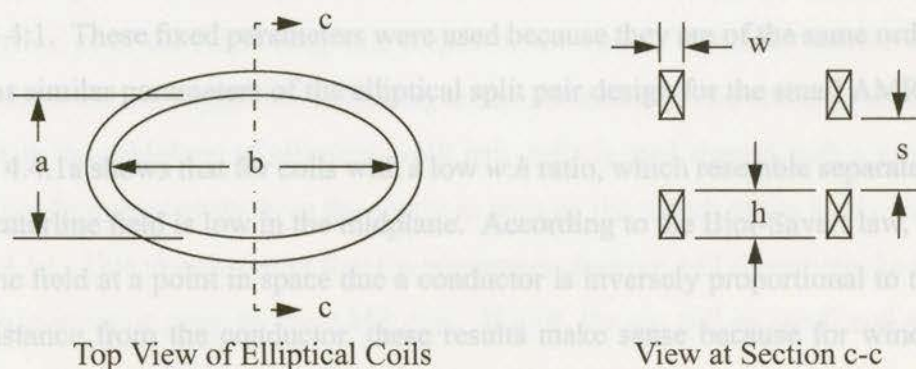


Figure 4.4.1a Variable dimensions of elliptical, split pair coils.

The field distribution is also affected by the width, w , and height, h , of the winding but, additionally, these variables affect the winding volume. Therefore, the height and width dimensions of the winding must be considered carefully to keep the winding volume as low as possible while still providing the necessary applied field. A good way to determine the effect of varying these parameters is to examine the centerline field of two circular coils in a Helmholtz configuration using Equation (4.3.3a) and Equation (4.3.3b). Table 4.4.1a shows estimates of the centerline applied field in the midplane and coil bore of two coils with varying $w:h$ ratios as sketched in Figure 4.4.1b. These coils have an inner diam-

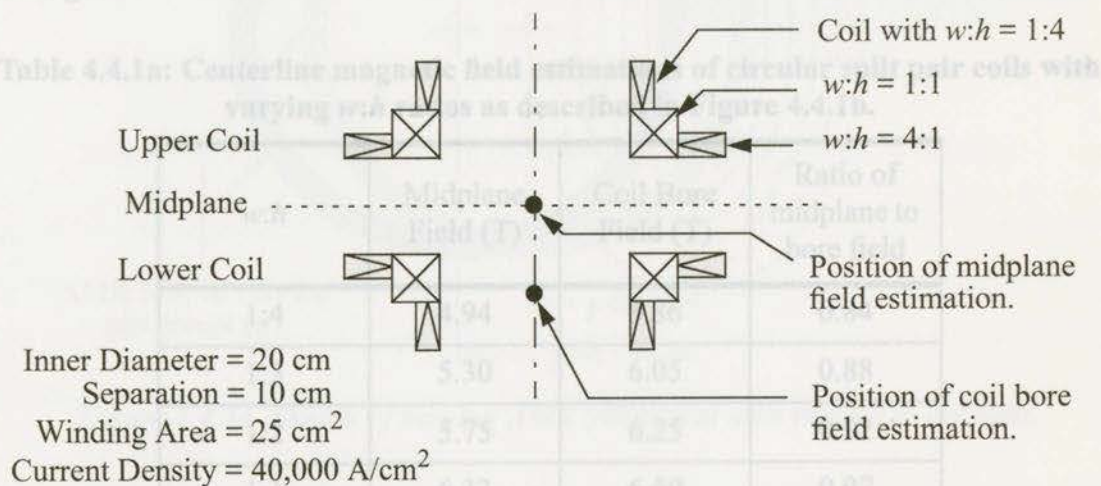


Figure 4.4.1b Sketch of circular split pair coils with varying $w:h$ ratios.

eter of 20 cm, a separation distance of 10 cm, a fixed winding area of 25 cm², and operate with a uniform current density of 40,000 A/cm². Although these parameters also affect the field profile, they were held constant while the width to height ratio was varied from 1:4 to 4:1. These fixed parameters were used because they are of the same order of magnitude as similar parameters of the elliptical split pair design for the small AMRL. The field

Table 4.4.1a shows that for coils with a low $w:h$ ratio, which resemble separated solenoids, the centerline field is low in the midplane. According to the Biot-Savart law, which states that the field at a point in space due a conductor is inversely proportional to the square of the distance from the conductor, these results make sense because for windings of this configuration much of the conductor is located far away from the midplane. As the $w:h$ ratio of these coils increases, making them resemble separated “pancake” coils, the mid-

plane field approaches a maximum and then decreases. This eventual decrease in field makes sense for the same reason that the midplane field is low for coils with a small $w:h$ ratio. Although the midplane field approaches a maximum for coils of this shape, pancake coils also produced very high, and undesirable, fields on the windings at inner circumference of the coils. This occurs because coils with low β and high α values have high ratios of maximum field to central field [17]. Therefore, coils with a $w:h$ ratio near unity will most likely have a good balance of the characteristics needed to provide a midplane field of the required magnitude without producing unreasonably high local fields within the windings.

Table 4.4.1a: Centerline magnetic field estimations of circular split pair coils with varying $w:h$ ratios as described in Figure 4.4.1b.

$w:h$	Midplane Field (T)	Coil Bore Field (T)	Ratio of midplane to bore field
1:4	4.94	5.86	0.84
1:3	5.30	6.05	0.88
1:2	5.75	6.25	0.92
1:1	6.33	6.50	0.97
2:1	6.62	6.56	1.01
3:1	6.64	6.43	1.03
4:1	6.59	6.37	1.03

The other geometric variable that affects the field distribution on the AMR ring is the placement, p , of the AMR ring with respect to the coils. The placement distance is measured from the center of the AMR ring to the centerline of the elliptical coils. The field profile in the midplane of elliptical, split pair coils is oval shaped with a uniform central field that decreases away from the center as seen by the sketch of the field contours in Figure 4.4.1c. This sketch shows that the placement distance will determine the arc length of the magnetization zone on the AMR ring. If $p > R$, the arc will be small and as p becomes

increased. The applied field of this design was calculated to be only 6.3 T over a 60° arc length of the AMR ring. Although this was the best design of the NBTI split pair coils, it still did

less than R the magnetization zone increases. However, if $p \ll R$ the ring will be placed outside the region of highest field so the optimal placement will likely be a value slightly less than the radius.

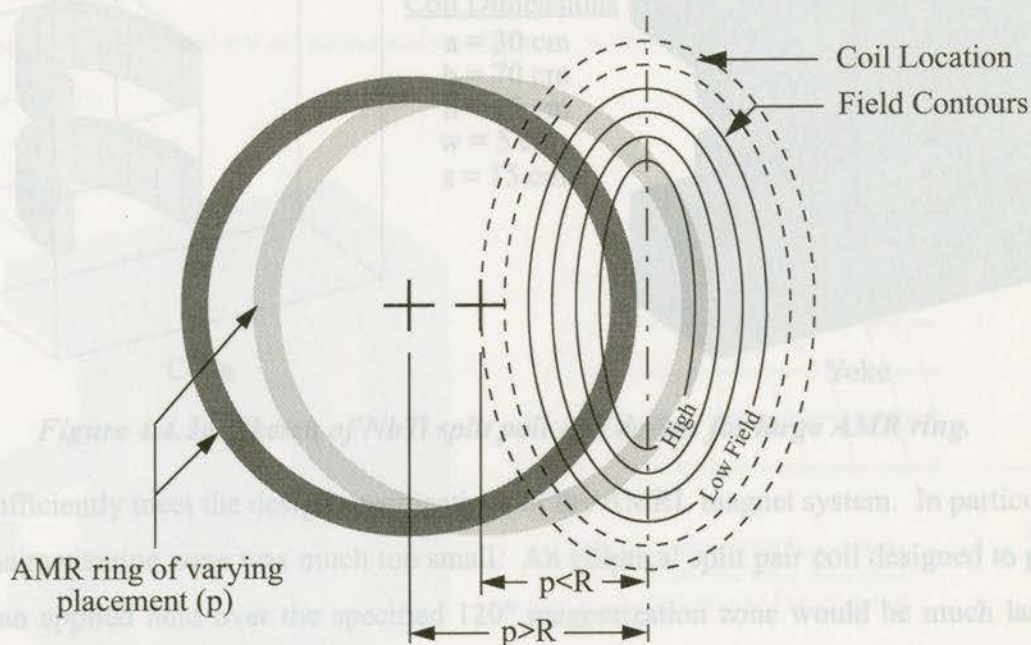


Figure 4.4.1c Sketch of varying AMR placement with respect to the coils.

4.4.2 Design Evolution of Split Pair Coils for the AMRL

Initial simulations of split pair coils with NbTi conductors were made to see if a split pair coil design could be applied to the first AMRL design with the large AMR ring. Figure 4.4.2a shows a cutaway sketch of one of these designs. It is modelled with a very large yoke to examine the effect of a large flux return path even though a yoke of this size is too large for a real system.

All of the early designs of these NbTi windings were made to operate at a single current density of $19,000 \text{ A/cm}^2$ with a maximum local field in the windings of 8.5 T. The designs of the NbTi split pair coils were examined over a parameter space which included variable windings dimensions and yoke dimensions but a fixed separation distance of 15 cm. The design in Figure 4.4.2a provided the best results of all of the NbTi designs examined. The applied field of this design was calculated to be only 6.3 T over a 60° arc length of the AMR ring. Although this was the best design of the NbTi split pair coils, it still did

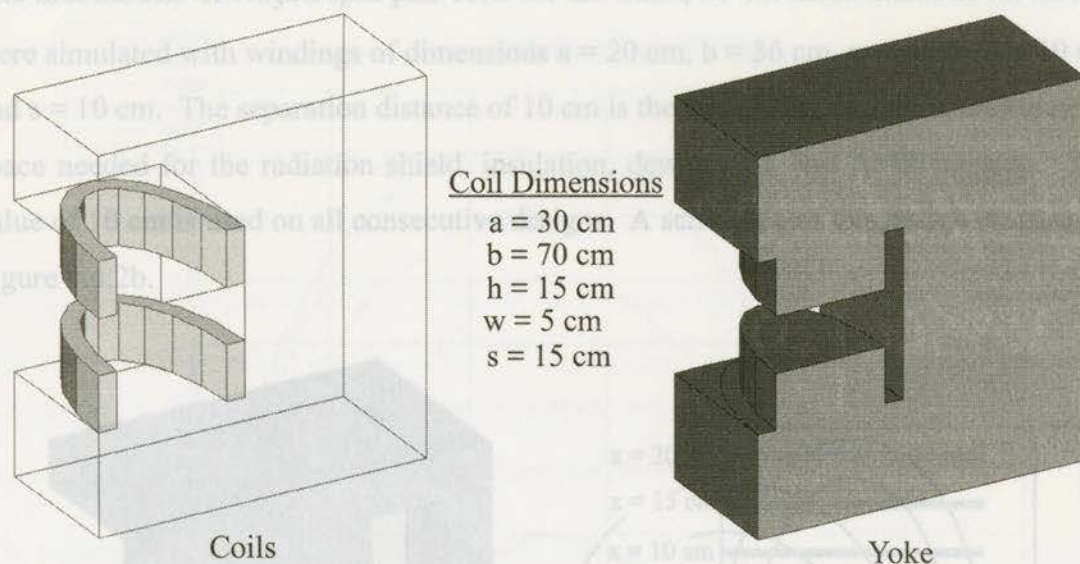


Figure 4.4.2a Sketch of NbTi split pair coil design for large AMR ring.

not sufficiently meet the design specifications of the AMRL magnet system. In particular, the magnetization zone was much too small. An elliptical split pair coil designed to provide an applied field over the specified 120° magnetization zone would be much larger and, therefore, prohibitively expensive. Therefore, further designs of NbTi split pair coils for the first AMRL were abandoned.

Figure 4.4.2b Sketch of Nb₃Sn split pair coil model with 5 cm wide yoke.

There was some investigation into the design of Nb₃Sn split pair coils for the first AMRL but it was immediately obvious that the coils would still have to be very large and, therefore, prohibitively expensive. There was no affordable magnet design that could meet the specification of the first AMRL so the specifications of the AMRL were changed such that an affordable magnet design was possible. The second AMRL design was specified to have a smaller AMR ring diameter and a smaller magnetization zone. The specifications of this second, smaller AMRL are given in Section 3.2.2.

The option of using NbTi split pair coils for this smaller AMRL was briefly examined but it was concluded that the coils would still be too large and expensive. It was, therefore, decided that the coils were to be made of Nb₃Sn conductors.

The first models of Nb_3Sn split pair coils for the small, 30 cm mean diameter AMR ring were simulated with windings of dimensions $a = 20$ cm, $b = 36$ cm, $w = 4$ cm, $h = 10$ cm, and $s = 10$ cm. The separation distance of 10 cm is the minimum possible considering the space needed for the radiation shield, insulation, dewar wall, and AMR housing. This value of 10 cm is used on all consecutive designs. A schematic of this design is shown in Figure 4.4.2b.

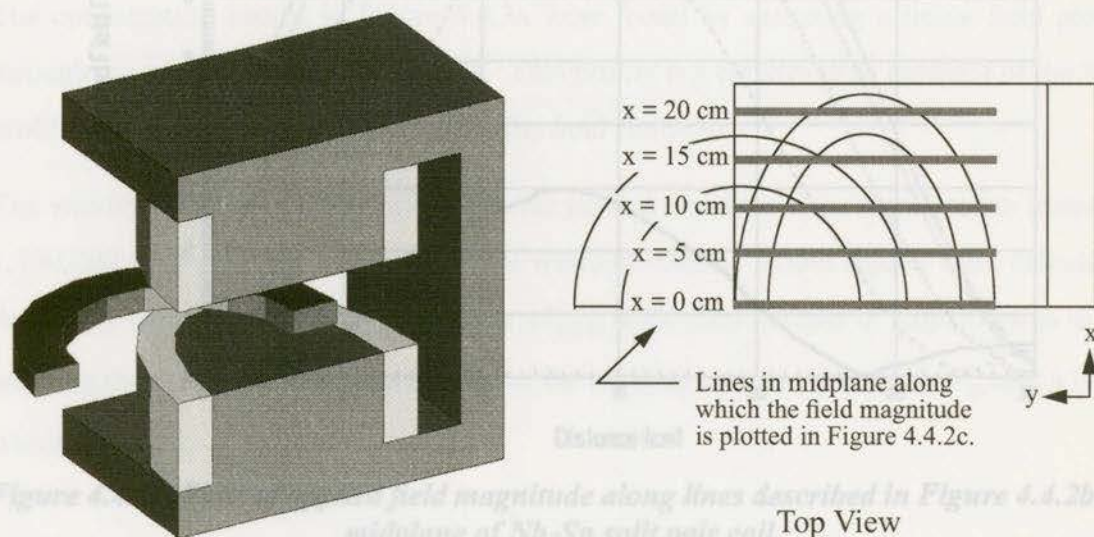


Figure 4.4.2b Sketch of Nb_3Sn split pair coil model with 5 cm wide yoke.

For a current density of $43,250 \text{ A/cm}^2$, coils of these dimensions produce a maximum local field in the windings of 14 T. Although the current density was too high for the conductor in this field, refining the model to correct this current density was considered unnecessary because the windings were to be refined later during the optimization. So, for peak field values of 14 T, these models provided fields in the midplane of 8 T to 9.5 T depending on the size of the yoke. The yoke thickness was fixed at 5 cm because this was the size of the steel plate available for construction. Thicker yokes also provided only a marginal increase in the applied field in the midplane and increased the weight of the assembly. The field profile along the midplane lines displayed in Figure 4.4.2b of this Nb_3Sn split pair coil is shown in Figure 4.4.2c.

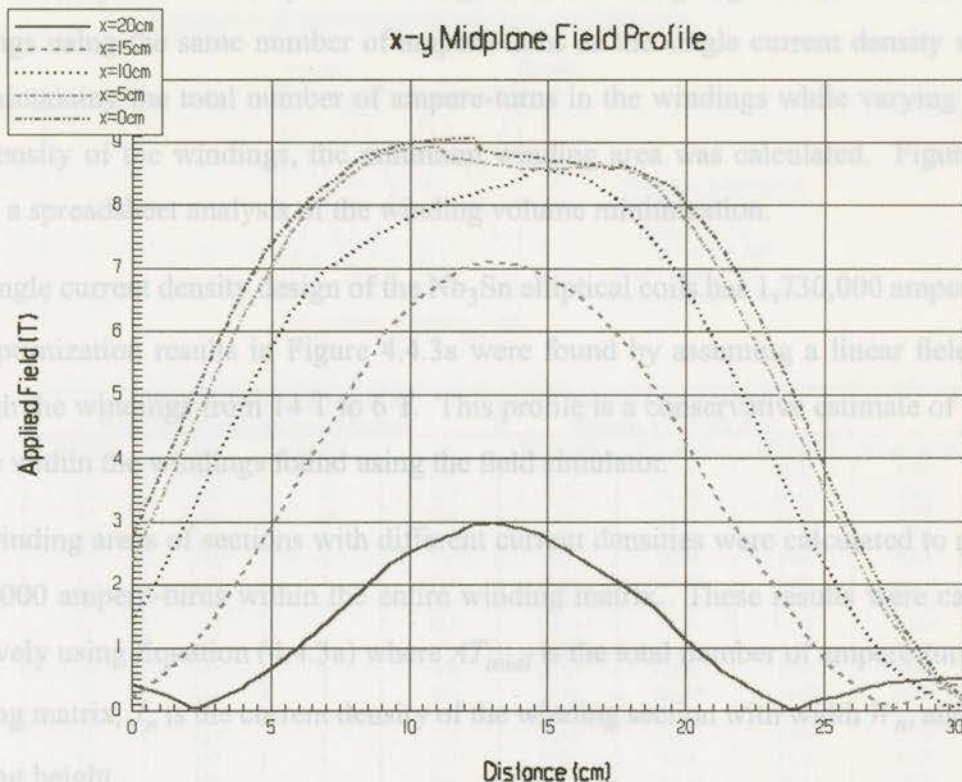


Figure 4.4.2c Plots of applied field magnitude along lines described in Figure 4.4.2b in midplane of Nb_3Sn split pair coil.

This design provides an acceptably sized magnetization zone of 90° of the necessary magnitude however, like the single current density partial tokamak designs, the windings may be optimized to use multiple current densities so less conductor material is needed.

4.4.3 Winding Optimization

This section presents a technique for reducing the total volume and, therefore, cost of the windings without sacrificing the performance of the coils. An example of this technique is shown but not the final optimized design of the windings is not shown. Further refinement by Dr. Jeffery Hall resulted in the final design of the elliptical, split pair coils as presented in the following section.

The solenoids from the partial tokamak were optimized by designing a multiple current density coil, using simple analytic expressions, that produce the same centerline field as a single current density coil. However, unlike simple solenoids, there is no simple, analytic expression that describes the centerline field of elliptical windings. Therefore, the optimi-

zation technique for the elliptical windings involved designing multiple current density windings using the same number of ampere-turns as the single current density winding. By maintaining the total number of ampere-turns in the windings while varying the current density of the windings, the minimum winding area was calculated. Figure 4.4.3a shows a spreadsheet analysis of the winding volume minimization.

The single current density design of the Nb₃Sn elliptical coils has 1,730,000 ampere-turns. The optimization results in Figure 4.4.3a were found by assuming a linear field profile through the windings from 14 T to 6 T. This profile is a conservative estimate of the field profile within the windings found using the field simulator.

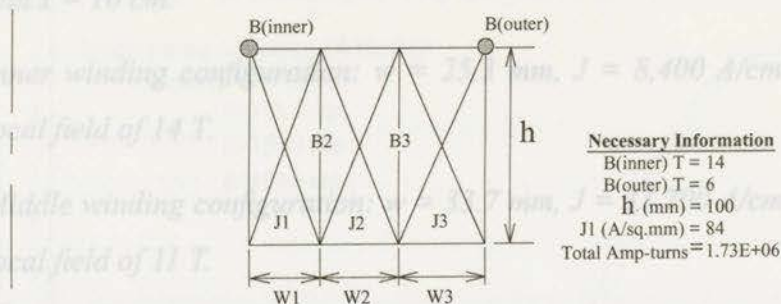
The winding areas of sections with different current densities were calculated to maintain 1,730,000 ampere-turns within the entire winding matrix. These results were calculated iteratively using Equation (4.4.3a) where AT_{total} is the total number of ampere-turns in the winding matrix, J_n is the current density of the winding section with width W_n , and h is the winding height.

$$AT_{total} = h (J_1 W_1 + J_2 W_2 + J_3 W_3) \quad (4.4.3a)$$

The winding widths were calculated with Equation (4.4.3a) and then the applied field (B_2 and B_3 in Figure 4.4.3a) was estimated at the position where the current density changes. If the current density was too high for the local field then the widths of the winding were re-calculated until the field-current density relationship was satisfied. The minimum winding area was found by varying the limit of the local applied field in the winding from 13 T to 7 T along with the appropriate current density. Although this is not exactly a true optimization method, because the redistribution of the current densities in the current loop may affect the overall field profile, the results were considered close enough to the optimal winding configuration. For this optimization of 1,730,000 ampere-turns, the minimum volume winding configuration is as follows:

Figure 4.4.3a Spreadsheet results of winding area minimization for three-winding Nb₃Sn elliptical coils.

Multiple Wire Wrapped Superconducting Coil - Size Optimization



Range of Applied Fields and Associated Practical Current Densities (A/sq.mm)				Iterative Calculations of Winding Width and Area			
B2 (T)	J2	B3 (T)	J3	W1 (mm)	W2 (mm)	W3 (mm)	X-Sec. Area
13	156	12	231	11.12	22.24	55.61	8897
13	156	11	337	9.08	27.24	36.32	7263
13	156	10	445	8.44	33.77	25.33	6755
13	156	9	555	8.74	43.69	17.48	6991
13	156	8	707	9.99	59.93	9.99	7991
13	156	7	861	14.67	102.68	0.00	11735
12	231	11	337	18.43	27.64	27.64	7372
12	231	10	445	17.41	34.81	17.41	6963
12	231	9	555	18.37	45.93	9.19	7348
12	231	8	707	22.20	66.60	0.00	8880
12	231	7	861	37.34	130.68	-18.67	14935
11	337	10	445	25.31	33.74	8.44	6748
11	337	9	555	26.72	44.53	0.00	7124
11	337	8	707	33.02	66.05	-11.01	8807
11	337	7	861	58.21	135.83	-38.81	15523
10	445	9	555	34.40	43.00	-8.60	6879
10	445	8	707	43.34	65.01	-21.67	8668
10	445	7	861	79.49	139.11	-59.62	15899

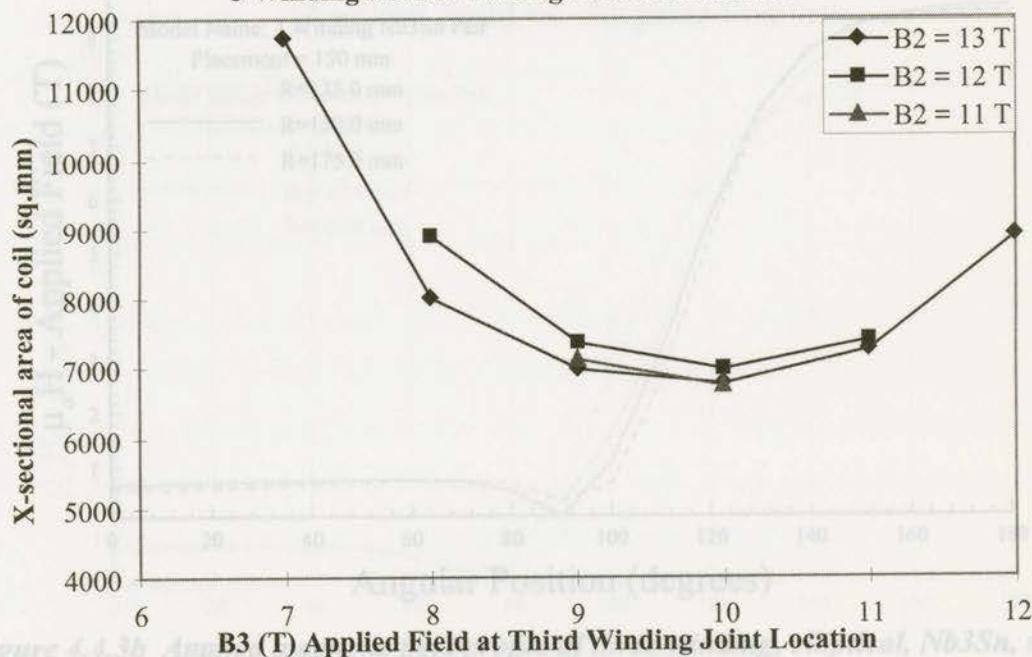
3 Winding Nb₃Sn Winding Area Minimization

Figure 4.4.3a Spreadsheet results of winding area minimization for three-winding Nb₃Sn elliptical coils.

- Elliptical, split pair coil dimensions of $a = 20$ cm, $b = 36$ cm, $h = 10$ cm, and $s = 10$ cm.
- Inner winding configuration: $w = 25.3$ mm, $J = 8,400$ A/cm², maximum local field of 14 T.
- Middle winding configuration: $w = 33.7$ mm, $J = 33,700$ A/cm², maximum local field of 11 T.
- Outer winding configuration: $w = 8.4$ mm, $J = 44,500$ A/cm², maximum local field of 10 T.

After the elliptical split pair coils were optimized, they were modelled with the magneto-static simulator to verify the resulting applied field on the AMR ring. The simulation results of this three-winding model are shown in Figure 4.4.3b, Figure 4.4.3c, and Figure 4.4.3d. Each of these figures shows the applied field profile on the AMR ring for different ring placement distances. These figures show that, as expected, the size of the magnetiza-

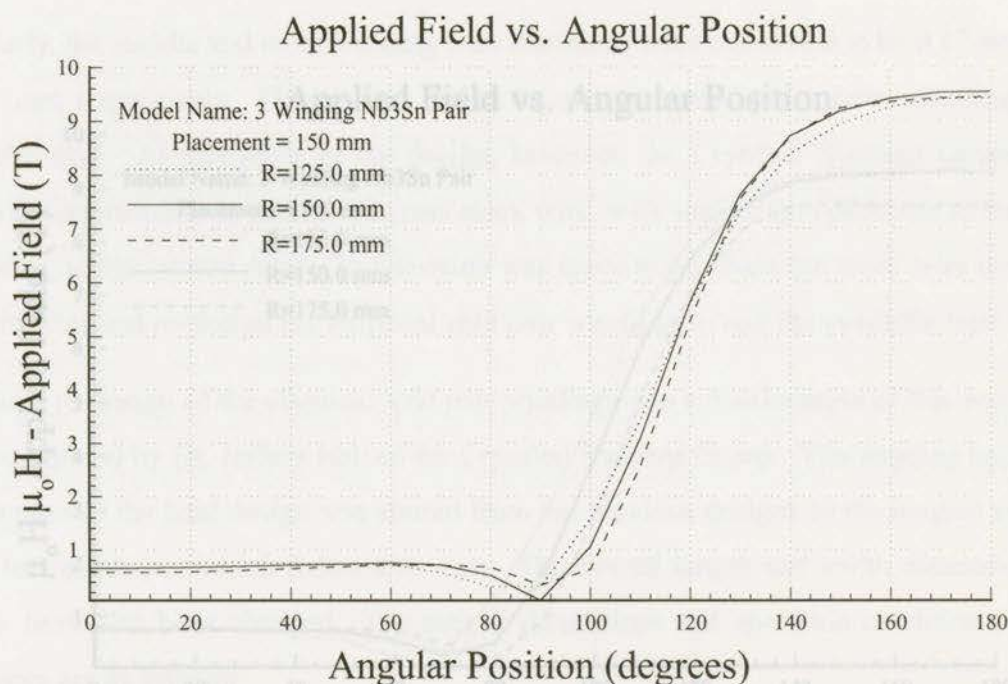


Figure 4.4.3b Applied magnetic field profile of three-winding, elliptical, Nb3Sn, split pair coils around an AMR ring with a placement distance of 15 cm.

Figure 4.4.3d Applied magnetic field profile of three-winding, elliptical, Nb3Sn, split pair coils around an AMR ring with a placement distance of 11 cm.

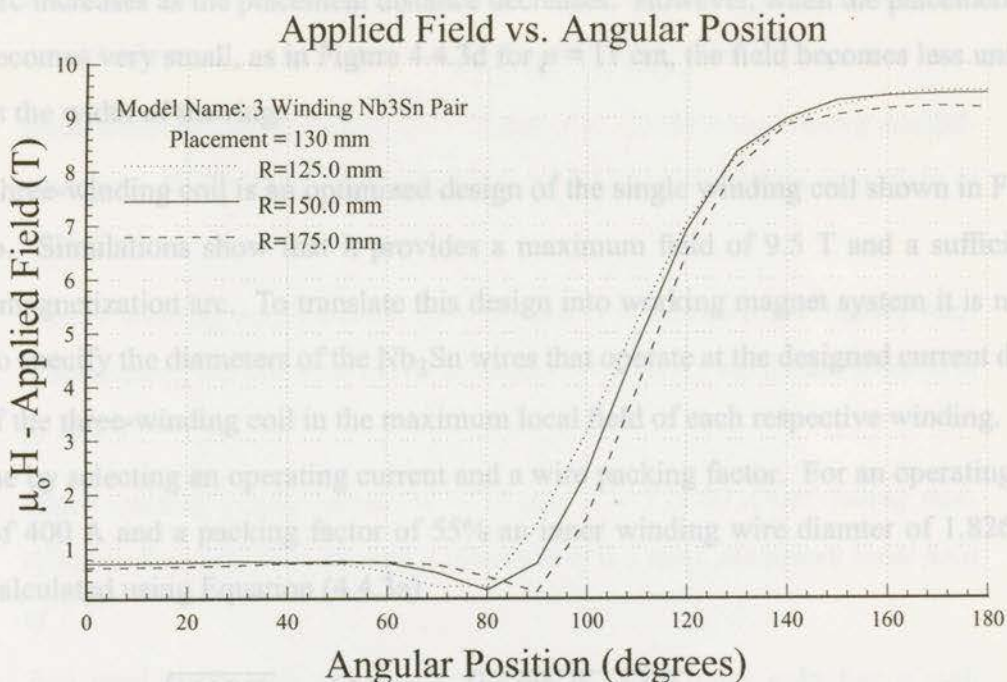


Figure 4.4.3c Applied magnetic field profile of three-winding, elliptical, Nb3Sn, split pair coils around an AMR ring with a placement distance of 13 cm.

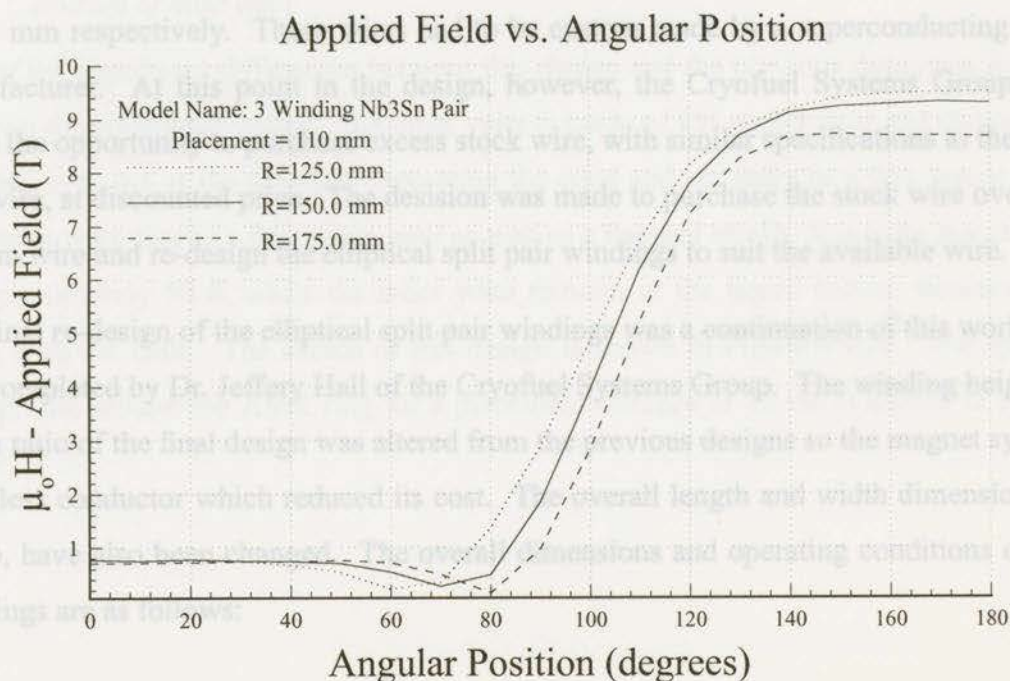


Figure 4.4.3d Applied magnetic field profile of three-winding, elliptical, Nb3Sn, split pair coils around an AMR ring with a placement distance of 11 cm.

tion arc increases as the placement distance decreases. However, when the placement values becomes very small, as in Figure 4.4.3d for $p = 11$ cm, the field becomes less uniform across the width of the ring.

This three-winding coil is an optimized design of the single winding coil shown in Figure 4.4.2b. Simulations show that it provides a maximum field of 9.5 T and a sufficiently large magnetization arc. To translate this design into working magnet system it is necessary to specify the diameters of the Nb_3Sn wires that operate at the designed current densities of the three-winding coil in the maximum local field of each respective winding. This is done by selecting an operating current and a wire packing factor. For an operating current of 400 A and a packing factor of 55% an inner winding wire diameter of 1.826 mm was calculated using Equation (4.4.3a)

$$d_w = \sqrt{\frac{4I(PF)}{J\pi}} = \left(\frac{10\text{mm}}{1\text{cm}}\right) \sqrt{\frac{4(400\text{A})(0.55)}{\left(8400\frac{\text{A}}{\text{cm}^2}\right)\pi}} = 1.826\text{mm} \quad (4.4.3a)$$

Similarly, the middle and outer winding wire diameters were calculated to be 0.87 mm and 0.793 mm respectively. These wires had to be custom made by a superconducting wire manufacturer. At this point in the design, however, the Cryofuel Systems Group was given the opportunity to purchase excess stock wire, with similar specifications to the custom wire, at discounted price. The decision was made to purchase the stock wire over the custom wire and re-design the elliptical split pair windings to suit the available wire.

The final re-design of the elliptical split pair windings was a continuation of this work and was completed by Dr. Jeffery Hall of the Cryofuel Systems Group. The winding height to width ratio of the final design was altered from the previous designs so the magnet system used less conductor which reduced its cost. The overall length and width dimensions, a and b , have also been changed. The overall dimensions and operating conditions of the windings are as follows:

- *Elliptical, split pair coil dimensions of $a = 15$ cm, $b = 30$ cm, $h = 5$ cm, and $s = 10.32$ m.*
- *Inner winding configuration: $w = 15$ mm, $J = 23,000$ A/cm² (using multifilamentary, Nb₃Sn wire with a diameter of 1.2 mm), maximum local field of 12.6 T.*
- *Middle winding configuration: $w = 30$ mm, $J = 32,100$ A/cm² (using multifilamentary, Nb₃Sn wire with a diameter of 1.0 mm), maximum local field of 11.5 T.*
- *Outer winding configuration: $w = 15$ mm, $J = 73,600$ A/cm² (using multifilamentary, Nb₃Sn wire with a diameter of 0.6 mm), maximum local field of 7 T.*
- *Two steel yokes with concentric placement. The inner yoke has a wall thickness of 5 cm, mechanically separates the upper and lower coil, and is constructed of 9% nickel steel. The outer yoke has a wall thickness of 5 cm, acts as a flux return path as well as a thermal shield, and is constructed of mild steel.*

One of the significant differences between this design and the previous designs is the use of a two ferromagnetic yokes. The inner yoke is made of 9% nickel steel and its primary function is to act as the structure separating the coils and secondly as a flux return path. The outer yoke acts as a flux return path as well as a thermal shield. It is to be maintained at approximately 50 K while the inner yoke remains at the liquid helium temperatures along with the coils. The sketch of this design is shown in Figure 4.4.3e. The applied field profile around the AMR ring for a placement distance of 15 cm is shown in Figure 4.4.3f.



Figure 4.4.3f Applied magnetic field profile of final split pair coil design around AMR ring with a placement distance of 15 cm.

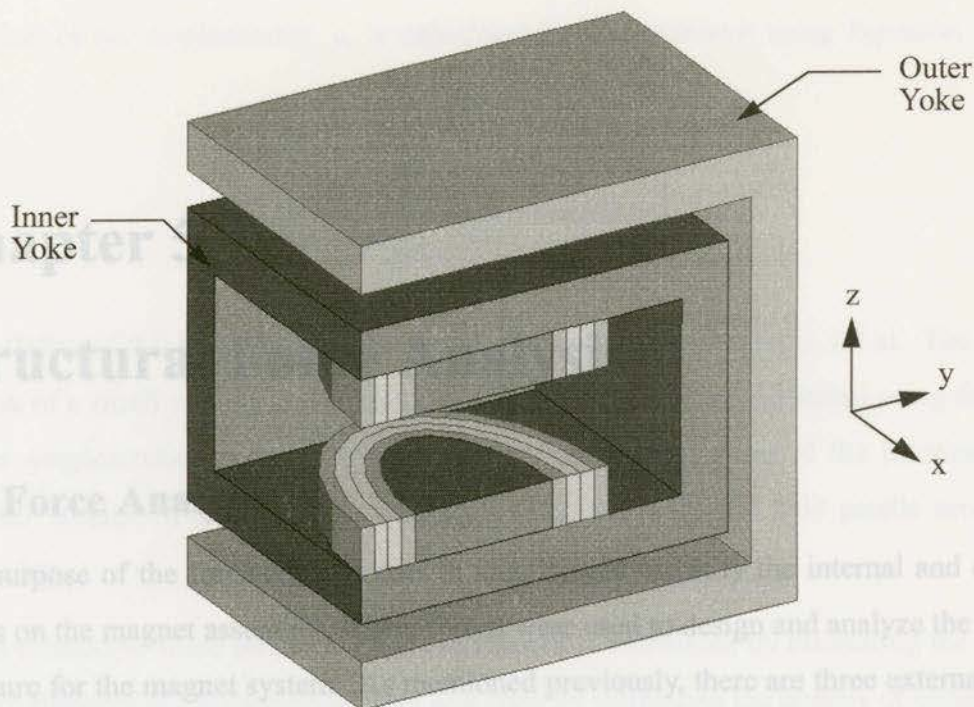


Figure 4.4.3e Sketch of final Nb_3Sn , elliptical, split pair coil design.

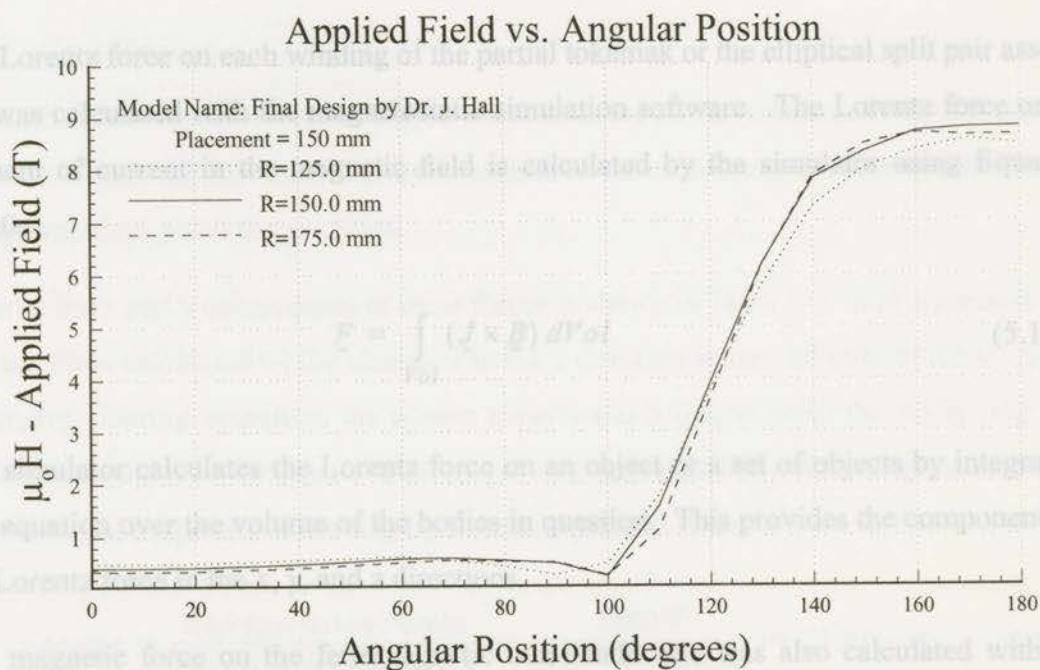


Figure 4.4.3f Applied magnetic field profile of final split pair coil design around AMR ring with a placement distance of 15 cm.

energy of the system due to a small displacement of the body. The force on a body in the direction of the displacement, c , is calculated by the simulator using Equation (5.1.0b) (115).

Chapter 5

$$F_c = \frac{\partial}{\partial c} \left[\frac{1}{2} \int_{Vol} \left(\int_0^{2\pi} B \cdot dH \right) dVol \right] \quad (5.1.0b)$$

Structural Force Analysis

5.1 Force Analysis

The purpose of the force analysis was to identify and quantify the internal and external forces on the magnet assembly. These forces were used to design and analyze the support structure for the magnet system. As mentioned previously, there are three external forces that act on the SC magnet sub-system. The Lorentz forces acting between coils, the magnetic forces acting between all magnetic material and the coils, and the gravitational body forces on the entire system assembly.

The Lorentz force on each winding of the partial tokamak or the elliptical split pair assembly was calculated with the magnetostatic simulation software. The Lorentz force on an element of current in the magnetic field is calculated by the simulator using Equation (5.1.0a).

$$\underline{F} = \int_{Vol} (\underline{J} \times \underline{B}) dVol \quad (5.1.0a)$$

The simulator calculates the Lorentz force on an object or a set of objects by integrating this equation over the volume of the bodies in question. This provides the components of the Lorentz force in the x, y, and z directions.

The magnetic force on the ferromagnetic non-conductors was also calculated with the simulator. Maxwell 3D™ computes the magnetic force on bodies using the principle of virtual work. This technique calculates the force on a body based on the change in the

energy of the system due to a small displacement of the body. The force on a body in the direction of the displacement, c , is calculated by the simulator using Equation (5.1.0b) [115].

$$F_c = \frac{\partial}{\partial c} \left[\frac{1}{2} \int_{Vol} \left(\int_0^H B \cdot dH \right) dVol \right] \quad (5.1.0b)$$

The validity of this magnetic force was also checked with Equation (1.1.3.a). The magnetization of a small volume of the material in the AMR ring was estimated using the gadolinium magnetization curve in Figure 1.1.3c. The field gradient at the location of the material volume in question was estimated using the magnetic field profile around the AMR ring.

The gravitational force on the magnet assembly was calculated by estimating the mass of each component of the assembly. This was done by estimating the density of component's material and multiplying this by the estimated volume of the component.

5.2 Partial Tokamak Configuration Forces

5.2.1 Coil Forces

A sketch of the Lorentz forces acting on the coils of the partial tokamak in the x-y plane is shown in Figure 5.2.1a. Only the forces on half of the coils are shown because the forces are symmetrical about the y-z plane.

A list of the x and y components of these forces is shown in Table A.1.1a in Appendix - A. The net force calculated by the simulator in the x direction is zero because of the y-z plane symmetry. During operation, the system experiences a torque about the AMR ring axis due to the rotation of the AMR. This torque was estimated from the refrigeration power and rotational frequency of the ring by Equation (5.2.1a).

$$Torque = \frac{RefrigerationPower}{RotationalFrequency} = \frac{1000W}{5Hz \cdot 2\pi radians} = 31.8N \cdot m \quad (5.2.1a)$$

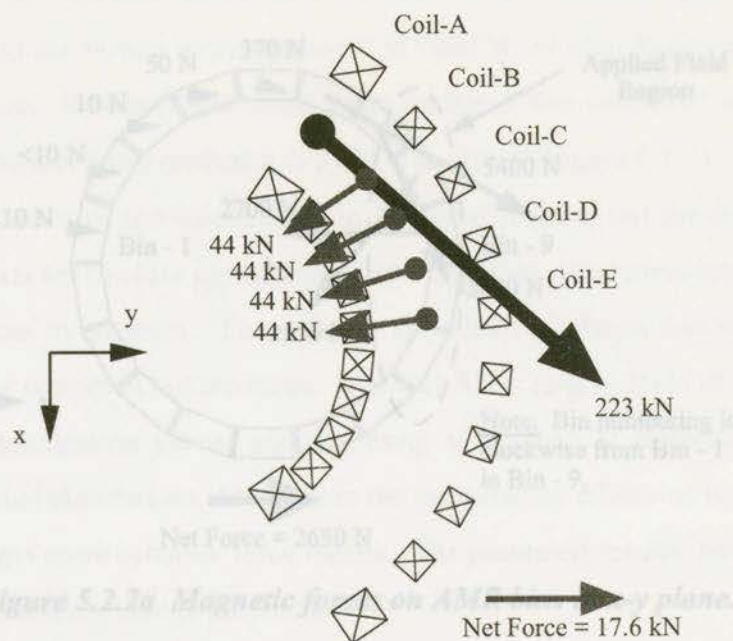


Figure 5.2.1a Lorentz forces in the x - y plane on individual coils of the partial tokamak assembly.

Although the torque is important, a 31.8 Nm torque does not cause a large force on the coil assembly compared to the other forces. The Lorentz forces that cause internal stress within the coil were not examined because the partial tokamak design was abandoned for the elliptical split pair configuration.

5.2.2 Forces on Magnetic Materials

The AMR ring is comprised of 18 bins of the magnetic refrigerant in the form of a packed particle beds. The beds are layered with five different magnetic refrigerants. As discussed in Section 4.2.2 the material properties of these refrigerants were assumed to be the same as the material properties of gadolinium. The calculated magnetic forces on the materials in the bins of the AMR ring are shown in Figure 5.2.2a. Each bin has an arc length of 19° and there is a 1° gap between the bins. The volume of each bin is 274 cm^3 but the porosity of the particle bed is 38% so each bin only contains 170 cm^3 of magnetic materials. The simulator assumes that the bins are 100% solid material so the virtual forces, calculated by the simulator, were reduced by 38% to account for the void volume. A list of the x and y components of these forces is shown in Table A.1.2a in Appendix - A.

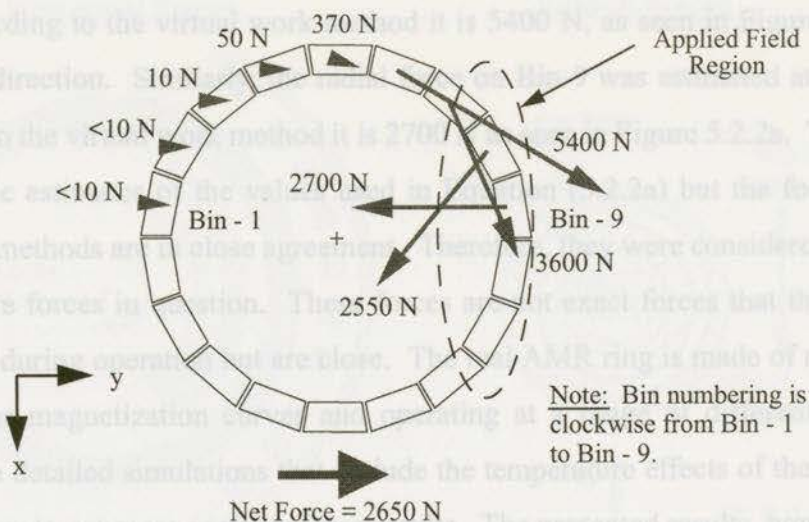


Figure 5.2.2a Magnetic forces on AMR bins in x - y plane.

There is also a small force on the AMR ring in the z direction because the ring is not centered in the x - y plane. It is centered 5 mm above the x - y plane and this causes a force in the z direction of approximately 500 N. It also acts in the opposite direction of the gravitational force so the net z direction force on the AMR ring is small compared to the other body forces but important for seating the AMR ring on the bearing.

These magnetic forces, calculated using the virtual work method, were confirmed by rough estimates using Equation (1.1.3.a). Bin-6, for example, is located in the portion of the field profile in Figure 4.3.2b with the highest azimuthal field gradient. Between 100° and 120° the field gradient is approximately 60 T/m in the azimuthal direction. The radial portion of the gradient is small so it was omitted for simplicity. The average field on Bin-6 is about 3 T so from the magnetization curve of gadolinium in Figure 1.1.3c the magnetization is about 7.0×10^5 A/m at 295 K. The force on this bin was then calculated by Equation (5.2.2a).

$$F = M \cdot \nabla B = \left(7.0 \times 10^5 \frac{\text{A}}{\text{m}} \right) \left(1.7 \times 10^{-4} \text{m}^3 \right) \left(60 \frac{\text{T}}{\text{m}} \right) = 7100 \text{N} \quad (5.2.2a)$$

A diagram of the net forces on the AMR and the partial tokamak magnet assembly is shown in Figure 5.2.4a. There are no externally applied horizontal forces so the sum of the net magnetic forces should equal zero. The results shown, however, indicate an imbal-

So, according to this calculation the force on Bin-6 in the azimuthal direction is 7100 N while according to the virtual work method it is 5400 N, as seen in Figure 5.2.2a, in the azimuthal direction. Similarly, the radial force on Bin-9 was estimated at 2800 N while according to the virtual work method it is 2700 N as seen in Figure 5.2.2a. There are some errors in the estimates of the values used in Equation (5.2.2a) but the forces calculated using both methods are in close agreement. Therefore, they were considered realistic estimates of the forces in question. These forces are not exact forces that the AMR would experience during operation but are close. The real AMR ring is made of many materials with similar magnetization curves and operating at a range of different temperatures. Much more detailed simulations that include the temperature effects of the magnetization are necessary to get more accurate force results. The presented results, however, are good estimates for engineering design purposes.

There are also magnetic forces on the steel yoke surrounding the coils. The net forces on this yoke are only in the y direction because the yoke is symmetrical about the x-y plane and the y-z plane. Calculating the forces using the virtual work method showed that the net force on the yoke is approximately -15 kN in the y direction.

5.2.3 Gravitational Body Forces

Table A.2.1a in Appendix-A gives a detailed description of the mass estimates of the components in the partial tokamak magnet assembly. The two distinct sub-assemblies of the total system are the coil assembly and the steel yoke. These two assemblies were considered separately because they operate at different temperatures and must, therefore, be physically and thermally isolated from each other. The coil assembly was estimated to weigh approximately 980 N (100 kg) and the steel yoke approximately 1180 N (120 kg). The weight of the AMR ring is approximately 250 N (25kg) but it is not supported by the magnet assembly structure.

5.2.4 Summary of Forces

A diagram of the net forces on the AMR and the partial tokamak magnet assembly is shown in Figure 5.2.4a. There are no externally applied horizontal forces so the sum of the net magnetic forces should equal zero. The results shown, however, indicate an imbal-

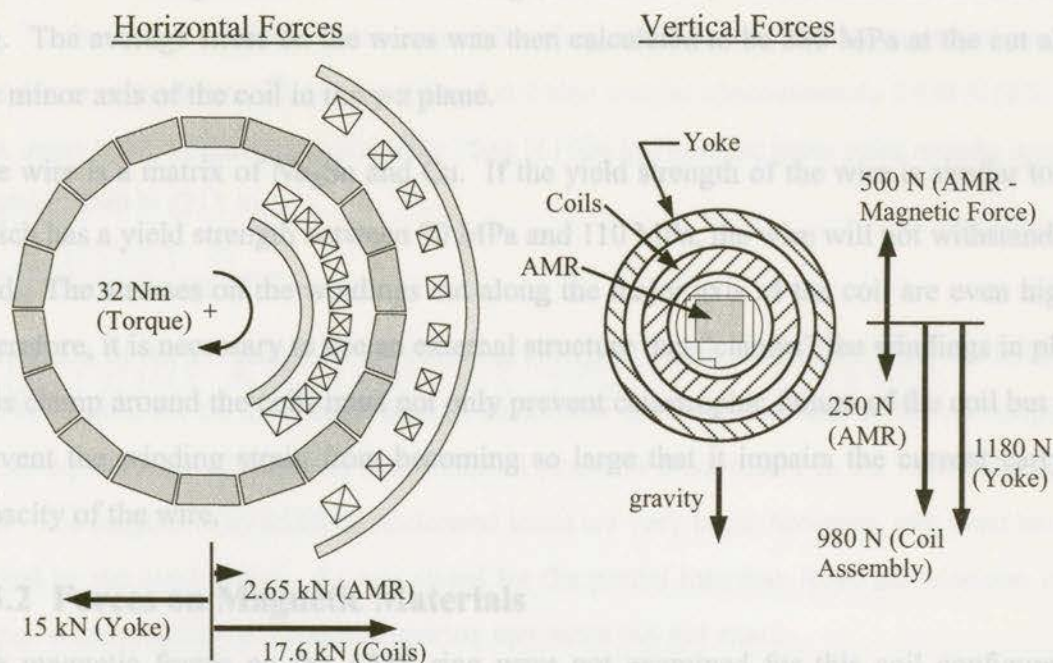


Figure 5.2.4a Schematic summary of forces on partial tokamak magnet assembly.

ance of the net forces. This indicates the limitation of the simulator's force calculation using finite element analysis. The sum of the net forces calculated by the magnetostatic simulator was converging to zero as the finite element mesh was discretized further. This increased discretization, however, did not affect the calculated results of the applied magnetic field profile and the energy error convergence criteria, discussed in Section 4.1, was less than the 2% requirement. Further discretization to improve the accuracy of the force calculations was not attempted because the problem was excessively large and beyond the capacity of the available computing facilities. Therefore, as stated before, these forces were considered good engineering estimates but not exact.

5.3 Elliptical Split Pair Configuration Forces

5.3.1 Coil Forces

The Lorentz force attracting the two elliptical coils together was estimated by the simulator to be approximately 290 kN. This is equivalent to 30 metric tonnes so the structure must be very strong to support this force. The net force on the winding in the x-direction, as shown in Figure 4.4.3e, is -1000 kN. This force was assumed to be distributed evenly

across the winding and 60% of the winding (i.e. the wires) was assumed to be load bearing. The average stress on the wires was then calculated to be 280 MPa at the cut along the minor axis of the coil in the y-z plane.

The wire is a matrix of Nb₃Sn and Cu. If the yield strength of the wire is similar to Cu, which has a yield strength between 70 MPa and 110 MPa, the wire will not withstand this load. The stresses on the windings cut along the major axis of the coil are even higher. Therefore, it is necessary to use an external structure that "clamps" the windings in place. This clamp around the coils must not only prevent catastrophic failure of the coil but also prevent the winding strain from becoming so large that it impairs the current carrying capacity of the wire.

5.3.2 Forces on Magnetic Materials

The magnetic forces on the AMR ring were not examined for this coil configuration because they were examined for the partial tokamak configuration. The forces on the AMR ring in the elliptical split pair configuration were assumed to be on the same order of magnitude or less than the ring forces in the partial tokamak configuration. This assumption was made because the field magnitudes and gradients on the rings of both winding configurations are similar but there less magnetic material is used in the smaller AMR of the split pair configuration.

The coils are wound on solid steel bobbins that are bolted to the yoke. The magnetic force on each bobbin was calculated to be 420 kN acting towards the opposite bobbin. This force is even greater than the attraction between the windings alone. As the windings are assembled on the bobbins, the total attractive force acting between the winding-bobbin assemblies is on the order of 710 kN or 72 metric tonnes which must be supported by the yoke.

5.3.3 Gravitational Body Forces

Table A.2.1a in Appendix-A gives a detailed description of the mass estimates of the components in the elliptical split pair magnet assembly. The three distinct sub-assemblies of the total system are the coil and bobbin assembly, the inner yoke, and the outer yoke. The coil-bobbin assembly and the inner yoke were considered as one assembly because they

are all maintained at liquid helium temperatures while the outer yoke is kept at around 50 K. To thermally separate these assemblies they must be physically separated so their weights are important. The two coils and bobbins weighs approximately 2470 N (252 kg). The inner yoke weighs approximately 1630 N (166 kg) and the inner yoke weighs approximately 2090 N (213 kg).

5.3.4 Summary of Forces

A diagram of the net forces on the elliptical split pair magnet assembly is shown in Figure 5.3.4a. There are no externally applied horizontal forces so the sum of the net magnetic forces equals zero. Therefore, little external structure is necessary in the horizontal direction. The magnetically induced horizontal loads are very large, however, and must be supported by the steel yokes. As was stated for the partial tokamak force calculations, these forces were considered good engineering estimates but not exact.

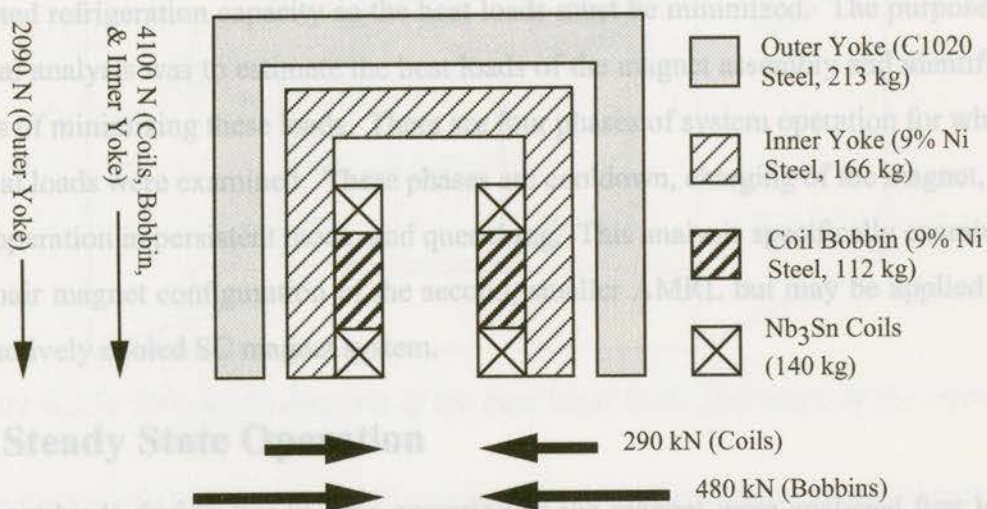


Figure 5.3.4a Schematic summary of forces on elliptical split magnet assembly.

6.2.1 First Stage Heat Loads

The first stage of the cryocooler is connected to the outer yoke of the magnet assembly and the copper current leads from the outside of the dewar. In addition to being a magnetic shield, the outer yoke acts also acts thermal radiation shield intercepting radiant heat from the inner walls of the vacuum vessel. The only mechanisms of heat transfer to the first

Chapter 6

Thermal Analysis of Magnet System

6.1 Thermal Analysis

The parasitic heat loads to the SC magnet assembly are conductively removed with a two stage Gifford-McMahon cryocooler. The first stage loads are removed at approximately 50 K and the second stage loads are removed at approximately 4.2 K. The cryocooler has a limited refrigeration capacity so the heat loads must be minimized. The purpose of the thermal analysis was to estimate the heat loads of the magnet assembly and identify techniques of minimizing these loads. There are four phases of system operation for which the thermal loads were examined. These phases are cooldown, charging of the magnet, steady state operation in persistent mode, and quenching. This analysis specifically examined the split pair magnet configuration of the second, smaller AMRL but may be applied to any conductively cooled SC magnet system.

Figure 6.2.1a Schematic diagram of the heat loads to the first stage of the cryocooler

6.2 Steady State Operation

The heat loads during steady state operation of the magnet were analyzed first because they are non-transient and the simplest to examine. This analysis identified the mechanisms of heat transfer and generation within the system and the elements of the design that affect these mechanisms. Once these mechanisms were quantified, design concepts were suggested that helped to minimize the heat loads.

where the emissivity factor, F_{12} , is defined as:

$$F_{12} = \left[\frac{1}{\epsilon_1} + \frac{\epsilon_2}{\epsilon_1} \left(\frac{1}{\epsilon_2} - 1 \right) \right]^{-1} \quad (6.2.1b)$$

6.2.1 First Stage Heat Loads

The first stage of the cryocooler is connected to the outer yoke of the magnet assembly and the copper current leads from the outside of the dewar. In addition to being a magnetic shield, the outer yoke acts also as thermal radiation shield intercepting radiant heat from the inner walls of the vacuum vessel. The only mechanisms of heat transfer to the first stage are conduction, \dot{Q}_{cond} , and radiation, \dot{Q}_{rad} . There are no sources of heat generation and convective heat transfer is negligible because the entire magnet assembly is kept in a vacuum of less than 10 mPa (7.5×10^{-5} torr) [58][59]. Figure 6.2.1a shows the heat loads to the first stage.

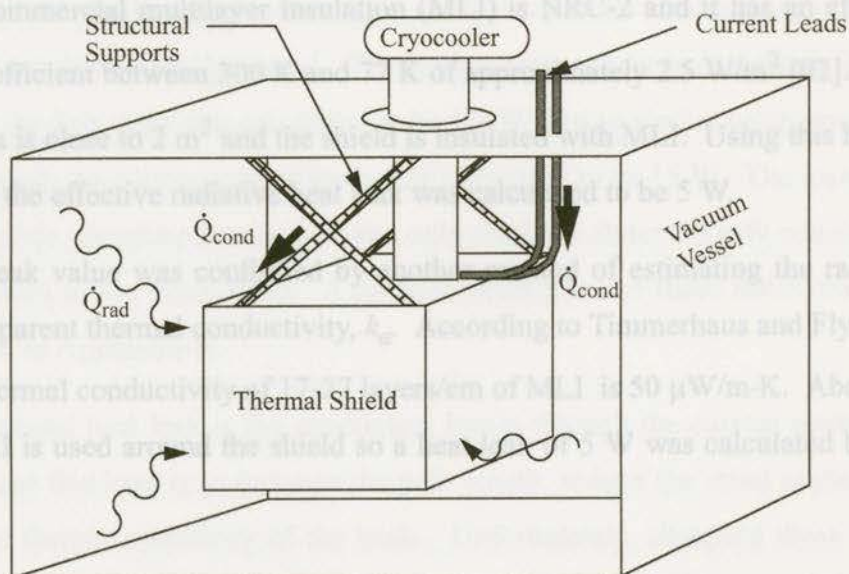


Figure 6.2.1a Schematic diagram of the heat loads to the first stage of the cryocooler.

The radiative heat load to a body fully enclosed by an outer vessel is found using Equation (6.2.1a).

$$\dot{Q}_{rad} = F_e \sigma A_1 (T_2^4 - T_1^4) \quad (6.2.1a)$$

Where the emissivity factor, F_e , is defined as:

$$F_e = \left[\frac{1}{e_1} + \frac{A_1}{A_2} \left(\frac{1}{e_2} - 1 \right) \right]^{-1} \quad (6.2.1b)$$

and e is the emissivity of surface and A is the area of the surface. The subscripts 1 and 2 denote the inner and outer vessels respectively. Low surface emissivities reduce the radiative heat transfer but Equation (6.2.1b) shows that the emissivity factor, F_e , is more heavily influenced by the emissivity of the outer vessel, e_2 , than by the emissivity of the inner vessel, e_1 . Therefore, if resources are limited it is better to put more effort into reducing the emissivity of the vacuum vessel than the shield. This may be done by polishing or electroplating.

The emissivity factor can also be reduced by adding floating shields with low emissivities. This typically done with reflective multilayer insulation. As stated in section 2.5, the most common commercial multilayer insulation (MLI) is NRC-2 and it has an effective heat transfer coefficient between 300 K and 77 K of approximately 2.5 W/m^2 [92]. The shield surface area is close to 2 m^2 and the shield is insulated with MLI. Using this heat transfer coefficient, the effective radiative heat leak was calculated to be 5 W.

This heat leak value was confirmed by another method of estimating the radiative leak using an apparent thermal conductivity, k_a . According to Timmerhaus and Flynn [59], the apparent thermal conductivity of 17-27 layers/cm of MLI is $50 \mu\text{W/m}\cdot\text{K}$. About 5 mm of packed MLI is used around the shield so a heat leak of 5 W was calculated by Equation (6.2.1c).

$$\dot{Q} = k_a A_1 \frac{dT}{dx} = \left(50 \times 10^{-6} \frac{\text{W}}{\text{m} \cdot \text{K}} \right) (2 \text{ m}^2) \left(\frac{300 \text{ K} - 50 \text{ K}}{0.005 \text{ m}} \right) = 5 \text{ W} \quad (6.2.1c)$$

The conductive heat losses through the structural supports and the current leads are also described by Equation (6.2.1c) using the apparent thermal conductivity of the material and the cross sectional area of the material. The apparent thermal conductivity is an estimate of the average thermal conductivity over the temperature range in question. A more accurate method of determining the heat transfer is to integrate the thermal conductivity over the temperature range in question. When the temperature dependence of the conductivity is taken into account, the one dimensional heat conduction through the supports of length L_s and cross sectional area A_s is calculated by Equation (6.2.1d) [59].

$$\dot{Q}_{cond} = \frac{A_s}{L_s} (\theta_2 - \theta_1) \quad (6.2.1d)$$

Where θ is the integral of the temperature dependent thermal conductivity, k , and is calculated by Equation (6.2.1e).

$$\theta_1 = \int_0^{T_1} k dT \quad (6.2.1e)$$

All of the structural supports in the magnet system are made of G-10 composite because it has a high strength to conductivity ratio. Although the yield strength of G-10 is only about half of the yield strength of stainless steel, the thermal conductivity is 1/10 to 1/20 of the conductivity of stainless steel. The net conductive heat leak through the all of the supports to the first stage was calculated to be 1.2 W. Using similar calculations, the conduction through the copper current leads was calculated to be 15 W. The instrumentation wire is 32 gauge phosphor bronze wire and only conducts about 0.3 mW which is insignificant compared to the other loads. A detailed description of these estimates is given in Table B.1.1a in Appendix-B.

The predominant heat leak is the conduction losses through the current leads. The only way to reduce this load is to increase the path length, reduce the cross sectional area, or increase the thermal resistivity of the leads. Unfortunately, changing these factors also increases the Joule heating of the leads during charging. Detailed design of the leads such that the combined conductive and Joule heating loads are minimized is an important consideration if the windings are to be permanently connected to the power supply. The AMRL magnet has been designed operate in a persistent current mode so the leads were not designed to have a minimized heat load while carrying current. Instead, they were designed so that their conductive heat leak did not exceed the refrigeration capacity of the cryocooler during steady state operation. A thermal sink was designed to absorb the Joule heating from the leads during charging.

6.2.2 Second Stage Heat Loads

The thermal loads on the second stage are caused by the same heat transfer mechanisms identified for the first stage. The radiative heating can be reduced by using MLI but a simpler and reportedly better method is to cover all surfaces with adhesive aluminized mylar tape [90][92]. Using this reflective tape provides an effective heat transfer rate of 12.5 mW/m^2 between 77 K and 4.2 K. This is a good way of reducing the radiative heat so the magnet was designed to have this tape applied to all of its radiating surfaces. The shield area is 2 m^2 so the radiative heat load was calculated to be 25 mW.

Like the first stage, the supports to the second stage are also made of G-10. The heat conducted through these supports was calculated to be 120 mW. The high temperature superconducting current leads are made of BSCCO ($\text{Bi}_2\text{Sr}_2\text{CaCu}_2\text{O}_8$) which has a thermal conductivity of $1 \text{ W/m}\cdot\text{K}$ at 77 K [116]. This value was conservatively assumed to remain constant below 77 K so the calculated conductive load was 35 mW for the high temperature superconducting current leads. The heat transferred through the instrumentation wires was calculated to be 0.2 mW which is insignificant.

The other source of heat at the second stage is the Joule heating due to the resistance of the soldered joints in the superconducting circuit. At 4 K the resistance of the soldered connections to the BSCCO leads is $10 \text{ n}\Omega$ [96]. This was assumed to be the resistance at the connections of the Nb_3Sn winding wires so the total calculated heat generated from all of the wire connections was 13 mW. A detailed description of all of the heat load estimates to the second stage is given in Table B.1.1a in Appendix-B.

6.3 Charging

The heat loads on the magnet assembly during the charging phase equal the steady state heat loads plus the extra loads caused by charging. The charging loads include the Joule heating of the copper current leads, the heat supplied to the PCS to maintain it in a normal state, the Joule heating of the PCS, and the Joule heating within the winding due to the and 20 K. The combination of the applied heat and the Joule heating of the switch, while it is in a normal state, is 60 mW [117]. This increases the total heat load to the second

eddy currents. The eddy current heating of the windings, however, has not been examined in this work. The magnet has a low charging rate so the eddy current heating was assumed to be very low.

The windings are designed to operate at 420 A. During the charging phase, which was set to be approximately 1 hour [117], the current through the leads increases monotonically. The Joule heating of the current leads is defined by equation Equation (6.3.0a).

$$\dot{Q}_{\Omega} = I^2 R = I^2 \left(\bar{\rho}_e \frac{\text{WireLength}}{\text{WireArea}} \right) \quad (6.3.0a)$$

6.4 Cooldown

The temperature averaged electrical resistivity of the copper leads is $10^{-8} \Omega \cdot \text{m}$ between room temperature and 50 K [85]. There are two 0.35 m long leads with a diameter of 6 mm so the total calculated Joule heating of the leads at 420 A was 44 W. During the charging phase, therefore, the heat load of the current leads increases from 15 W at zero current to 59 W, which is the combination of the conduction and Joule heating at 420 A. The steady state, first stage radiation heat loads and other conductive losses of 6.2 W must also be added to the charging loads of the current leads. Therefore, the heat load applied to the first stage of the cryocooler during charging increases from 21.2 W to 65.2 W.

The refrigeration power of the cryocooler is at least 30 W at the first stage [118]. The additional heat loads from the current leads during charging, therefore, exceed the capacity of the cryocooler and will increase the second stage temperature. To avoid this temperature increase, Dr. Hall designed a heat sink for the current leads [117]. The heat sink is made of stainless steel block that are connected to the first stage. The current leads are thermally connected to stainless steel blocks which absorb the heat from the leads. The heat sink has large enough thermal mass to absorb the excess heat produced during charging without increasing the second stage temperature of the cryocooler.

The persistent current switch was designed by Dr. Hall. It is made of NbTi superconducting switch wire and has a normal state resistance of 50 Ω when maintained between 15 K and 20 K. The combination of the applied heat and the Joule heating of the switch, while it is in a normal state, is 60 mW [117]. This increases the total heat load to the second

stage during charging to 260 mW. Because the switch is at 15 K to 20 K during charging but must operate near 4.5 K in persistent mode, the switch was designed to be thermally insulated from the second stage of the cryocooler by a connection made of G-10. The connection was designed so that there is a temperature differential between the switch and the cryocooler of about 15 K, as heat is conducted from the switch, due to the low thermal conductivity of the G-10. The switch is then maintained at 15 K to 20 K during charging but when charging is complete the heater is turned off and the switch cools to its superconducting state.

6.4 Cooldown

The outer yoke has a mass of 213 kg and must be cooled to 50 K. Inner yoke and coil assembly has a mass of 418 kg and must be cooled to 4.2 K. The cooling rate of these assemblies depends on their respective heat capacities and the cooling power of the refrigerator. The heat capacity of materials decreases at cryogenic temperatures so the cooling rate of the assemblies is non-linear. The total cooling time of the assemblies was estimated by calculating the total thermal energy removed during the cooldown and assuming an average refrigeration power of the cryocooler.

Because the heat capacity is temperature dependent, the cooldown time was estimated for three temperature ranges. It takes 62 hours to cool the magnet assembly from 300 K to 100 K. From 100 K to 50 K, it takes 32 hours to cool the entire assembly. From 50 K to 4 K, only the inner yoke and coil assembly must be cooled and take 60 hours to do so. The total cooldown time was calculated to be 154 hours. The complete calculations of the cooldown time are shown in Appendix-B.

The conduction cooled magnet by Hata et al. [78] had a reported total mass of 190 kg and took 56 hours to cool to operating temperature. The mass and cooldown time of Hata's system are both approximately one third of the corresponding values calculated for the AMRL magnet system. The calculated cooldown time of the AMRL magnet system is considered a good engineering estimate and acceptable for this work.

6.5 Quenching

During the quenching process the superconducting wire becomes normal and the stored magnetic energy of the system is dissipated as Joule heating within the windings. Ideally the energy is dissipated uniformly throughout the windings and causes uniform heating of the windings. Unfortunately, the localized zone where the quench begins remains normal for a longer period of time than the rest of the windings over the duration of the quench. This zone then rises in temperature more than the rest of the windings. Section 2.6.4 describe the quench process, the protection methods, and literature regarding the subject. A detailed quench analysis is an extensive problem and beyond the scope of this work.

During operation, the split pair magnet systems contains 640 kJ of stored magnetic energy as was calculated with the magnetic field model. This energy dissipates within the windings so the average temperature rise of the windings may be calculated in a similar fashion to the cooldown time calculations. The windings contain 125 kg of conductor and 50% of this is copper. The magnetic energy was conservatively assumed to be absorbed only by the copper in the windings. The heat absorbed by the copper was then calculated to be 10.24 J/g using Equation (6.5.0a).

$$Q = \frac{E}{m} = \frac{640 \text{ kJ}}{0.5 (125 \text{ kg})} = 10.24 \frac{\text{J}}{\text{g}} \quad (6.5.0a)$$

The heat absorption of copper as it heats from 4.2 K to a final equilibrium quench temperature, T_q , was calculated by integrating the heat capacity of copper as described by Equation (6.5.0b).

$$Q = \int_{4.2 \text{ K}}^{T_q} C(T) dT = 10.24 \frac{\text{J}}{\text{g}} \quad (6.5.0b)$$

A final equilibrium quench temperature of 98 K was calculated for a stored energy of 10.24 J/g in copper. This means that the final temperature of the windings after a quench will be 98 K at most if the quench is dissipated uniformly.

Although there is localized heating of the wires during the quench, this value shows that the winding temperature will not exceed 100 K after the system reaches thermal equilibrium. This temperature is a good lower limit design value to prevent large stresses induced by differential thermal expansion [17].

This work examined the mechanisms, prediction techniques, and protection methods of superconducting magnet quenching. Further work in this topic was done by Dr. Hall, who designed the quench protection circuitry. According to his estimates, the system will quench in less than 100 milliseconds and local overheating of the wire will not occur. This small quench time, however, means that there are induced voltages on the order of 3000 to 4000 volts within the winding so extra dielectric insulation has been added to the conductor.

6.6 Cryocooler and Conduction Pathways

The object of the conduction cooling system is to maintain the magnet assembly, and particularly the windings, at the lowest temperature possible. The heat loads on the magnet assembly must be conducted to the cryocooler through a conduction pathway. This pathway must be designed with the least thermal resistance possible. If the pathway resistance is low, the temperature differential between the cryocooler and the magnet assembly will be small for a given heat leak. Figure 6.6.0a shows a sketch of the second stage conduction pathway that was designed as part of this work for the split pair magnet system. This pathway was designed to have the smallest possible temperature difference between the cryocooler and the magnet given the design constraints of the system.

In Figure 6.6.0a, the numbered points identify important locations along the thermal path from the cryocooler to the windings. Point-2 is a copper flange that is soldered to the flexible copper braid at point-3 and bolted to the second stage of the cryocooler at point-1. Copper braid is used between point-3 and point-4 because the connection between the cryocooler and the windings must remain flexible to prevent stresses due to thermal contraction. Point-5 is also a copper flange that is soldered to the copper braid and this flange

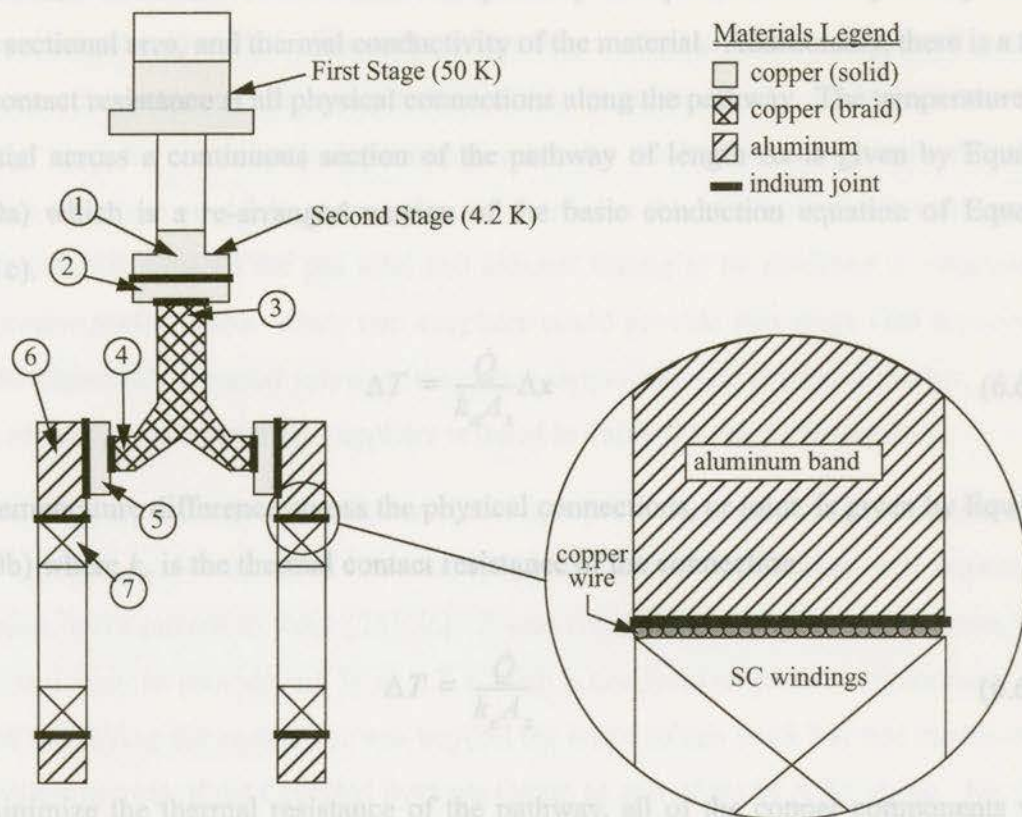


Figure 6.6.0a Sketch of thermal conduction path between superconducting windings and second stage of cryocooler.

is bolted to the aluminum band, point-6. This aluminum band is clamped around the outside of the windings to conduct heat from the windings and to share the magnetically induced stresses in the windings.

The connection between the aluminum clamp and the windings was designed using the connection technique described by Yazawa et al. [84] so the thermal resistance would be minimized. During the construction of the SC coil, the outer winding is wrapped with copper wire but this wire is not part of the electrical circuit. After the coil has been epoxy impregnated, the exterior of the winding is machined to expose the copper wire and indium sheet is inserted between the freshly machined copper surface and the aluminum bands that are clamped around the coils. A sketch of this connection is shown in Figure 6.6.0a.

The thermal resistance of the conduction pathway is dependent on the pathway length, cross sectional area, and thermal conductivity of the material. Additionally, there is a thermal contact resistance at all physical connections along the pathway. The temperature differential across a continuous section of the pathway of length Δx is given by Equation (6.6.0a) which is a re-arranged version of the basic conduction equation of Equation (6.2.1c).

$$\Delta T = \frac{\dot{Q}}{k_a A_x} \Delta x \quad (6.6.0a)$$

The temperature difference across the physical connections, or joint, is given by Equation (6.6.0b) where k_c is the thermal contact resistance of the connection.

$$\Delta T = \frac{\dot{Q}}{k_c A_x} \quad (6.6.0b)$$

To minimize the thermal resistance of the pathway, all of the copper components were specified to be made of oxygen free high conductivity (OFHC) copper. The soldered connections were specified to be made with indium solder and all of the bolted connections with indium gaskets.

Using Equation (6.6.0a) and Equation (6.2.1c) with the steady state heat loads calculated in Table B.1.1a, the temperature difference between the cryocooler and the windings was estimated to be approximately 0.6 K. A summary of the temperature differences through the conduction path is shown in Table B.3.0a in Appendix-B.

During this work a commercially available two stage Gifford-McMahon cryocooler was identified and purchased. Commercially available two stage Gifford-McMahon cryocoolers capable of operating at 4.2 K with passive rare earth regenerators were determined to be too expensive. It was decided, therefore, that a standard two stage GM cryocooler would be purchased and the second stage regenerator would be modified to use low temperature, high heat capacity, passive magnetic regenerator materials.

Several cryocooler suppliers were contacted and many different models of two stage GM cryocoolers were identified. The cryocoolers were evaluated based on their refrigeration capacity, compressor power, and potential ability to be modified. An important criteria was the need for a mechanically actuated valve for the helium refrigerant. All of the reported literature on 4.2 K cryocoolers indicated that this mechanical valve was necessary because it allowed the gas inlet and exhaust timing to be modified to improve the refrigerator performance. Only two suppliers could provide two stage GM cryocoolers with mechanically actuated valves so they were short-listed and evaluated further. A summary of the quotes from these suppliers is listed in Table C.1.0a of Appendix-C.

The selected cryocooler was a Balzers UCH 130 [76]. This was chosen because previously reported modifications to this model, operating at 4.2 K with rare earth regenerator materials, were proven to work [75][76]. It also could be modified by the supplier, at an additional cost, to provide 0.5 W at 4.2 K with a neodymium particle regenerator. The task of modifying the cryocooler was beyond the scope of this work but was continued by Mr. Walter Merida of the Cryofuel Systems Group as part of his M.A.Sc. thesis. Mr. Merida has conservatively estimated the cooling power of the modified cryocooler to be at least 30 W at 50 K and 0.5 W at 4.2 K [118].

The second stage cooling power of the cryocooler is greater than the calculated heat loads to the second stages so the temperature of the cryocooler during operation will remain at 4.2 K or slightly lower. Because the temperature differential between the cryocooler and the windings was calculated to be 0.6 K, the coldest part of the windings will be approximately 4.8 K or lower. This does not mean that the windings will be at a uniform temperature of 4.8 K. The temperature distribution throughout the windings is dependent upon the distribution of the heat load on the windings. The detailed analysis of the heat load and a temperature distribution throughout the windings is beyond the scope of this work. Experimental results of similar conduction cooled systems, however, indicate a temperature differential through the windings of 1 K. The conduction cooled SC magnet systems by Urata et al. [83], Furuyama et al. [64], and Herd et al. [80] had measured temperature differentials of 0.1 K, 1 K, and 1.4 K respectively across the SC windings.

6.7 Summary of Thermal Analysis

The calculated heat loads on the magnet and the operational temperatures of different locations within the system are summarized below in Table 6.7.0.a.

Table 6.7.0.a: Summary of estimated heat loads and temperatures of the elliptical split pair magnet assembly for the AMRL.

Location within Magnet Assembly	During Operation in Persistent Current Mode		During Charging	
	Heat Load	Temperature	Heat Load	Temperature
First Stage	21.2 W	50 K	21.2 → 65.2 W	50 K
Second Stage	200 mW	4.2 K	260 mW	4.2 K
SC Winding	---	4.8 ~ 5.8 K	---	---
Other Operational Information				
Estimated Cooldown Time				154 hours
Equilibrium Temperature of Windings after Quench				<100 K

Chapter 7

Conclusions and Future Work

7.1 Conclusions

The economic analysis of the LNG refuelling station showed that for systems with liquefaction efficiencies of at least 20%, capital cost is the greatest factor that affects the delivered LNG price. Liquefaction efficiencies greater than 20% provide only marginal economic benefits in the cost of the delivered fuel to the consumer. AMRL systems are very capital intensive so it is necessary to reduce their costs if they are to become commercially viable for LNG production.

This thesis presents a substantial part of the analysis and design of a conductively cooled superconducting magnet system for a rotary active magnetic regenerative liquefier. The individual topics examined in this work have been examined by other researchers but this work represents a unique synthesis of these topics. The winding configurations applicable to a rotary AMRL were evaluated and the partial tokamak and the elliptical split pair configurations were selected as suitable configurations. These configurations were then analyzed and designed. This is the first published work that has examined the details of applying the partial tokamak magnet configuration to a rotary AMRL.

The superconducting coils of these configurations were designed and optimized using computer modelling of the windings to calculate the resulting applied magnetic fields. The forces acting on the components of these two magnet systems were calculated. The estimates of these forces were used in the structural design. After a critical design review,

the analysis and design of the partial tokamak was then abandoned due to the high overall cost of the AMRL and the mechanical complexities of the associated componentry of the AMRL.

A partial tokamak coil configuration was designed to magnetize a region of 100° for a rotary AMR with a mean radius of 30 cm and a width of 5 cm. Based on literature, this is the first detailed analysis of a partial tokamak coil configuration for a rotary AMR. The configuration was designed to use ten superconducting solenoids made of NbTi filamentary wire. The end coils of the magnet assembly were designed with more ampere-turns than the central coils. These end coils produced a larger field than the central coils and decreased the azimuthal attenuation of the applied field so that the arc length of the region of uniform magnetization was maximized. The field attenuation between the coils of designs with less than ten coils was unacceptably large and caused a field "ripple" effect. The ten coil design had a gap field attenuation of less than 5% which met the field uniformity specifications. The applied field along the mean radius of the AMR ring was 6 T and the radial field attenuation across the width of the AMR was 1 T. The 6 T field was less than the specified field of 7 T but was the maximum attainable field given the performance limits of the NbTi conductor and the size of the AMR ring. This partial tokamak configuration could only provide a 7 T field if the AMR ring had mean radius of at least 60 cm and a width of 5 cm. An AMR of this size would also only have a radial field attenuation of approximately 0.5 T. The general conclusion of the partial tokamak configuration is that it is better suited to rotary AMRs with higher ratios of mean radius to width. The partial tokamak configuration also does allow for good utilization of the field by the AMR but requires a complex, coupled mechanical design of the entire AMRL.

An elliptical split pair coil configuration was designed to magnetize a region of 90° for a rotary AMR with a mean radius of 15 cm and a width of 5 cm. The windings were designed to use Nb₃Sn filamentary wire. This design provided a uniform field of greater than 7 T over the 90° magnetization region but had maximum local field within the windings of approximately 12.6 T. This high ratio of local field in the winding to mean applied field on the AMR is inherent to this configuration because of the large gap between the coils. Reducing the gap distance reduces this field ratio and, therefore, the amount of con-

ductor necessary for the windings. The large gap of this design was necessary for the large G-10 pressure housing of the AMR ring. If the G-10 housing was not hermetically sealed, as the pressure differential across the width of the AMR is only on the order of 30 kPa, then it could be smaller thus reducing the space between the coils. The dewar walls of the magnet system, which are made of stainless steel, could then be designed to withstand the pressure of the helium gas.

The elliptical split pair coil was designed to be conductively cooled by a two-stage, low temperature Gifford-McMahon cryocooler. The coils were designed to provide the 7 T field at an operating temperature of 5 K. The thermal loads on the elliptical split pair magnet configuration were calculated, the conduction cooling pathways were designed, and a suitable commercially available cryocooler was selected. According to the thermal analysis the windings will operate at less than 5.8 K but the temperature distribution within the windings is unknown. The performance of the magnet may, therefore, be reduced if the operating temperature in the high field section of the winding does attain the designed operating temperature. The successful operation of this magnet design depends on the assumption that the modified cryocooler will meet its cooling power performance estimates. If the modified cryocooler does not provide adequate cooling then the magnet system will not provide the specified magnetic field. The magnet will still work but to lesser capacity. If it is too warm it will not work at all. This, however, is unlikely to occur.

7.2 Suggestions for Future Work

The work completed in this thesis substantially examines the analysis and design of a superconducting magnet system for a rotary AMRL. Because of constraints on the scope and duration of this project there remain several topics that merit further research. Topics that should be researched further are described in the following list:

- The predicted system performance of the elliptical split pair magnet configuration designed in this work should be confirmed by experimental testing of the constructed system. These tests should examine the applied magnetic field profile with magnetic field probes, the estimated forces within the system by strain measurement, and measure the temperature distribution within the system during operation.

- An thermo-economic analysis of the effect of the conduction cooling system input power requirements on the overall liquefaction efficiency is needed. This should examine the scaling effects of the cooling system for the magnet on the AMRL and compare conventional liquid cryogen cooled systems to conduction cooled systems.
 - A more detailed quench analysis should be done. It should examine the effect of the inductive coupling between the windings on the quench propagation, the heat generation and dissipation in the windings, and the induced voltages between the windings. This analysis should be coupled with a detailed thermal and stress analysis of the windings.
 - An overall stress and strain analysis including thermal stresses and magnetic stresses during cooldown, operation, and quenching should be done. This should be used to identify high risk sections of the mechanical design and suggest design concepts to minimize these risks
 - A detail thermal simulation of the system is necessary to provide a better idea of the overall temperature distribution within the magnet assembly. A better estimation of the winding temperature would provide a better idea of the operating characteristics of the magnet. This could also be used to improve the conduction pathway design.
 - An experimental analysis of the contact resistance of realistic mechanical connections at 4.2 K should be done. This should examine bolted and soldered connections similar to the connections used in conductively cooled superconducting magnet systems. This should also examine the effect of using gaskets made of indium and other soft, conductive materials.
 - A thorough technical and economic feasibility study of the chainsaw AMRL configuration [42] is needed. The superconducting magnet system is the most expensive component of an AMRL system. Because the chainsaw design uses a simple solenoid magnet configuration it will be less expensive than an equivalent sized rotary AMRL.
- 9) Lee, T.H., Linden, H.R., Dreyfus, D.A., Vaska, T., *The Methane Age*, Kluwer Academic Publishers & NASA, 1988.
- 10) Barclay, J.A., Corless, A.J., "Cost Analysis of a Magnetic Liquefier in a Fleet-Size Cryofuel Refuelling System", *Solar Energy Technology, SED-Vol. 13*, pp. 43-50, ASME, 1992.

11. Barclay, J.A., "Cryofuels, Now and in the Future", Plenary Session, Cryogenic Engineering Conference, Columbus, OH, July 17-21, 1995.
12. Barclay, J.A., Goulet, D.W., Reid, C.H.J., "Comparison of Natural Gas Liquefiers for Fleet-size LNG/CNG Refuelling Systems", Windsor Workshop on Alternative Fuels, Toronto, ON, June 12-14, 1995.
13. Powers, C., Luscher, D., Meyer, C., Browning, L., A White Paper: Preliminary Assessment of LNG Vehicle Technology, Economics, and Safety Issues (Revision 1), GRI-91/0347, Gas Research Institute, 1991.

References

1. International Energy Agency, Energy Balances of OECD Countries 1992-1993, OECD/IEA, Paris, France, 1995.
2. Energy Information Administration, Alternatives to Traditional Transportation Fuels 1993, DOE/EIA-0585(93), U.S. Department of Energy, January, 1995.
3. "Clean Fuels Legislation Directory", The Clean Fuels Report, Vol. 6, No. 5, pp. 26-68, J.E. Sinor Consultants Inc., November, 1994.
4. Webb, R.F., Moyer, C.B., Jackson, M.D., "Distribution of Natural Gas and Methanol: Costs and Opportunities", Alternative Transportation Fuels, Quorum Books, Greenwood Press, Inc., 1989.
5. U.S. Department of Energy, Assesment of Costs and Benefits of Flexible and Alternative Fuel Use in the U.S. Transportation Sector, Technical Report Four: Vehicle and Fuel Distribution Requirements, DOE/PE-0095P, August, 1990.
6. Energy Information Administration, Alternatives to Traditional Transportation Fuels: An Overview, DOE/EIA-0585/O, U.S. Department of Energy, June, 1994.
7. International Energy Agency, Energy Statistics of OECD Countries 1992-1993, OECD/IEA, Paris, France, 1995.
8. Rogner, H-H., "Natural Gas as the Fuel for the Future", Annual Review of Energy, Vol. 14, pp. 47-73, 1989.
9. Lee, T.H., Linden, H.R., Dreyfus, D.A., Vasko, T., The Methane Age, Kluwer Academic Publishers & IIASA, 1988.
10. Barclay, J.A., Corless, A.J., "Cost Analysis of a Magnetic Liquefier in a Fleet-Size Cryofuel Refuelling System", Solar Energy Technology, SED-Vol. 13, pp. 43-50, ASME, 1992.

11. Barclay, J.A., "Cryofuels, Now and in the Future", Plenary Session, Cryogenic Engineering Conference, Columbus, OH, July 17-21, 1995.
12. Barclay, J.A., Goudie, D.W., Reid, C.E.J., "Comparison of Natural Gas Liquefiers for Fleet-size LNG/CNG Refuelling Systems", Windsor Workshop on Alternate Fuels, Toronto, ON, June 12-14, 1995.
13. Powars, C., Luscher, D., Moyer, C., Browning, L., A White Paper: Preliminary Assessment of LNG Vehicle Technology, Economics, and Safety Issues (Revision 1), GRI-91/0347, Gas Research Institute, 1991.
14. Richardson, F.W., Chiu, C., "Baseload LNG Plant Design", Proc. of the Energy Transportation, Transfer & Storage '94 Conference, 1994.
15. Spearing, I.G., A Numerical Model for a Rotary Active Magnetic Regenerative Refrigerator, M.A.Sc. Thesis, Department of Mechanical Engineering, University of Victoria, 1994.
16. Hall, J.L., Reid, C.E., Spearing, I.G., Barclay, J.A., "Thermodynamic Considerations for the Design of Active Magnetic Regenerative Refrigerators", Cryogenic Engineering Conference, Columbus, OH, July 17-21, 1995.
17. Wilson, M.N., Superconducting Magnets, Monographs on Cryogenics, Oxford University Press, New York, 1983.
18. Iwasa, Y., "Design and Operational Issues for 77 K Superconducting Magnets", IEEE Transactions on Magnetics, MAG-24, pp. 1211-1214, 1988.
19. Green, M.A., "High Tc Superconductor and Superconducting Magnets", ASME Winter Meeting, Chicago, IL, November 30 - December 5, 1988.
20. Ries, G. "Magnet Technology and Conductor Design with High Temperature Superconductors", Cryogenics, Vol. 33, No. 6, pp. 609-614, 1988
21. Tozai, N. "Liquid-Helium-Free Refrigeration for SC Magnets", Superconductor Industry, pp.41-42, Spring 1994.
22. Hall, J.L., Barclay, J.A., "A Prototype Active Magnetic Liquefier for Natural Gas, Part 1: Design and Construction", manuscript in preparation.
23. Lacaze, A.F., "Magnetic Refrigeration - An Overview", Proceedings of the International Institute of Refrigeration Conference, pp. 99-110, Prague, Czechoslovakia, 1986.

24. Barclay, J.A., "Magnetic Refrigeration: A Review of a Developing Technology", *Advances in Cryogenic Engineering*, Plenum Press, New York, Vol. 33, pp. 719-731, 1988.
25. Barclay, J.A., "A Review of Magnetic Heat Pump Technology", *International Cryogenic Engineering Conference*, Reno, NV, August 12-17, 1990
26. Zhang, L., Sherif, S.A., Veziroglu, T.N., Sheffield, J.W., "Performance Analysis of Reciprocating Magnetic Liquefiers", *International Journal of Hydrogen Energy*, Vol. 19, pp. 945-956, Elsevier Science Ltd., 1994.
27. Pratt, W.P. Jr, Rosenblum, S.S., Steyert, W.A., Barclay, J.A., "A Continuous Demagnetization Refrigerator Operating Near 2 K and a Study of Magnetic Refrigerants", *Cryogenics*, Vol. 17, pp. 689-693, 1977.
28. Barclay, J.A., "A 4 K to 20 K Rotational-Cooling Magnetic Refrigerator Capable of 1-mW to 1-W Operation", *Cryogenics*, Vol. 20, pp. 468-471, 1980.
29. Hakuraku, Y., Ogata, H., "Conceptual Design of a New Magnetic Refrigerator Operating between 4 K and 20 K", *Japanese Journal of Applied Physics*, Vol. 24, No. 11, pp. 1548-1551, November, 1985.
30. Hakuraku, Y., Ogata, H., "A Magnetic Refrigerator for Superfluid Helium Equipped with a Rotating Superconducting Magnetic System", *Japanese Journal of Applied Physics*, Vol. 25, No. 1, pp. 140-146, January, 1986.
31. Hakuraku, Y., Ogata, H., "A Rotary Magnetic Refrigerator for Superfluid Helium Production", *Journal of Applied Physics*, Vol. 60, No. 9, pp. 3266-3268, November, 1986.
32. Nakagome, H., Kuriyama, T., Ogiwara, H., Yazawa, T., Hashimoto, T., "A Rotating Magnetic Refrigerator for Helium Liquefaction", *Proceedings of the International Cryogenic Engineering Conference 11*, Berlin, 1986.
33. Nakagome, H., Takahashi, M., Ogiwara, H., "A Parasitic Magnetic Refrigerator for Cooling Superconducting Magnet", *IEEE Transactions on Magnetics*, Vol. 24, No. 2, pp. 1113-1116, March, 1988.
34. Barclay, J.A., Stewart, W.F., "The Effect of Parasitic Refrigeration on the Efficiency of Magnetic Liquefiers", *Proceedings of the 17th Intersociety Energy Conversion Engineering Conference (IECEC '82)*, August, 1982.
35. DeGregoria, A.J., Zimm, C., Janda, D.J., Lubasz, R.A., Jastrab, A.G., Johnson, J.W., Ludeman, E.M., "Active Magnetic Regenerator Method and Apparatus", *United States Patent*, No. 5,249,424, October 5, 1993.

36. Hakuraku, Y., Ogata, H., Daikoku, T., Suzuki, N., "Magnetic Refrigerator", United States Patent, No. 4,532,770, August 6, 1985.
37. Kirol, L.D., Dacus, M.W., "Rotary Recuperative Magnetic Heat Pump", *Advances in Cryogenic Engineering*, Plenum Press, New York, Vol. 33, pp. 757-766, 1988.
38. Rowe, J.R., Hertel, J.A., Barclay, J.A., Cross, C.R., Trueblood, J.R., Hill, D.D., "Conductively Cooled Nb₃Sn Magnet System for a Magnetic Refrigerator", *IEEE Transactions on Magnetics*, Vol. 27, No. 2, pp. 2377-2380, March, 1991
39. Rosenblum, S.S., Steyert, W.A., Pratt, W.P., A Continuous Magnetic Refrigerator Operating Near Room Temperature, Los Alamos National Laboratory, Report No. LA-6581, May, 1977.
40. Barclay, J.A., Steyert, W.A., "Magnetic Refrigeration for Space Applications", *Proceedings of the 8th International Cryogenic Engineering Conference*, Genoa, Switzerland, February, 1980.
41. Waynert, J.A., Barclay, J.A., Foster, R.W., "A Portable Magnetic Refrigerator for X-30 Slush Hydrogen Maintenance", *5th National Aero-Space Plane Technology Symposium*, Paper No. 76, October 17-21, 1988.
42. Barclay, J.A., Stewart, W.F., Henke, M.D., Kalash, K.E., "Magnetic Refrigeration Apparatus with Belt of Ferro or Paramagnetic Material", United States Patent, No. 4,704,871, November 10, 1987.
43. Kral, S.F., Barclay, J.A., "Magnetic Refrigeration: A Large Cooling Power Cryogenic Refrigeration Technology", *Applications of Cryogenic Technology*, Plenum Press, New York, Vol. 10, pp. 27-41, 1991.
44. Barclay, J.A., Steyert, W.A., Magnetic Refrigerator Development, Electric Power Research Institute, EPRI-EL 1757, 1987.
45. Barclay, J.A., Stewart, W.F., Overton, W.C., Chandler, R.J., Harkleroad, O.D., "Experimental Results on a Low-Temperature Magnetic Refrigerator", *Advances in Cryogenic Engineering*, Plenum Press, New York, Vol. 31, pp. 743-752, 1986.
46. Prenger, F.C., Hill, D.D., Trueblood, J., Servais, T., Laatsch, J., Barclay, J.A., "Performance Tests of a Conductive Magnetic Refrigerator using a 4.5 K Heat Sink", *Advances in Cryogenic Engineering*, Plenum Press, New York, Vol. 35, pp.1105-1113, 1990.
47. Iwasa, Y., Case Studies in Superconducting Magnets, Selected Topics in Superconductivity, Plenum Press, New York, 1994.

48. Wood, M., "Some Aspects of the Design of Superconducting Solenoids", *Cryogenics*, Vol. 2, pp. 297-300, September, 1962.
49. Thomas, E.J., Bright, C.D., "Optimizing the Design of Superconducting Solenoids", *Cryogenics*, Vol. 6, No. 1, pp. 10-13, February, 1966.
50. Ishiyama, A., Shimizu, K., "An Optimal Design Method for Multi-Section Superconducting Magnets", *IEEE Transactions on Magnetics*, Vol. 28, No. 1, pp 919-922, January, 1992.
51. Lubell, M.S., "Empirical Scaling Formulas for Critical Current and Critical Field for Commercial NbTi", *IEEE Transactions on Magnetics*, MAG-19, pp. 754, 1983.
52. Barclay, J.A., Shnaider, M., Cross, C.R., Prenger, F.C., Stewart, W.F., Zimm, C.B., "Design Limitations on Magnetic Refrigerators Imposed by Magnetic Forces", *Proceedings of the 4th International Cryocooler Conference*, Easton, MD, September, 1986.
53. Mitchell, N., Mszanowski, U., "Stress Analysis of Structurally Graded Long Solenoid Coils", *IEEE Transactions on Magnetics*, Vol. 28, No. 1, pp. 226-229, 1992.
54. Ekin, J.W., "Stress/Strain Effects on Critical Current", *Cryogenics*, Vol. 35, VAMAS Supplement, pp. S25-S28, 1995.
55. Minas, C., Laskaris, E.T., "Structural Design and Analysis of a Cryogen-Free Open Superconducting Magnet for Interventional MRI Applications", *IEEE Transactions on Applied Superconductivity*, Vol. 5, No. 2, June, 1995.
56. Jüngst, K.P., Ries, G., Förster, S., Graf, F., Obermaier, G., Lehmann, W., "Magnet System for a Superconducting Magnetic Separator", *Cryogenics*, Vol. 24, pp. 648-652, November, 1984.
57. Vermilyea, M.A., Novel Cryogen-Free Actively Shielded Superconducting Magnets for Maglev Vehicles, General Electric Company, U.S. Dept. of Transportation Report, NTIS # PB93-154771, June, 1992.
58. Barron, R.F., Cryogenic Systems, Monographs on Cryogenics, Oxford University Press, New York, 1985.
59. Timmerhaus, K.D., Flynn, T.M., Cryogenic Process Engineering, The International Cryogenics Monograph Series, Plenum Press, New York, 1989.
60. van der Laan, M.T.G., Tax, R.B., ten Kate, H.H.J., van de Klundert, L.J.M., "A 1 T, 0.33 m Bore Superconducting Magnet Operating with Cryocoolers at 12 K", *IEEE Transactions on Magnetics*, Vol. 28, No. 1, pp. 633-636, January, 1992.

61. Kasen, M.B., "Mechanical and Thermal Properties of Filamentary-Reinforced Structural Composites at Cryogenic Temperatures 1: Glass Reinforced Plastics", *Cryogenics*, Vol.15, pp. 327-349, June, 1975.
62. Duband, L., Hui, L., Lange, A., "Thermal Isolation of Large Loads at Low Temperature using Kevlar Rope", *Cryogenics*, Vol. 33, No. 6, pp 643-647, 1993.
63. Hoenig, M.O., "Design Concepts for a Mechanically Refrigerated 13 K Superconducting Magnet System", *IEEE Transactions on Magnetics*, Vol. MAG-19, No. 3, pp. 880-883, May, 1983.
64. Furuyama, M., Yamamoto, H., Tanaka, M., Kaneko, M., Matsubara, Y., Ogasawara, T., "Performance of a Nb₃Sn Tape Magnet Cooled by Indirect Conduction Method", *Advances in Cryogenic Engineering*, Vol. 35a, pp. 625-631, Plenum Press, New York, 1990.
65. van der Laan, M.T.G., Tax, R.B., ten Kate, H.H.J., van de Klundert, L.J.M., "The Cryogenic System of a Conduction Cooled 12 K Superconducting Magnet", *Cryogenics*, Vol. 30c, pp. 163-167, 1990.
66. Hashimoto, T., Li, R., Matsumoto, K., Sahashi, M., Yayama, H., Tomokiyo, A., "Recent Progress in the Magnetic Materials for Regenerator in the Range from 4.2 K to 20 K", *Proceedings of the International Cryogenic Materials Conference, China, 1988*.
67. Kuriyama, T., Hakamada, R., Nakagome, H., Tokai, Y., Sahashi, M., Li, R., Yoshida, O., Matsumoto, K., Hashimoto, T., "High Efficient Two-Stage GM Refrigerator with Magnetic Material in the Liquid Helium Temperature Range", *Advances in Cryogenic Engineering*, Vol. 35, pp. 1261-1269, Plenum Press, New York, 1990.
68. Masuyama, S., Yamamoto, Matsubara, Y., "A NbTi Split Magnet Directly Cooled by a Cryocooler", *IEEE Transactions on Applied Superconductivity*, Vol. 3, No. 1, pp. 262-265, March, 1993.
69. Onishi, A., Li, R., Satoh, T., Kanazawa, H., Aikawa, S., Hashimoto, T., "A 4 K GM Cryocooler with Hybrid Regenerator of Magnetic Materials", *Proceedings of the 7th International Cryocooler Conference, Santa Fe, NM, November 17-19, 1992*.
70. Yabuki, M., Nitta, H., Hashimoto, T., Kuriyama, T., Takahashi, M., Nakagome, H., "Magnetic Regenerator Material in the Liquid Helium Temperature Range - Recent Advances and its Possibility", *Proceedings of the 4th Joint Sino-Japanese Seminar on Cryocoolers and Concerned Topics, Beijing, P.R. China, October 19-23, 1993*.

71. Kuriyama, T., Takahashi, M., Nakagome, H., Hashimoto, T., Nitta, H., Yabuki, M., "Development of 1 Watt Class 4 K GM Refrigerator with Magnetic Materials", *Advances in Cryogenic Engineering*, Vol. 39b, pp. 1335-1342, Plenum Press, New York, 1994.
72. Tsukagoshi, T., Nitta, H., Yoshida, A., Matsumoto, K., Hashimoto, T., Kuriyama, T., Takahashi, M., Ohtani, Y., Nakagome, H., "Refrigeration Capacity of a GM Refrigerator with Magnetic Regenerator Materials", *Cryogenic Engineering Conference*, Columbus, OH, July 17-21, 1995.
73. Satoh, T., Onishi, A., Li, R., Asami, H., Kanazawa, Y., "Development of 1.5W 4K GM Cryocooler with Magnetic Regenerator Material", *Cryogenic Engineering Conference*, Columbus, OH, July 17-21, 1995.
74. Chafe, J., Green, G., Reidy, R.C., "Neodymium Regenerator Test Results in a Standard Gifford-McMahon Refrigerator", *Proceedings of the 7th International Cryocooler Conference*, Santa Fe, NM, November 17-19, 1992.
75. Reidy, R.C., "Low Temperature, High Performance G-M Refrigerator", *Cryogenics*, Vol. 33, No. 6, pp. 653-658, 1993.
76. Balzers, 8 Sagamore Park Road, Hudson, NH 03051, USA.
77. Takahashi, M., Hakamada, R., Yamamoto, K., Kuriyama, T., Nakagome, H., Masuyama, S., Yamamoto, H., Tanaka, S., Matsubara, Y., "A 7.7 NbTi Superconducting Magnet System Cooled by a 4 K GM Refrigerator", *Advances in Cryogenic Engineering*, Vol. 39a, pp. 343-350, Plenum Press, New York, 1994.
78. Hata, F., Sakubara, J., Chong, C.K., Yamada, Y., Hasebe, T., Ishihara, M., Watanabe, K., "A Conduction Cooled Superconducting Magnet Using High-Tc Oxide Current Leads", *IEEE Transactions on Magnetics*, Vol. MT-13, *Proceedings of the 13th International Magnet Technology Conference*, Victoria, Canada, September 20-24, 1993.
79. Herd, K.G., Laskaris, E.T., Thompson, P.S., "A Cryogen-Free Superconducting Magnet for Maglev Applications: Design and Test Results", *IEEE Transactions on Applied Superconductivity*, Vol. 5, No. 2, June, 1995.
80. Herd, K.G., Laskaris, E.T., Thompson, P.S., "A Dual Refrigerator Assembly for Cryogen Free Superconducting Magnet Applications", *IEEE Transactions on Applied Superconductivity*, Vol. 5, No. 2, June, 1995.
81. Laskaris, E.T., Ackermann, R., Dorri, B., Gross, D., Herd, K., Minas, C., "A Cryogen Free Open Superconducting Magnet for Interventional MRI Applications", *IEEE Transactions on Applied Superconductivity*, Vol. 5, No. 2, June, 1995.

82. Cowey, L., Cetnik, P., Timms, K., Daniels, P., Mellors, J., McDougall, I., "Cryogen Free Nb₃Sn Magnet, Operated at 9.5K with High Tc BiSrCaCuO (2122) Current Leads", IEEE Transactions on Applied Superconductivity, Vol. 5, No. 2, June, 1995.
83. Urata, M., Kuriyama, T., Yazawa, T., Koyanagi, K., Yamamoto, K., Nomura, S., Yamada, Y., Nakagome, H., Murase, S., Maeda, H., Horigami, O., "A 6 T Refrigerator Cooled NbTi Superconducting Magnet with 180 mm Room Temperature Bore", IEEE Transactions on Applied Superconductivity, Vol. 5, No. 2, June, 1995.
84. Yazawa, T., Koyanagi, K., Urata, M., Kuriyama, T., Ohtani, Y., Nomura, S., Maeda, H., "Cooling Structure for a 6 T NbTi Superconducting Magnet Directly Cooled by Cryocooler", IEEE Transactions on Applied Superconductivity, Vol. 5, No. 2, June, 1995.
85. Reed, R.P., Clark, A.F., Materials at Low Temperatures, American Society for Metals, Metals Park, OH 44073, USA, 1983.
86. Radebaugh, R., "Thermal Conductance of Indium Solder Joints at Low Temperature", Review of Scientific Instruments, Vol. 48, No. 1, 1977.
87. Deutsch, M., "Thermal Conductance in Screw-Fastened Joints at Helium Temperatures", Cryogenics, Vol. 19, pp. 273-274, May, 1979.
88. Salerno, L.J., Kittel, P., Spivak, A.L., "Thermal Conductance of Pressed Metallic Contacts Augmented with Indium Foil or Apiezon Grease at Liquid Helium Temperatures", Cryogenics, Vol. 34, No. 8, pp. 649-654, 1994.
89. GEC Alsthom Ltd., P.O. Box 136, Manchester M60 1AN, England.
90. Leung, E.M.W., Fast, R.W., Hart, H.L., Heim, J.R., "Techniques for Reducing Radiation Heat Transfer Between 77 and 4.2 K", Advances in Cryogenic Engineering, Vol. 25, pp. 489-494, Plenum Press, New York, 1980.
91. King Seely Company, Winchester, Massachusetts, USA.
92. Gathright, T.R., Reeve, P.A., "Effect of Multilayer Insulation on Radiation Heat Transfer at Cryogenic Temperatures", IEEE Transactions on Magnetics, Vol. 24, No. 2, pp. 1105-1108, 1988.
93. 3M, St. Paul, MN 55144, USA.
94. Communication with Cryomagnetics, Inc., Oak Ridge, TN, 37830, USA, September, 1995.
106. Personal communication with Dr. Michael Coffey, Cryomagnetics, Inc., 1006 Alvin Weinberg Dr., Oak Ridge, TN 37830, USA.

95. Chafe, J.N., Green, G., "An Analytic Investigation of Conduction Cooled Cryogenic Current Leads", Proceedings of the 4th Interagency Meeting on Cryocoolers, Plymouth, USA, January, 1991.
96. Bock, J., Elschner, S., Herrmann, P.F., "MCP-BSCCO 2212 Tubes for Power Applications up to 10 kA", IEEE Transactions on Applied Superconductivity, Vol. 5, June, 1995.
97. Ponnusamy, D., Li, Z., Ravi-Chandar, K., "Large Current High Tc Superconducting Rods for Current Lead Applications", IEEE Transactions on Applied Superconductivity, Vol. 5, June, 1995.
98. Ballarino, A., Ijspeert, A., "Design and Test of the Prototype High Tc Current Leads for the Large Hadron Collider Orbit Correctors", IEEE Transactions on Applied Superconductivity, Vol. 5, June, 1995.
99. Dorri, B., Laskaris, E.T., "Persistent Current Switch for Cryogen-Free MR Magnets", IEEE Transactions on Applied Superconductivity, Vol. 5, June, 1995.
100. Noto, K., Kono, Y., Matsukawa, M., Itagaki, M., Ishida, T., Chiba, K., Tatsuki, T., Homma, H., Sadakata, N., Saito, T., Kohno, O., "Development of a 50 A Fast Response, Magnetically Controlled Persistent Current Switch", IEEE Transactions on Applied Superconductivity, Vol. 5, June, 1995.
101. Sadakata, N., Uchiyama, K., Goto, K., Saito, T., Kohno, O., Kouno, Y., Matsukawa, M., Noto, K., Homma, H., Tatsuki, T., "Fast Switching Characteristics of Magnetic Persistent Current Switch for SMES", IEEE Transactions on Applied Superconductivity, Vol. 5, June, 1995.
102. Green, M.A., "The Role of Quench Back in Quench Protection of a Superconducting Solenoid", Cryogenics, Vol. 24, pp. 659-668, December, 1984.
103. Yunus, M.I., Iwasa, Y., Williams, J.E.C., "A.C. Loss Induced Quenching in Multicoil Adiabatic Superconducting Magnets", Cryogenics, Vol. 35, No. 2, pp. 93-100, 1995.
104. Schwall, R.E., "Protection System for Inductively Coupled Magnets", IEEE Transactions on Magnetics, Vol. 27, No. 2, pp. 1700-1703, March, 1991.
105. Ansoft Corporation, Four Station Square, Suite 660, Pittsburgh, PA 15219, USA.
106. Sun Microsystems, Inc., 2550 Garcia Avenue, Mountain View, CA 94943-1100, USA
107. Supercon, Inc., 830 Boston Turnpike Road, Shrewsbury, MA 01545, USA.
108. Personal communication with Dr. Michael Coffey, Cryomagnetics, Inc., 1006 Alvin Weinberg Dr., Oak Ridge, TN 37830, USA.

109. Teledyne Wah Chang, 7400 Highway 20 West, Huntsville, AB 35806, USA.
110. Reid, C.E.J., Development of Magnetic Refrigerants for Active Magnetic Regenerative Refrigerators, M.A.Sc. Thesis, Department of Mechanical Engineering, University of Victoria, 1995.
111. Personal communication with Mr. Paul Reeve, Department of Physics, University of Victoria.
112. Cryomagnetics, Inc., 1006 Alvin Weinberg Dr., Oak Ridge, TN 37830, USA.
113. Oxford Instruments, Inc., 130a Baker Avenue Extension, Concord, MA 01742, USA.
114. American Magnetics, Inc., PO Box 2509, 112 Flint Road, Oak Ridge, TN 37831-2509, USA.
115. Ansoft Corporation, Maxwell 3D Field Simulator - Reference Manual, pp. A-14, Four Station Square, Suite 660, Pittsburgh, PA 15219, USA, December, 1993.
116. High Temperature Superconducting Bulk Material for Superconducting Leads, Hoechst Celanese Corporation, Advanced Technology Group, 86 Morris Avenue, Summit, NJ 07901, USA.
117. Personal communication with Dr. Jeffery Hall, Cryofuel Systems Group, University of Victoria.

118. Personal communication with Mr. Walter Merida, Cryofuel Systems Group, University of Victoria.

119. CVI Inc., P.O. Box 2138, Columbus, OH 43216, USA.

Coil Name (as shown in)	Lorentz Force	Lorentz Force
Coil - A	-148.4 kN	166.2 kN
Coil - C	-20.2 kN	-37.0 kN
Coil - D	-13.4 kN	-41.4 kN
Coil - E	-5.7 kN	-43.2 kN
Total (all 10 coils)	0 N	17.6 kN

A.1.2 Magnetic Material Forces

The x-y components of the magnetic forces on the AMR material bins shown in Figure 5.2.2a, as calculated by the magnetic field simulator, are listed in Table A.1.2a. Values are rounded to the nearest 10 N.

Appendix - A

Body Forces on Magnet Assembly

A.1 Large AMRL - Partial Tokamak Configuration

A.1.1 Coil Forces

The x-y components of the coil forces shown in Figure 5.2.1a, as calculated by the magnetic field simulator, are listed in Table A.1.1a.

Table A.1.1a: Lorentz forces on partial tokamak coils of large AMRL in x-y directions.

Coil Name (as shown in Figure 5.2.1a)	Lorentz Force in x-Direction	Lorentz Force in y-Direction
Coil - A	-148.4 kN	166.2 kN
Coil - B	-23.4 kN	-35.8 kN
Coil - C	-20.2 kN	-37.0 kN
Coil - D	-13.4 kN	-41.4 kN
Coil - E	-5.7 kN	-43.2 kN
Total (all 10 coils)	0 N	17.6 kN

A.1.2 Magnetic Material Forces

The x-y components of the magnetic forces on the AMR material bins shown in Figure 5.2.2a, as calculated by the magnetic field simulator, are listed in Table A.1.2a. Values are rounded to the nearest 10 N.

Table A.1.2a: Magnetic forces on AMR bins of large AMRL in x-y directions.

Bin Name (as shown in Figure 5.2.2a)	Magnetic Force in x-Direction	Magnetic Force in y-Direction
Bin - 1	<10 N	<10 N
Bin - 2	<10 N	<10 N
Bin - 3	<10 N	<10 N
Bin - 4	20 N	40 N
Bin - 5	110 N	350 N
Bin - 6	2980 N	4530 N
Bin - 7	3460 N	1120 N
Bin - 8	1430 N	-2090 N
Bin - 9	330 N	-2670 N
Total (all 18 bins)	0	2650

A.1.3 Gravitational Forces

A list of the components in the magnet assembly, their volumes, and estimated masses are shown in Table A.2.1a.

Table A.1.3a: Estimates of weight of partial tokamak magnet assembly.

Component Name	Estimated Volume	Material Density	Estimated Mass	Quantity	Total Weight
Main Coils	494 cm ³	6.5 g/cm ³ (65% Cu, 45% FRP)	3.2 kg	8	250 N
Compensating Coils	943 cm ³	6.5 g/cm ³ (65% Cu, 45% FRP)	6.1 kg	2	120 N
Coil Bobbins	355 cm ³	8.96 g/cm ³ (100% Cu)	3.2	10	310 N
Yoke	15,000 cm ³	7.9 g/cm ³ (100% Steel)	120 kg	1	1180 N
Coil Separation Structure	---	Cu, FRP, & Steel	30 kg	---	300 N
Total	---	---	220 kg	---	2160 N

A.2 Small AMRL - Elliptical Split Pair Configuration

A.2.1 Gravitational Forces

A list of the components in the elliptical split pair magnet assembly, their volumes, and estimated masses are shown in Table A.2.1a.

Table A.2.1a: Estimates of weight of elliptical split pair magnet assembly.

Component Name	Estimated Volume	Material Density	Estimated Mass	Quantity	Total Weight
Main Coils	10,750 cm ³	6.5 g/cm ³ (65% Cu, 45% FRP)	70 kg	2	1370 N
Coil Bobbins	7,100 cm ³	7.9 g/cm ³ (100% Steel)	56	2	1100 N
Inner Yoke	21,000 cm ³	7.9 g/cm ³ (100% Steel)	166 kg	1	1630 N
Outer Yoke	27,000 cm ³	7.9 g/cm ³ (100% Steel)	213 kg	1	2090 N
Total	---	---	631 kg	---	6190 N

* $\theta_1 = 45,000 \text{ W/m at } T = 300 \text{ K for Cu wire;}$

* $\theta_2 = 9,000 \text{ W/m at } T = 50 \text{ K for Cu wire; and}$

* $k_0 = 20 \text{ W/m-K for phosphor-bronze wire from 300 K to 50 K.}$

A summary of all of the heat loads to the first stage is shown in Table B.1.1a.

Table B.1.1a: Heat loads to first stage.

Description	Length (m)	Cross Sectional Area (m ²)	Material	Quantity	Heat Load (W)
from Dewar to Cryo Stage	0.025 m thick	Surface Area 2 m ²	MLI in vacuum	—	5
Main Supports	0.45	1.5×10^{-5}	G-10	1	0.21
Alignment Pins	0.025	7.85×10^{-5}	G-10	2	0.95
Cu Circuit	0.35	7.13×10^{-5}	Cu	2	15

Appendix - B

Heat Loads on Magnet Assembly

B.1 Heat Loads During Steady State Operation

B.1.1 First Stage Loads

Based on an effective conduction coefficient of $50 \mu\text{W/m}\cdot\text{K}$ for MLI, the radiative heat loads are estimated to be on the order of 5 W. The conductive heat loads to the first stage are calculated using Equation (6.2.1d) and Equation (6.2.1c) where:

- $\theta_1 = 160 \text{ W/m}$ at $T = 300 \text{ K}$ for G-10;
- $\theta_2 = 13 \text{ W/m}$ at $T = 50 \text{ K}$ for G-10;
- $\theta_1 = 45,000 \text{ W/m}$ at $T = 300 \text{ K}$ for Cu wire;
- $\theta_2 = 9,000 \text{ W/m}$ at $T = 50 \text{ K}$ for Cu wire; and
- $k_a \approx 20 \text{ W/m}\cdot\text{K}$ for phosphor-bronze wire from 300 K to 50 K.

A summary of all of the heat loads to the first stage is shown in Table B.1.1a.

Table B.1.1a: Heat loads to first stage.

Description	Length (m)	Cross Sectional Area (m ²)	Material	Quantity	Heat Load (W)
Radiative Heat from Dewar to Outer Yoke	0.005 m thick	Surface Area 2 m ²	MLI in vacuum	---	5
Main Supports	0.45	1.59x10 ⁻⁴	G-10	4	0.21
Alignment Pins	0.025	7.85x10 ⁻⁵	G-10	2	0.95
Cu Current Leads	0.35	7.13x10 ⁻⁵	Cu	2	15
Instrumentation Wire	0.5	3x10 ⁻⁸	phosphor-bronze	20	0.0003
Total	---	---	---	---	21.2

Table B.1.2a: Heat loads to second stage.

Description	Length (m)	Cross Sectional Area (m ²)	Material	Quantity	Heat Load (mW)
Radiative Heat from Outer Yoke to Inner Yoke	---	Surface Area 2 m ²	Reflective Mylar Tape 12.5 mW/m ²	---	25
Main Supports	0.13	1.59x10 ⁻⁴	G-10	8	120
BSCCO Current Leads	0.13	3.03x10 ⁻⁸	BSCCO	2	35
Instrumentation Wire	0.2	3x10 ⁻⁸	phosphor-bronze	20	0.2
Joint Heating	---	---	---	---	13
Total	---	---	---	---	193

B.1.2 Second Stage Loads

The conductive heat loads to the first stage are calculated using Equation (6.2.1d) and Equation (6.2.1c) where:

- $\theta_1 = 13 \text{ W/m at } T = 50 \text{ K for G-10};$
- $\theta_2 = 0.8 \text{ W/m at } T = 4.2 \text{ K for G-10};$
- $k_a \approx 1 \text{ W/m}\cdot\text{K for superconducting current leads from 50 K to 4.2 K.}$
- $k_a \approx 20 \text{ W/m}\cdot\text{K for phosphor-bronze wire from 50 K to 4.2 K.}$

The Joule heating of the electrical connections is calculated by:

$$\dot{Q}_\Omega = I^2 R \quad (\text{B.1.2a})$$

Where the resistance of the electrical connections at 4 K is 10 n Ω and the operating current is 400 A. For 8 connections the total Joule heating is calculated to be 13 mW. A summary of all of the heat loads to the second stage is shown in Table B.1.1a.

Table B.1.2a: Heat loads to second stage.

Description	Length (m)	Cross Sectional Area (m ²)	Material	Quantity	Heat Load (mW)
Radiative Heat from Outer Yoke to Inner Yoke	---	Surface Area 2 m ²	Reflective Mylar Tape 12.5 mW/m ²	---	25
Main Supports	0.13	1.59x10 ⁻⁴	G-10	8	120
BSCCO Current Leads	0.13	5.03x10 ⁻⁵	BSCCO	2	35
Instrumentation Wire	0.2	3x10 ⁻⁸	phosphor-bronze	20	0.2
Joule Heating	---	---	---	---	13
Total	---	---	---	---	193

B.2 Estimation of Cooldown Time

The cooldown time of the magnet assembly was estimated for three temperature ranges because the heat capacity of the magnet assembly is temperature dependent. The magnet assembly is constructed mostly of steel and copper. The heat capacity of these metals is similar in this temperature range but copper has a slightly higher heat capacity. The heat capacity of the magnet assembly was assumed to be equal to that of copper so the cooldown time estimates are conservative.

B.2.1 Cooldown from 300 K to 100 K

The cryocooler has a cooling power of approximately 115 W at 77 K [76] so the average cooling power between 300 K and 100 K was assumed to be 200 W. The average heat capacity of copper in this temperature range is 0.35 kJ/kg·K. The mass of the assembly is 631 kg so the stored thermal energy was found by Equation (B.2.1a).

$$E = mC(T_2 - T_1) = (631 \text{ kg}) \left(0.35 \frac{\text{kJ}}{\text{kgK}} \right) (300 \text{ K} - 100 \text{ K}) = 44170 \text{ kJ} \quad (\text{B.2.1a})$$

The cooldown time of 62 hours was then estimated by dividing the total thermal energy stored in the system by the cooling power of the cryocooler as in Equation (B.2.1b).

$$\text{Time} = \frac{E}{\text{CoolingPower}} = \frac{44170 \text{ kJ}}{200 \text{ W}} = 62 \text{ hours} \quad (\text{B.2.1b})$$

B.2.2 Cooldown from 100 K to 50 K

The cryocooler has a minimum cooling power of 30 W at 50 K so the average cooling power between 100 K and 50 K was estimated to be 50 W. The heat capacity of copper decreases in this temperature range so the total thermal energy absorbed was calculated by integrating the heat capacity over this temperature range [59]. The thermal energy was calculated to be 9.17 kJ/kg so the total thermal energy of the assembly was estimated to be 5790 kJ. Using Equation (B.2.1b) the cooldown time was calculated to be 32 hours.

B.2.3 Cooldown from 50 K to 4.2 K

The cryocooler has an assumed cooling power of 1 W at 4.2 K so the average cooling power between 50 K and 4.2 K was assumed to be 3 W. The absorbed thermal energy was estimated, using the same method as in Section B.2.2, to be 1.56 kJ/kg. Only the inner yoke and winding assembly, which has a mass of 418 kg, must be cooled to 4.2 K. The total stored energy was then calculated to be 652 kJ resulting in a cooldown time of 60 hours.

B.3 Thermal Conduction Pathway

The temperature differentials through the second stage conduction pathway shown in Figure 6.6.0a were found using Equation (6.6.0a) and Equation (6.5.0b). A summary of the calculations is shown in Table B.3.0a. The values of the contact resistance were obtained from Salerno [88] and Radebaugh [86].

Table B.3.0a: Temperatures within second stage conduction pathway during steady state operation.

Span Between Points Shown in Figure 6.6.0a	Heat Load (mW)	Apparent Thermal Conductivity (mW/cm·K)	Thermal Contact Resistance (mW/cm ² ·K)	Area (cm ²)	Temperature Differential (K)
1 to 2	193	---	95	26	0.08
2 to 3	158	---	30,000	4.75	0.002
3 to 4 ($\Delta x=25\text{cm}$)	79	2000	---	2.38	0.45
4 to 5	79	---	30,000	2.38	0.002
5 to 6	79	---	95	17.5	0.05
6 to 7	79	---	43	200	0.01
Total ΔT	---	---	---	---	0.6

Table C.1.0a: Summary of cryocooler specifications.

	Balzers	CVI
Electrical Requirements	200-230 V 3 phase, 60 Hz	208 V 3 phase, 60 Hz
Rated Input Power	6.5 kW	5.5 kW
Electrical Standards	Not CSA Approved -must be inspected	CSA Approved
Maintenance Interval	9,000 hours	N.A.
Helium Gas Lines	2 x 32 ft lines	2 x 10 ft lines
		10 ft

Appendix - C

Cryocooler Evaluations

C.1 Description of Suitable Cryocoolers

The quotations and specifications of the two stage GM cryocoolers from Balzers [76] and CVI [119].

Table C.1.0a: Summary of cryocooler specifications.

	Balzers	CVI
Model	UCH 130	CGR 511
Price (\$ Can)	\$ 30,022	\$ 31,602
Delivery Time	4 weeks	8 weeks
Warranty	12 months	18 months
Refrigeration Capacity at Operation Frequency of 60 Hz	115 W @ 77 K 15 W @ 20 K simultaneous	60 W @ 77 K 12 W @ 20 K not simultaneous
Lowest No-Load Temperature	6.5 K	10 K
No Load Temperature Stability	± 0.2 K	± 0.5 K
Variable Speed DC Motor Controller	No	Yes
Weight	14 kg	17.2 kg
Maintenance Interval	9,000 hours	15,000 hours
Compressor Type	Scroll	Scroll
Static Charge Pressure	250 psig	210 psig
Water Coolant Requirements	3.0 gpm	1.0 gpm

Table C.1.0a: Summary of cryocooler specifications.

	Balzers	CVI
Electrical Requirements	200-230 V 3 phase, 60 Hz	208 V 3 phase, 60 Hz
Nominal Input Power	6.5 kW	5.5 kW
Electrical Standards	Not CSA Approved -must be inspected	CSA Approved
Oil Adsorber Life	26,000 hours	N.A.
Helium Gas Lines	2 x 32 ft lines	2 x 10 ft lines
Cold Head Controller Cable	50 ft	10 ft

Degrees Awarded:

B.A.Sc. Queen's University 1990

Honours and Awards:

Canadian Mineral Industry Education Foundation Scholarship 1988

Canadian Mineral Industry Education Foundation Scholarship 1989

Publications:

Banley, J.A., Goudie, D.W., Reid, C.B.J., "Comparison of Natural Gas Liquefiers for Fleet-size LNG/CNG Refuelling Systems", 1995 Windsor Workshop on Alternate Fuels, Toronto ON, June 12-14, 1995.

Oosthuizen, P.H., Tong, P.C.C., Goudie, D., "An Experimental Study of the Flow About Tandem Cylinders Near a Flat Endwall", Proceedings of the 1991 Canadian Congress of Applied Mechanics, Vol. 2, pp. 434-435, 1991.

Partial Copyright License
Vita

Surname: Goudie

Given Names: Dale William

Place of Birth: Murrayville, British Columbia, Canada

Educational Institutions Attended:

University of Victoria	1993 to 1996
Queen's University	1985 to 1986
Queen's University	1986 to 1990

Degrees Awarded:

B.A.Sc. Queen's University 1990

Honours and Awards:

Canadian Mineral Industry Education Foundation Scholarship	1988
Canadian Mineral Industry Education Foundation Scholarship	1989

Publications:

Barclay, J.A., Goudie, D.W., Reid, C.E.J., "Comparison of Natural Gas Liquefiers for Fleet-size LNG/CNG Refuelling Systems", 1995 Windsor Workshop on Alternate Fuels, Toronto ON, June 12-14, 1995.

Oosthuizen, P.H., Tong, P.C.C., Goudie, D., "An Experimental Study of the Flow About Tandem Cylinders Near a Flat Endwall", Proceedings of the 1991 Canadian Congress of Applied Mechanics, Vol. 2, pp. 434-435, 1991.

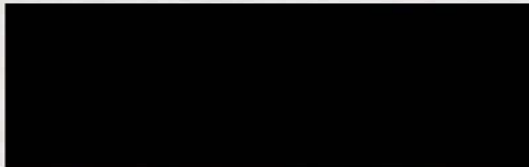
Partial Copyright License

I hereby grant the right to lend my thesis to users of the University of Victoria Library, and to make single copies only for such users or in response to a request from the Library of any other university, or similar institution, on its behalf or for one of its users. I further agree that permission for extensive copying of this thesis for scholarly purposes may be granted by me or a member of the University designated by me. It is understood that copying or publication of this thesis for financial gain shall not be allowed without my written permission.

Title of Thesis:

Analysis and Design of a Conductively Cooled Superconducting Magnet System for a Rotary Active Magnetic Regenerative Liquefier

Author:



Dale William Goudie

April 30, 1996

25% COTTON FIBER U.S.A.
Southworth Bond